Eur. Phys. J. C 27, 331–374 (2003)
Digital Object Identifier (DOI) 10.1140/epjc/s2002-01127-9

THE EUROPEAN PHYSICAL JOURNAL C

Search for neutrino oscillations on a long base-line at the CHOOZ nuclear power station

M. Apollonio[3], A. Baldini[2], C. Bemporad[2], E. Caffau[3], F. Cei[2], Y. Déclais[5,a], H. de Kerret[6], B. Dieterle[8], A. Etenko[4], L. Foresti[2], J. George[8], G. Giannini[3], M. Grassi[2], Y. Kozlov[4], W. Kropp[7], D. Kryn[6], M. Laiman[5], C. E. Lane[1], B. Lefièvre[6], I. Machulin[4], A. Martemyanov[4], V. Martemyanov[4], L. Mikaelyan[4], D. Nicolò[2], M. Obolensky[6], R. Pazzi[2], G. Pieri[2], L. Price[7], S. Riley[7], R. Reeder[8], A. Sabelnikov[4], G. Santin[3], M. Skorokhvatov[4], H. Sobel[7], J. Steele[1], R. Steinberg[1], S. Sukhotin[4], S. Tomshaw[1], D. Veron[7], V. Vyrodov[7]

[1] Drexel University, Philadelphia, PA 19104, USA
[2] INFN, Sezione di Pisa and University of Pisa, 56010 S. Piero a Grado Pisa, Italy
[3] INFN, Sezione di Trieste and University of Trieste, 34021 Trieste, Italy
[4] Russian Research Center, Kurchatov Institute, Moscow 123183, Russia
[5] LAPP-IN2P3-CNRS Annecy, 74941 Annecy-le-Vieux, France
[6] PCC-IN2P3-CNRS Collège de France, 75231 Paris, France
[7] University of California, Irvine, CA 92717, USA
[8] University of New Mexico, Albuquerque, NM 87131, USA

Received: 20 September 2002 / Revised version: 18 November 2002
Published online: 3 March 2003 –

Abstract. This final article about the CHOOZ experiment presents a complete description of the $\overline{\nu}_{\rm e}$ source and detector, the calibration methods and stability checks, the event reconstruction procedures and the Monte Carlo simulation. The data analysis, systematic effects and the methods used to reach our conclusions are fully discussed. Some new remarks are presented on the deduction of the confidence limits and on the correct treatment of systematic errors.

1 Introduction

Neutrino oscillation experiments are sensitive probes of the possible existence of a finite neutrino mass and provide a way to study physics beyond the Standard Model of electroweak interactions [1]. In fact, lepton flavour violation and the existence of nonzero neutrino masses can give rise to neutrino oscillations, as first pointed out by Pontecorvo [2,3] and Maki et al.[4]. Several experiments, studying solar [5–8] or atmospheric neutrinos [9–14], have measured fluxes consistently lower than expectations. This can be interpreted as due to various forms of neutrino oscillations. In particular the so-called "atmospheric neutrino anomaly" is the observation of a $\nu_\mu/\nu_{\rm e}$ ratio which is roughly one half of what expected and its possible explanation might be due to either oscillation of $\nu_\mu \leftrightarrow \nu_\tau$ or to $\nu_\mu \leftrightarrow \nu_{\rm e}$. In a model with two neutrino eigenstates of mass m_1 and m_2 which mix to form two flavour states, a pure beam of electron–flavoured neutrinos has a survival probability which oscillates due to the m_1-m_2 mass difference. For a single neutrino energy E_ν(MeV) and a distance from the source L (meters), the survival probability can be written in terms of the mixing parameter $\sin^2 2\theta$ and the difference of the squared masses $\delta m^2 = \left|m_2^2 - m_1^2\right|$ as follows:

$$P(\overline{\nu}_{\rm e} \to \overline{\nu}_{\rm e}) = 1 - \sin^2 2\theta \, \sin^2 \left(\frac{1.27\, \delta m^2 (\mathrm{eV}^2)\, L(\mathrm{m})}{E_\nu (\mathrm{MeV})} \right). \quad (1)$$

Atmospheric neutrino results give a δm^2 from 10^{-2} to $10^{-3}\,\mathrm{eV}^2$. Long base-line (L-B) reactor neutrino experiments [15] have been one of the most powerful ways to investigate $\overline{\nu}_{\rm e} \to \overline{\nu}_\mu$ neutrino oscillations (or, more generally, $\overline{\nu}_{\rm e} \to \overline{\nu}_{\rm x}$ oscillations). The CHOOZ [16,17] and PALO VERDE [18] experiments utilized the high intensity and purity of the reactor core flux to achieve high sensitivity.

The CHOOZ experiment had an average value of $L/E \sim 300$ ($L \sim 1\,\mathrm{km}$, $E \sim 3\,\mathrm{MeV}$), an intense and nearly pure neutrino flavour composition ($\sim 100\%\,\overline{\nu}_{\rm e}$) and an intensity known to better than 2%. It could therefore make a definitive contribution to solving the problem of the atmospheric neutrino anomaly. CHOOZ removed the possibility of explaining the atmospheric neutrino anomaly by $\nu_{\rm e} \leftrightarrow \nu_\mu$ oscillations and Super–Kamiokande showed that $\nu_\mu \leftrightarrow \nu_\tau$ caused the effect [19].

The experiment was designed to detect reactor $\overline{\nu}_{\rm e}$'s via the inverse β-decay reaction

$$\overline{\nu}_{\rm e} + \mathrm{p} \to \mathrm{e}^+ + \mathrm{n} \quad (2)$$

[a] *Present address:* IPNL-IN2P3-CNRS Lyon

The signature is a delayed coincidence between the prompt e^+ signal (boosted by the two 511 keV annihilation γ rays) and the signal from the neutron capture. The target material is a Hydrogen-rich (free protons) paraffin–based liquid scintillator loaded with Gadolinium, which was chosen due to its large neutron capture cross section and to the high γ-ray energy released after n-capture (~ 8 MeV, well above the natural radioactivity).

In this final paper we present a complete description of the experiment, calibration methods and stability checks, event reconstruction procedures and the Monte Carlo simulation.

Three different analyses, which have already been published [17], are more extensively discussed in this paper. The main one is based on all the available information: the measured number of positron events as a function of energy, separately obtained from each reactor. It uses the two spectral shapes, as well as the absolute normalizations. The second result is based only on the comparison of the positron spectra from the two, different-distance reactors. This analysis is largely unaffected by the absolute value of the $\overline{\nu}_e$ flux, the cross section, the number of target protons and the detector efficiencies, and is therefore dominated by statistical errors. The sensitivity in this case is limited to $\delta m^2 \gtrsim 2 \cdot 10^{-3}\,\mathrm{eV}^2$ due to the small distance, $\Delta L = 116.7$ m, between the reactors. The explored $(\delta m^2, \sin^2 2\theta)$ parameter space still matches well the region of the atmospheric neutrino anomaly. The third analysis is similar to the first, but does not include the knowledge of the absolute normalizations.

Finally, some new remarks are presented, concerning the deduction of the confidence limits and the correct treatment of the systematic errors.

2 The $\overline{\nu}_e$ source and the expected interaction rate

Nuclear reactors were the first sources used to search for neutrino oscillations and, in general, for systematic studies of neutrino properties. In past experiments (i.e. up to the 1980s), the knowledge of the reactor neutrino flux and spectrum ($\approx 10\%$ accurate at that time) limited the sensitivity to oscillations. Oscillation tests were performed by comparing the neutrino event rate at different distances (up to ~ 100 m) from the reactor. This approach eliminated the systematic uncertainty associated with the absolute neutrino flux, often much greater than the experiment statistical error. Since then, our knowledge base of fission reactors, in particular of pressurized water reactors (PWR), has much improved, thanks to the previous reactor experiments and to direct studies of fission reactions on several elements. Present uncertainty on the neutrino flux and spectrum induces systematic errors on the event rate which are lower than 3%. It is therefore possible to perform experiments, at one fixed distance from a reactor only, relying on the adequate knowledge of the neutrino source. The reactor $\overline{\nu}_e$ flux is perfectly isotropic and essentially with no contamination from other neutrino types, since the ν_e emission rate is lower than the one of $\overline{\nu}_e$ by a factor $> 10^5$ and may therefore be discarded [20].

Table 1. Summary of the CHOOZ data acquisition cycle between April 1997 and July 1998

	Time (h)	$\int W\,\mathrm{d}t$ (GWh)
Run	8761.7	
Live time	8209.3	
Dead time	552.4	
Reactor 1 only ON	2058.0	8295
Reactor 2 only ON	1187.8	4136
Reactors 1 & 2 ON	1543.1	8841
Reactors 1 & 2 OFF	3420.4	

2.1 Description

The CHOOZ nuclear power plant is located in the village of the same name, standing on the banks of the River Meuse in the north of France close to the border with Belgium.

The power plant consists of two twin pressurized-water (PWR) reactors belonging to a recently developed generation (N4) in France. The main innovation consists in an improved power yield (4.25 GWth, 1.45 GWe at full operating conditions), larger than any other PWR reactor. The first reactor reached full power in May 1997, the second in August 1997. Table 1 summarizes data acquisition (from April 7, 1997 to July 20, 1998). The schedule was quite suitable for separating the individual reactor contributions and for determining the reactor-OFF background.

The core of both reactors consists of an assembly of 205 fuel elements bound to the socket plate of the reactor vessel. The vessel is filled with pressurized water ($p = 155$ bars) at a temperature ranging from 280 °C at the entrance to about 320 °C at the exit. The water, which acts as a neutron moderator and cooling element, circulates through four independent systems. Each of these involves a primary pump and a steam generator comprising 5416 tubes immersed in the water of a secondary loop at a much lower pressure (56 bars) than primary loop pressure. As soon as the primary water passes through these tubes, the secondary water is vaporized and the steam produced travels to the turbine-alternator unit connected to the electric system [21].

The water in the primary loop is slightly doped by Boron, a strong absorber of thermal neutrons. Boron activity yields information on the trend of the chain reaction in the core.

2.2 Reactor power monitor

Two methods were developed by the E.D.F. technical staff to monitor the total thermal power produced by each reactor. The first one is based on the heat balance of the steam generators. Measurements are made of parameters

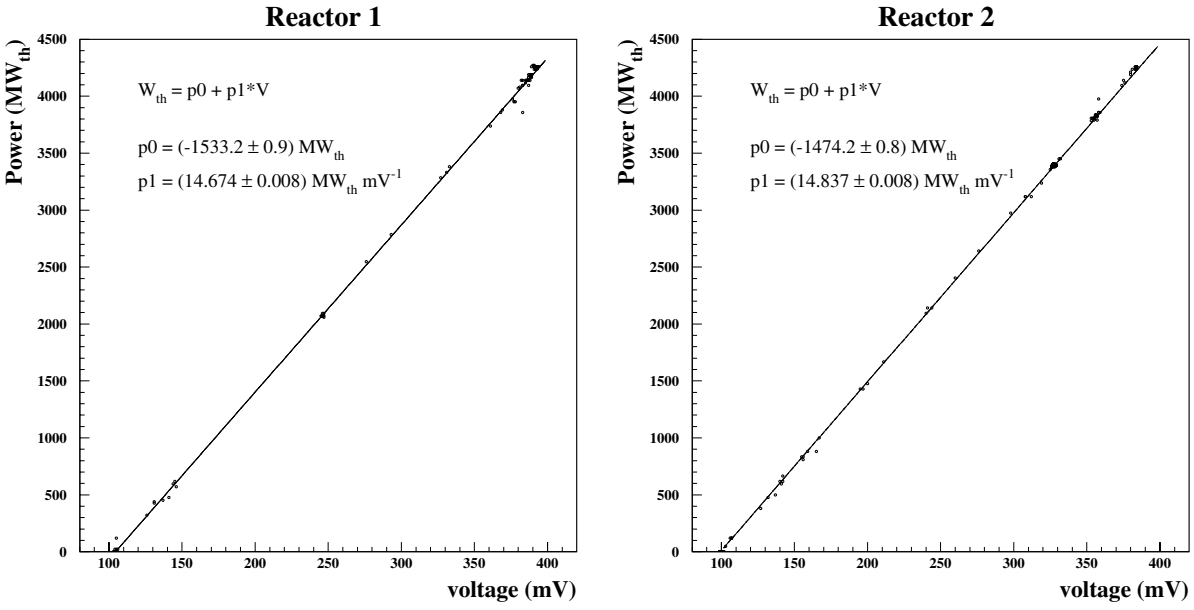

Fig. 1. Voltmeter calibration for reactor 1 (*left*) and 2 (*right*)

(water flow rate, vapour pressure and temperature in the secondary loop) needed to determine the amount of heat supplied to the steam generators. The resulting values are periodically available on a special computer network which records the data on an Excel file. The overall precision on the calculated thermal power is claimed to be 0.6%.

The second set of thermal power data is provided by the external neutron flux measurement. This flux is expected to be directly proportional to the fission rate inside the core and, as a consequence, to the released thermal power. For each reactor, four different neutron detectors (one proportional counters plus three ionization chambers) are located at the opposite sides of the reactor vessel. This method is less precise than the other one because of the spread in the energy release per fission of the different fissile isotopes. Accuracy is estimated to be about 1.5%. However, this method has the advantage of operating continuously and is used simultaneously as a power monitor and sensor for the reactor safety system. Neutron detector outputs are fed to the computer network and written twice a day (or more frequently if the power ramps up or down) to another Excel file. The computer is also programmed to drive a direct current generator whose amplitude is proportional to the neutron detection rate. Such a signal was measured in the CHOOZ experiment by a CAMAC voltmeter across a 5Ω resistor (connected in series to each loop). This provided a direct, instantaneous information about the thermal power for both reactors. The voltmeter calibration is shown in Fig. 1, where thermal power values, provided by E.D.F., are plotted versus the corresponding voltmeter data. The calibration parameters obtained by a linear fit are also given.

2.3 Map of the reactor core

The nuclear fuel consists of 110 T of uranium oxide tablets (diameter = 8.2 mm) enriched with ^{235}U and stacked in 4 m long, 1 cm wide assemblies. The standard enrichment for this type of reactor is 3.1%. Each fuel element contains 264 assemblies. About 1/3 of the 205 fuel elements are changed at the end of each cycle. The remainder is displaced towards the centre and new fuel elements are arranged in the outer part of the core, so as to get the fuel burning as uniformly as possible. For the start-up of the CHOOZ reactors, brand-new fuel rods were used. In order to reproduce the behaviour of reactors at equilibrium, where partially burned-up fuel is used, 137 less enriched elements are located at the centre (68 at 2.4% and 69 at 1.8%, while the standard enrichment is 3.1%). A schematic map of the reactor core is drawn in Fig. 2.

As shown in Fig. 2, the fuel assemblies of the most enriched elements are surrounded by a number of 12.7% Boron-doped steel rods, termed "poison" rods. The rods absorb the thermal neutron excess, thus accumulating ^{11}B, which has a negligible neutron absorption cross section, inside the core. Therefore the neutron absorption power of the poison rods diminishes with time partly compensating the fuel burn-up. The number of rods per fuel element varies according to the fuel loading as well as to the element position in the core. This was taken into account when computing fuel evolution.

2.4 Fuel evolution

The unit used to describe the aging of the fuel at nuclear reactors is the MW d/T, which measures the amount of energy per ton extracted from the nuclear fuel after its introduction into the reactor core. This quantity is called "burn-up" and is closely related to the fissile isotope composition of the fuel.

For any PWR reactor, the procedure to compute the evolution of the fuel in the core needs daily information provided by the reactor technical staff. This includes:

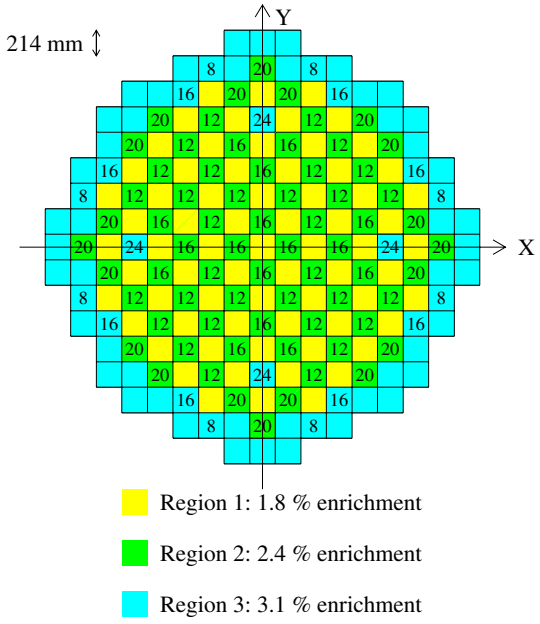

Fig. 2. Schematic view of the fuel rods in the core for the first cycle of the CHOOZ reactors. The number of Boron poison rods assembled with each fuel element is also indicated

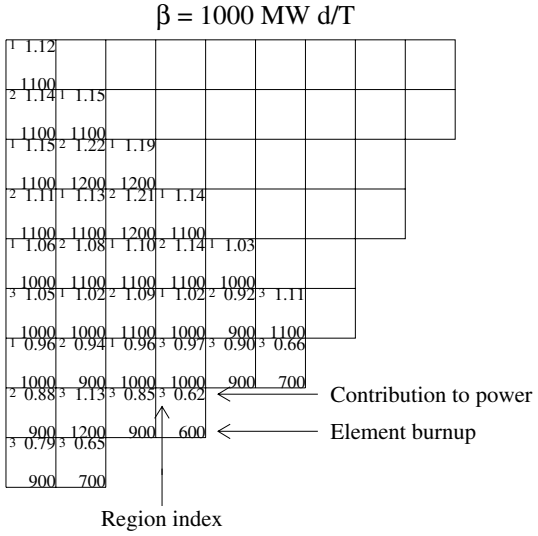

Fig. 3. Power distribution and burn-up values for the fuel elements in an octant of the CHOOZ reactor core at a certain step ($\beta = 1000$ of the first cycle). The contribution to the power of each element is normalized to have a mean value equal to one

Table 2. Energy release per fission of the main fissile isotopes (from [22])

isotope	energy (MeV)
^{235}U	201.7 ± 0.6
^{238}U	205.0 ± 0.9
^{239}Pu	210.0 ± 0.9
^{241}Pu	212.4 ± 1.0

– the daily cumulative burn-up, given as

$$\beta(t) \equiv \frac{1}{M_U} \int_0^t W_{th}(t')\,\mathrm{d}t', \qquad (3)$$

W being the thermal power, t the time since the start of reactor operation and $M_U = 110.26$ T the total amount of uranium in the core:

– the burn-up β_i and the relative contribution α_i to the power from the i-th fuel element, at several stages of the reactor cycle (an example is shown in Fig. 3).

These two inputs determine the daily burn-up of each fuel element. An example of the tables provided by E.D.F. for these quantities is given in Fig. 3. E.D.F. also provides another set of tables (at several burn-up stages) in which the relative power contribution f_k^i from the k-th fissile isotope for the i-th fuel element is given.

The number n_k^i of fissions per second for the i-th element for each isotope k can then be computed with the equation

$$n_k^i(\beta) = \frac{\alpha_i(\beta) f_k^i(\beta) W(t)}{\sum_k f_k^i(\beta) E_k}, \qquad (4)$$

where E_k is the energy release per fission for the k-th isotope, whose values are listed in Table 2. Adding the contribution of all the fuel elements yields the average number N_k of fissions per second for the k-th isotope. Contributions from other fissioning isotopes, such as ^{236}U, ^{240}Pu, ^{242}Pu, etc. amount to less than 0.1% and are therefore neglected.

To obtain the source spectrum, in addition to the average fission rate N_k of each of the four isotopes, we need the corresponding differential neutrino yield per fission $S_k(E_\nu)$. The next section explains how these spectra are evaluated.

2.5 The expected neutrino spectra

We used the so-called "conversion" approach which is the most reliable and recent method to determine the $\overline{\nu}_e$ spectrum at reactors. This method utilizes measurements of the electron spectrum emitted by a layer of fissile material activated by thermal neutrons. The experimental electron spectrum is then converted into the $\overline{\nu}_e$ one [23–25]. The most recent and precise measurements were reported by Schreckenbach et al.[26–28]. In the latter case thin foils enriched with the main fissile nuclei (about 1 mg) were exposed to an intense thermal neutron flux ($\approx 3 \cdot 10^{14}\,\mathrm{s}^{-1}$). A high-resolution ($\delta p/p = 3.5 \cdot 10^{-4}$) β-spectrometer was used to measure the momentum of the emerging electrons.

The β^- spectrum for each fissile isotope is approximated by the superposition of a set of hypothetical allowed branches with amplitude a_i and end-point E_0^i:

$$S_\beta(E_\beta) = \sum_i a_i S_\beta^i[E_\beta, E_0^i, \overline{Z}(E_0^i)], \qquad (5)$$

where S_β^i is the spectrum shape of the i-th branch and the summation is over the branches with end-point larger

than E_β. The spectrum weakly depends also on the charge $\overline{Z}$ (average charge of the β-decaying nuclei with end-point E_0^i) because of the Coulomb interaction in the final state. The measured electron spectrum is then used to determine the set of values $\{a_i, E_0^i\}$ by means of a fit procedure. Equation (5), with the introduction of the best-fit parameters, reproduces the measured spectrum to better than 1%.

The β^- spectrum for each individual hypothetical branch is then converted into the correlated $\overline{\nu}_e$ spectrum under the assumption that both the electron and the antineutrino share the total available energy E_0^i. Thus, for each branch with end-point E_0^i, the probability of emitting an electron with energy E_β is equal to the probability of having a $\overline{\nu}_e$ of energy $E_0^i - E_\beta$. Inserting the fit parameters into (5), one obtains

$$S_\nu(E_\nu) = \sum_i a_i S_\beta^i[(E_0^i - E_\nu), E_0^i, \overline{Z}(E_0^i)] \qquad (6)$$

These yields contain a normalization error of 1.9% stemming from the error on the neutron flux and from the absolute calibration uncertainty of the spectrometer. The conversion procedure also introduces a global shape uncertainty into the neutrino spectrum, beyond the inherent experimental errors. The main sources of this additional uncertainty, ranging from 1.34% at 3 MeV to 9.2% at 8 MeV, are the scattering in the nuclear charge distribution and the higher-order corrections (higher Coulomb terms and weak magnetism, for which an uncertainty of the order of the correction term itself was assumed).

This method was applied to obtain the neutrino yields of the ^{235}U, ^{239}Pu and ^{241}Pu fissions. The resulting spectra are presented in Fig. 4. Unfortunately, no experimental data is available for ^{238}U which cannot be fissioned by thermal neutrons. We must therefore rely on the theoretical predictions [29] to estimate the contribution to the $\overline{\nu}_e$ spectrum by the ^{238}U fission products. Although these predictions are less reliable than direct measurements, it should be noted that the contribution to the number of fissions, due to this isotope, is quite stable and never higher than 8%. Thus any possible discrepancy between the predicted and the real spectrum should not lead to significant errors.

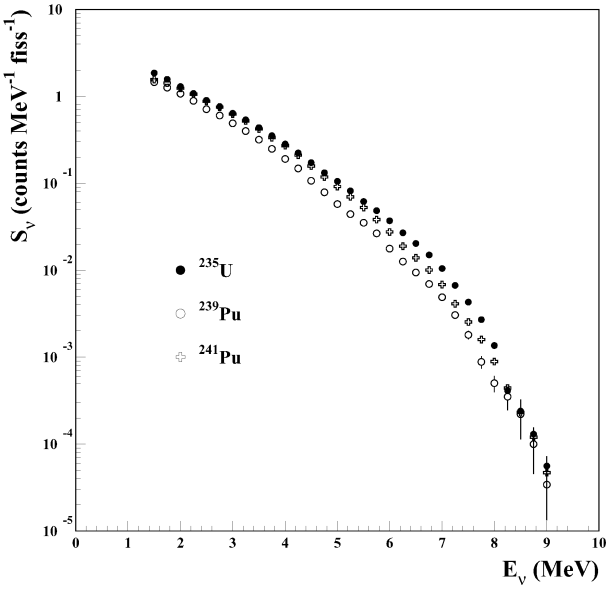

Fig. 4. Neutrino yield per fission of the listed isotopes, as determined by converting the measured β spectra [27,28]

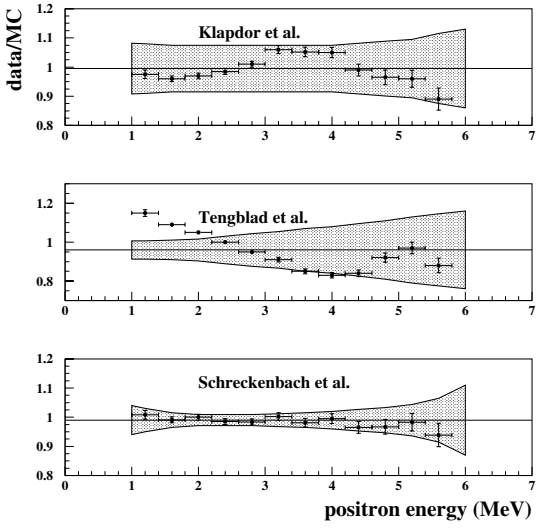

Fig. 5. Comparison of Bugey 3 data with three different reactor spectrum models. The error bars include only statistical uncertainties. The dashed lines are the quadratic sum of the quoted error of the models and the error due to the energy calibration

2.6 Systematic uncertainties of the neutrino spectrum

In past experiments at reactors, e.g. at Gösgen [30] and Bugey [31], more than 3×10^4 neutrino events were recorded at several reactor–detector distances R. Since no evidence for oscillations was observed and rates were found to be consistent with a $1/R^2$ law, these experiments can be interpreted as a check that a reactor is a neutrino source of characteristics known at a few percent level. The statistical accuracy obtained in these experiments makes it possible to use these results to discriminate between the existing models of reactor neutrino spectra.

The Bugey 3 collaboration [32] measured the positron energy spectrum at 15 and 40 m from the reactor core and compared its data with the results of a Monte Carlo simulation using the neutrino spectrum models proposed by [27,33,34]. As can be seen in Fig. 5, the data perfectly fit with the measurements made at Institute Laue Langevin at Grenoble (ILL), whereas there is a lower compatibility with other models.

An improved measurement of the integral neutrino flux was performed in 1993. The measurement used an integral type detector previously employed at the Rovno nuclear power plant [35] and subsequently moved to Bugey [36]. In that apparatus only neutrons were detected in ^{3}He counters, while positrons were not. The apparatus was installed

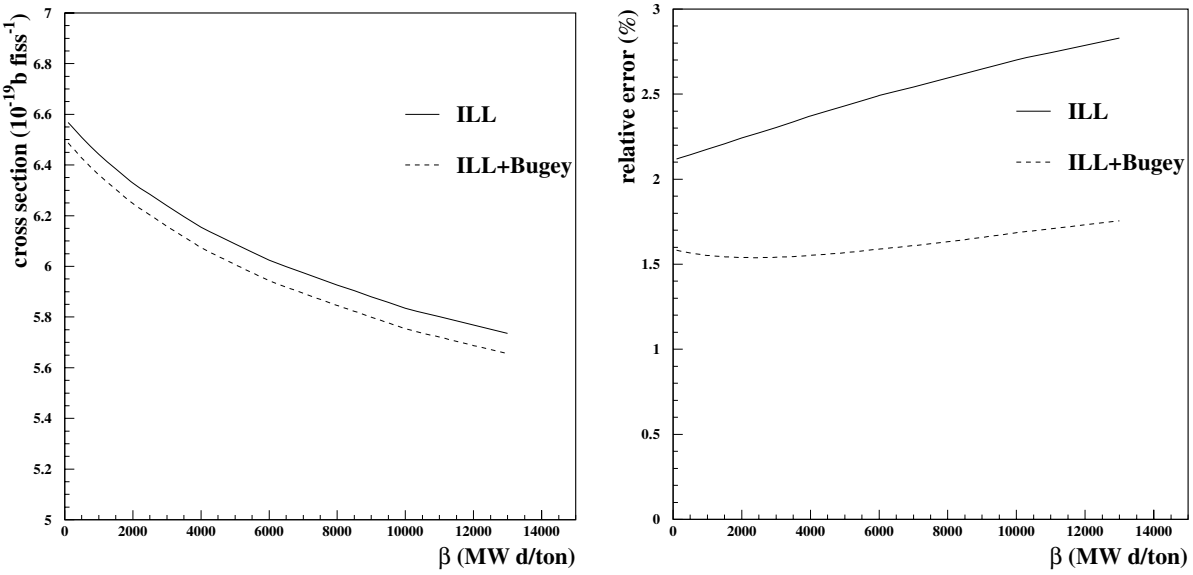

Fig. 6. Comparison of the combined (ILL+Bugey) reaction cross section with the ILL cross section (*left*) and their relative error (*right*) as a function of the first CHOOZ reactor cycle burn-up

at 15 m from the reactor core. About 3×10^5 neutrino events were collected so that the reaction rate was determined with 0.67% statistical accuracy. The neutrino event rate, n_ν, corresponds to a certain average fuel composition and is related to the cross section per fission σ_f and the number of target protons N_p by

$$n_\nu = \frac{1}{4\pi R^2} \frac{W_{th}}{\langle E_f \rangle} N_p \varepsilon \sigma_f, \tag{7}$$

The fuel composition, the thermal power W, the average energy per fission $\langle E_f \rangle$ absorbed in the reactor core and the distance R were provided by the E.D.F.–Bugey technical staff. The efficiency of the neutron detection ε was carefully measured; the overall accuracy was estimated to be 1.4%. The experimental result was then compared to the expected neutrino flux, which can be inferred by introducing into (7) the neutrino spectra S_k obtained at ILL [26–28], the cross section for the reaction (2) and the reactor parameters in (7). The expected cross section per fission for reaction (2) is given by

$$\begin{aligned} \sigma_f^{exp} &= \int_0^\infty \sigma(E_\nu) S(E_\nu)\, \mathrm{d}E_\nu \\ &= \sum_k f_k \int_0^\infty \sigma(E_\nu) S_k(E_\nu)\, \mathrm{d}E_\nu = \sum_k f_k \sigma_k \end{aligned} \tag{8}$$

where f_k refers to the contribution of the main fissile nuclei to the total number of fission, S_k to their corresponding $\overline{\nu}_\mathrm{e}$ spectrum and σ_k to their cross section per fission. The result of the measurement was $\sigma_f^{meas} = 5.752 \times 10^{-19}$barns/fission$\pm$1.4%, which perfectly agrees with the expected value ($\sigma_f^{exp} = 5.824 \times 10^{-19}$barns/fission$\pm$2.7%), and is twice as accurate as the predictions based on the knowledge of the neutrino spectrum.

We could therefore adopt the conversion procedure for the shape of the neutrino spectra but normalize the total cross section per fission to the Bugey measurement, i.e., after taking all the different reactors conditions into account.

In Fig. 6(left) the ILL cross section (8) and the combined (ILL+Bugey) cross section obtained for the CHOOZ reactors are plotted vs. the reactor burn-up. The average ratio of the two curves amounts to 0.987. By combining the uncertainty on the neutrino spectra, on the cross section for the reaction (2) and on the fission contributions f_k (which are of the order of 5%), we obtained the relative error on the neutrino detection rate, as a function of the fuel burn-up. As shown in Fig. 6(right), the average error decreases from 2.4% (ILL data alone) to 1.6% (ILL+Bugey). Other minor sources of errors come from the residual neutrino emission from long-lived fission fragments (dealt with in the next Section). However the reactor source can be considered to be known at a 2% level.

2.7 Neutrino spectrum time relaxation and residual neutrino emission

Another possible source of uncertainty of the neutrino flux is related to the residual emission due to the β^- decay of long-lived fission fragments. Taking this further contribution into account, the linear relation (7) between the prompt $\overline{\nu}_\mathrm{e}$ interaction rate and the current thermal power W no longer holds. Nevertheless, the $\overline{\nu}_\mathrm{e}$ spectra determined at ILL were derived after about 1.5 d exposure time, so that neutrinos from fission fragment decays of longer life are not included. The expected neutrino rate based on this model may thus be underestimated with respect to the experimental data. Fortunately the maximum neutrino energy is above the reaction (2) threshold only in a few cases since, as can be expected, the longer the lifetime,

Table 3. Time evolution of neutrino spectra relative to infinite irradiation time (from [37])

E_ν (MeV)	^{235}U			^{239}Pu		
	10^4 s	1.5 d	10^7	10^4 s	1.5 d	10^7
1.5	0.837	0.946	0.988	0.861	0.949	0.990
2	0.897	0.976	0.992	0.904	0.968	0.986
2.5	0.925	0.981	0.990	0.939	0.975	0.986
3	0.963	0.997	1.000	0.967	0.989	0.993
3.5	0.967	1.000	1.000	0.979	0.997	1.000

the lower the Q-value of the decay[1]. This effect has been evaluated by using the cumulative yields of the known long-lived fission fragments [37]; the results for ^{235}U and ^{239}Pu are summarized in Table 3. In particular, the reaction cross section σ_f computed by using (8) is probably lower than the effective one by $\approx 0.3\%$. This systematic shift affects the accuracy on the reaction cross section. We will then assume an overall and conservative 1.9% uncertainty on the integral neutrino rate.

2.8 The inverse beta-decay reaction

The detection of reactor antineutrinos is usually based on the reaction (2). This is the most suitable process since:

- it has the highest cross section in the energy range of reactor antineutrinos:
- provides a convenient time correlated pair of positron and neutron signals, which allows us to reject most of the background.

The antineutrino and the positron energy are related by

$$E_{\overline{\nu}_\mathrm{e}} = E_{\mathrm{e}^+} + (M_\mathrm{n} - M_\mathrm{p}) + \mathcal{O}(E_{\overline{\nu}_\mathrm{e}}/M_\mathrm{n}), \qquad (9)$$

where the infinitesimal term corresponds to the neutron recoil. Thus a measurement of the positron energy allows an accurate determination of the energy of the incoming antineutrino. The threshold for the reaction (2) is 1.804 MeV, equal to the nucleon mass difference plus the positron mass. In the low energy limit, the cross section for the reaction (2) may be written as a function of outgoing positron energy as follows:

$$\sigma(E_{\mathrm{e}^+}) = \frac{2\pi^2\hbar^3}{m_\mathrm{e}^5 f\tau_\mathrm{n}} p_{\mathrm{e}^+} E_{\mathrm{e}^+} (1 + \delta_{rad} + \delta_{WM}) \qquad (10)$$

The transition matrix element has been expressed in terms of the free neutron decay phase-space factor $f = 1.71465(15)$ [38] and lifetime $\tau_n = (886.7 \pm 1.9)$ s [39]. Two higher-order correction terms (both of 1% order of magnitude) are also included:

[1] This effect might be much more relevant in the case of experiments looking for neutrino elastic scattering interactions (i.e., measurement of the neutrino magnetic moment) and needs a more careful treatment

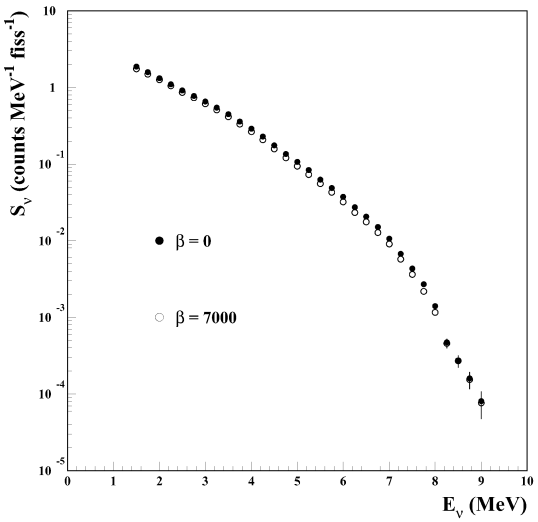

Fig. 7. Comparison between the neutrino spectrum at the beginning and during the first cycle of the CHOOZ reactors

(i) a radiative correction of the order of α, including an internal bremsstrahlung contribution, which can be approximated by

$$\delta_{rad}(E_{e^+}) = 11.7 \times 10^{-3} (E_{e^+} - m_e)^{-0.3} \qquad (11)$$

with the positron energy expressed in MeV [40] and

(ii) a correction for weak magnetism, arising from the difference $\mu = \mu_n - \mu_p = -4.705890(2)\mu_N$ between the anomalous magnetic moment of the neutron and the proton

$$\delta_{WM}(E_{e^+}) = -2\frac{\mu\lambda}{1+3\lambda^2}(E_{e^+} + \Delta + \beta p_{e^+})/M_p, \qquad (12)$$

where $\lambda = g_A/g_V = 1.2601 \pm 0.0025$ is the ratio of axial-vector and vector coupling constants and Δ is the nucleon mass difference [41].

The knowledge of the cross section is therefore much more accurate than the one of the $\overline{\nu}_\mathrm{e}$ spectrum, the major limitation being related to the uncertainty on τ_n (whose relative error is at most 0.3%).

2.9 Simulation of the $\overline{\nu}_\mathrm{e}$ spectrum

The expected neutrino spectrum was obtained by means of a Monte Carlo simulation of the reactor core in which we folded all the ingredients described in the previous sections, that is:

- the daily variation of the flux due to the fissile elements burn-up and to the live time of the apparatus;
- the contribution of the individual fuel elements according to their position inside the reactor core;
- the individual contributions of the different fissile elements in each fuel element to the neutrino flux.

Figure 7 shows the neutrino spectrum obtained at CHOOZ on the start-up day ($\beta = 0$) and at an intermediate step ($\beta = 7000$) of the first reactor cycle. Due

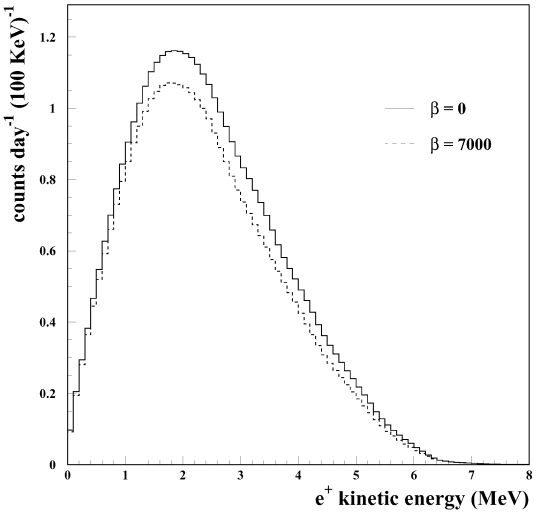

Fig. 8. Positron spectra at the startup and during the first cycle of the CHOOZ reactors at maximum daily neutrino luminosity

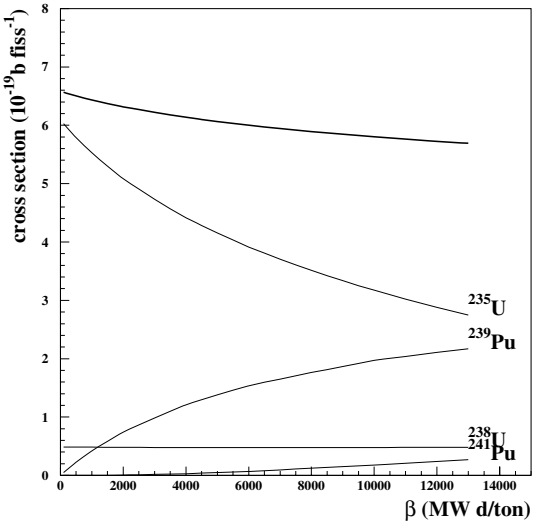

Fig. 9. Cross section per fission as a function of the reactor burn-up. The contribution of each fissile isotope is also shown

to the decrease of the ^{235}U concentration, a reduction of the neutrino interaction rate is observed and a softening of the neutrino spectrum is expected. The energy spectrum of the positrons coming from (2) is essentially the antineutrino spectrum shifted in energy and weighted by the cross section (10). So, following (7), each positron is assigned a weight given by

$$S_{e^+}(T_{e^+}) = \frac{N_p}{4\pi d^2}\sigma(E_\nu)S_\nu(E_\nu), \qquad (13)$$

where d is the distance from the neutrino production point to the detector and the positron kinetic energy T_{e^+} is given by (9). Figure 8 shows the positron yield obtained by generating the neutrino spectra drawn in Fig. 7 in one day of data taking with both reactors at full power. Although the generated neutrino luminosity is the same, the decrease of the positron yield with the reactor operating time is evident. The evolution of the positron spectrum must be followed very accurately in order to reproduce the hardware threshold effects on the positron detection. As an immediate consequence, also the integral neutrino interaction rate is expected to vary significantly during the reactor fuel cycle. A decrease of about 10% has been forecast for the cross section per fission (which is linear with the interaction rate, according to (7)) during the first cycle of the CHOOZ reactors, as shown in Fig. 9. The measured neutrino rate as a function of the burn-up will be shown and compared to the expected behaviour, under the no-oscillation hypothesis.

3 The experiment

3.1 The site

The detector was located in an underground laboratory about 1 km from the neutrino source (see Fig. 10). The

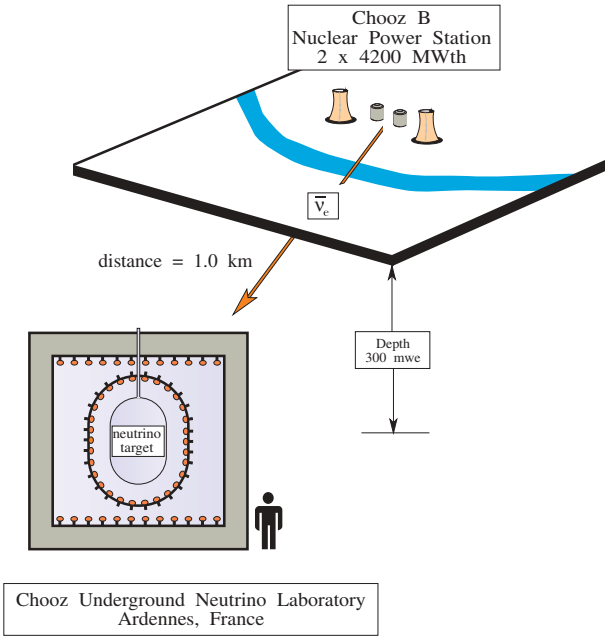

Fig. 10. Overview of the experiment site with indication of the source-detector distance and rock overburden

300 MWE rock overburden reduced the external cosmic ray muon flux by a factor of $\sim$ 300 to a value of $0.4\,\mathrm{m}^{-2}\mathrm{s}^{-1}$, significantly decreasing the most dangerous background, which is caused by fast neutrons produced by muon–induced nuclear spallations in the materials surrounding the detector. This cosmic ray shielding was an important feature of the CHOOZ site. As shown in Fig. 12, the rock shielding preserved the signal to noise ratio of previous reactor experiments, in spite of a reduction by a factor $\sim$ 100 of the neutrino flux due to the larger distance from the reactors. The characteristics of the site were thoroughly assessed before and after the set–up of the experiment. We measured the cosmic ray flux and angular dis-

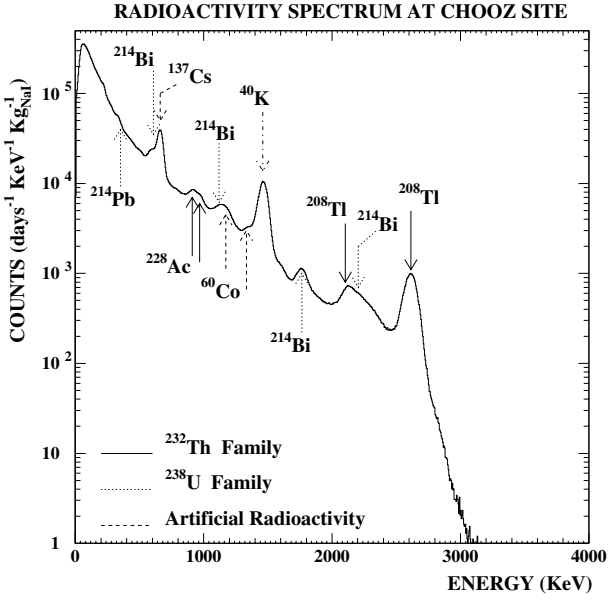

Fig. 11. Natural radioactivity spectrum recorded by a NaI crystal in the well hosting the detector

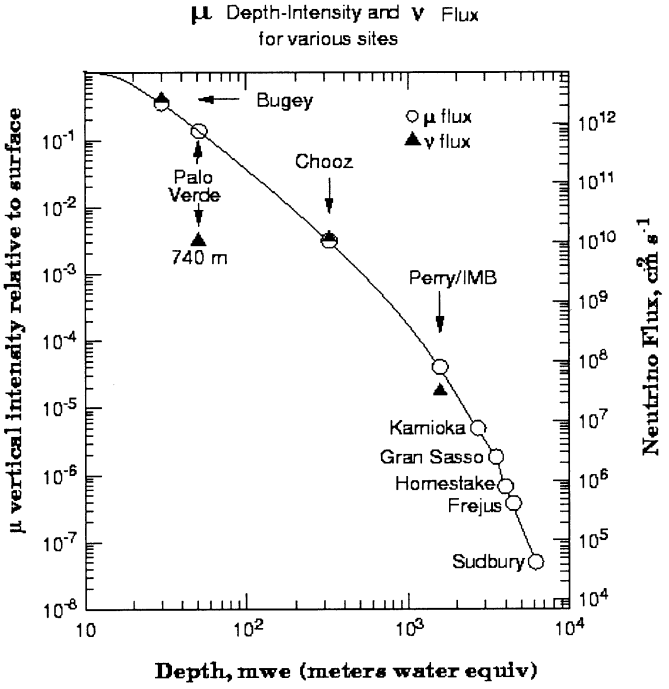

Fig. 12. Cosmic muon flux compared to the neutrino flux at the different underground experimental sites. In the CHOOZ case the lower neutrino flux is compensated by the reduction of the muon flux

tribution and the results were compared with predictions based on the rock structure above and around the site. The natural radioactivity background, the radon level in the tunnel and the intensity and orientation of the local terrestrial magnetic field were also measured. A geodesic survey was performed to determine the exact location of the underground experiment with respect to the two reactors and its orientation. All the information obtained in the preliminary studies were used to guide improvements in the detector and in the detector simulation.

The cosmic ray measurements were made for several days with a system of six Resistive Plate Chambers (RPC), each of area $1 \times 1\,\mathrm{m}^2$. The comparison of the experimental and expected angular distributions was fairly good, but some discrepancies persisted. A further geological study revealed the existence of several very high density rock layers ($3.1\,\mathrm{g/cm}^3$ the normal density being $2.8\,\mathrm{g/cm}^3$), whose positions and orientations fully explained the observed effects. The natural radioactivity spectrum was measured, at the position where the experiment had to be installed, by a $3 \times 3\,\mathrm{inches}^2$ NaI crystal. Natural radioactivity was rather high and the spectrum shows the normal natural radioactivity lines but also some artificial radioactivity contributions (see Fig. 11).

The magnetic field was measured by a rotating coil, pressurized-air device, and was found to be $B_{\parallel} = 0.178 \pm 0.007\,\mathrm{G}$ and $B_{\perp} = 0.388 \pm 0.007\,\mathrm{G}$.

3.2 The detector

The detector (Fig. 13) was installed in a welded cylindrical steel vessel 5.5 m in diameter and 5.5 m deep. The internal walls of the vessel were painted with high–reflectivity white paint. The vessel was placed in a pit 7 m in diameter and 7 m deep. To protect the detector from the natural radioactivity of the rock, the steel vessel was surrounded by 75 cm of low radioactivity sand (Comblanchien from Burgundy in France) and covered by 14 cm of cast iron. The detector comprised three concentric regions:

- a central 5–ton target in a transparent Plexiglas container (total mass = 117 kg) filled with a 0.09% Gd–loaded scintillator ("Region I");
- an intermediate 17–ton region (70 cm thick) equipped with 192 eight–inch PMT's (15% surface coverage, $\sim$ 130 photoelectrons/MeV), used to protect the target from PMT radioactivity and to contain the gamma rays from neutron capture ("Region II");
- an outer 90–ton optically separated active cosmic–ray muon veto shield (80 cm thick) equipped with two rings of 24 eight–inch PMT's ("Region III").

The apparatus was conceived as a liquid scintillator low energy, high-resolution calorimeter. The detector geometry (a central volume of scintillator surrounded by photomultipliers) is common to the Borexino, LSND and SNO detectors. The detector was simple and easily calibrated, while its behaviour could be well checked. Six laser flashers were installed in the three regions together with calibration pipes to allow the introduction of radioactive sources. The detector could be reliably simulated by the Monte Carlo method.

The target region contained a Gd-loaded liquid scintillator. The neutrino detection was based on the delayed coincidence between the prompt positron signal generated by reaction (2), boosted by the annihilation γ-rays, and

Table 4. Abundances and thermal neutron capture cross sections for the Gd isotopes

Gd isotope	$\sum_i E_{\gamma_i}$ (KeV)	Abundance (%)	Cross section (barns)	Relative intensity
152	6247	0.20	735	$3 \cdot 10^{-5}$
154	6438	2.18	85	$3.8 \cdot 10^{-5}$
155	8536	14.80	60900	0.1848
156	6360	20.47	1.50	$6 \cdot 10^{-6}$
157	7937	15.65	254000	0.8151
158	5942	24.84	2.20	$1.1 \cdot 10^{-5}$
160	5635	21.86	0.77	$3 \cdot 10^{-6}$

the signal associated with the γ-ray emission following the neutron capture reaction

$$\mathrm{n} + \mathrm{Gd} \rightarrow \mathrm{Gd}^{\star} \rightarrow \mathrm{Gd} + \sum_i \gamma_i \qquad (14)$$

The choice of a Gd-doping was to maximize the neutron capture efficiency; Gadolinium has the highest thermal neutron cross section. Moreover, the large total γ-ray energy ($\approx 8\,\mathrm{MeV}$, as shown in Table 4) easily discriminates the neutron capture from the natural radioactivity, whose energy does not exceed 3.5 MeV.

Region II was filled with an undoped high-flash point liquid scintillator. It provided a high-efficiency containment of the e.m. energy deposit; this was higher than 99% for positrons from $\overline{\nu}_{\mathrm{e}}$-interactions in Region I. The containment of the γ-rays due to the neutron capture on Gd was (on average) slightly lower than 95% for an energy deposit $E > 6\,\mathrm{MeV}$. The intermediate volume was bounded by the "geode", an opaque plastic structure serving as a support for the 192 inward-looking photomultiplier tubes (PMT from now on).

The outer volume, also filled with the undoped scintillator of Region II, was the "Veto" region (Region III). An additional 48 PMT's, arranged in two circular rings located at the top and the bottom of the main tank, detected the scintillation light associated with through-going cosmic muons. The Veto signal was used to tag and reject this major background source. The outer scintillator layer was also thick enough to shield the neutrino target against the natural radioactivity from the surrounding materials.

The inner detector volume was separated from Region II by a transparent 8 mm-thick vessel, a vertical cylindrical surface closed by two hemispherical end-caps. The outer radius of the cylinder and of the end-caps was 90 cm, the height of the cylinder was 100 cm; the inner volume was $5.555\,\mathrm{m}^3$, while the mass was 150 kg (empty). The vessel was made of an acrylic polymer (Altuglass), chosen for its excellent optical and mechanical properties and for its chemical resistance to aromatic compounds in the scintillator. The upper part of the vessel was fitted with a chimney (diameter $\phi = 70\,\mathrm{mm}$) to allow passage of filling pipes, calibration sources, temperature and pressure sensors.

The geode had the same shape of the target vessel, but a larger size; the cylinder height was the same, whereas the outer radius was 160 cm. The volume between the geode and the target was $19.6\,\mathrm{m}^3$. The geode surface (a drawing of which is shown in Fig. 13) had a total area of $42\,\mathrm{m}^2$ segmented into 32 panels; each panel was equipped with 6 8″ PMT's detecting the scintillation light produced in Regions I and II. The global PMT coverage was then 15%. Unlike the acrylic inner vessel, the geode was opaque so as to optically shield the inner regions from the veto scintillation light. The external surface was white-coated in order to enhance the light collection in Region III and improve the Veto rejection efficiency, while the black inner surface reduced light reflections, which could degrade the vertex resolution in the detector [43].

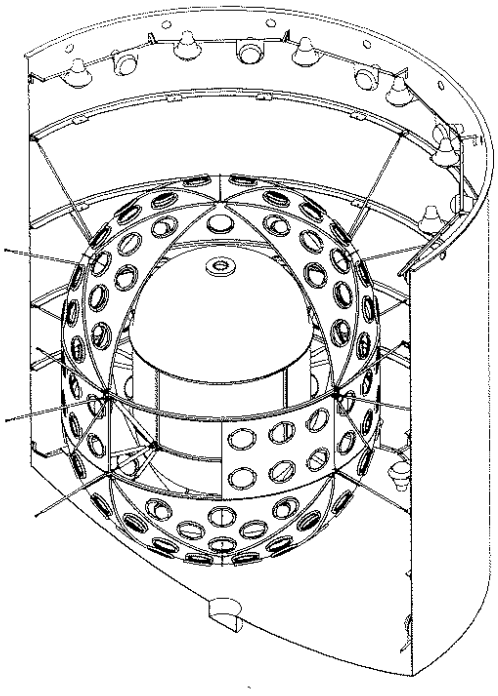

Fig. 13. Mechanical drawing of the detector; the visible holes on the geode are for the PMT housing (from [42])

3.3 The liquid scintillators

About 5 tons of Gd-loaded scintillator and 107 tons of unloaded scintillator were used in the experiment. The main properties of the two scintillators are listed in Table 5.

The solution of the Gadolinium salt $\mathrm{Gd(NO_3)_3}$ in hexanol as well as the mixing of the basic and aromatic compounds was performed in a dedicated hall close to the entrance of the underground tunnel. The amount of Gadolinium (0.09% in weight) was chosen to optimize neutron capture time and neutron detection efficiency. The measured values for the average capture time, path length and capture efficiency are listed in Table 5. A higher concentration would have required more alcohol, which could have lowered the high flash point of the solution below the limit imposed by safety regulations. Moreover, as we shall see, the presence of the nitrate ions in solution progressively deteriorated the optical properties of the scintillator. A

Table 5. Main properties of the liquid scintillators used in the experiment

	Gd-loaded	unloaded
Chemical content:		
basic	Norpar-15 (50% vol.)	Mineral oil (92.8% vol.)
aromatics, alcohols	IPB+hexanol (50% vol.)	IPB (7.2% vol.)
wavelength shifters	p-PTP+bis-MSB (1 g/l)	PPO + DPA (1.5 g/l)
Atomic mass composition:		
H	12.2%	13.3%
C	84.4%	85.5%
Gd	0.1%	
others	3.3%	1.2%
compatibility	acrylic, Teflon	
density (20 °C)	0.846 g/ml	0.854 g/ml
Flash point	69 °C	110 °C
Scintillation yield	5300 ph/MeV (35% of anthracene)	
Optical attenuation length	4 m	10 m
Refractive index	1.472	1.476
Neutron capture time	30.5 μs	180 μs
Neutron capture path length	$\sim$ 6 cm	$\sim$ 40 cm
Capture fraction on Gd	84.1%	

higher concentration would have further compromised the chemical stability of the scintillator.

A fundamental quantity for normalizing the neutrino event rate is the number of free protons in the target. An accurate evaluation of this number relies on precise measurements of the density and of the Hydrogen content of the Gd-loaded scintillator. The Hydrogen content was determined by combustion of scintillator samples; the presence of volatile elements (chiefly various types of alcohol) made this measurement particularly difficult. The value listed in Table 5 derives from averaging the dozen measurements performed on scintillator samples at different laboratories [44,45]. The overall relative uncertainty on the number of protons is 0.8%.

The scintillator transparency showed a degradation over time, resulting in a slight decrease of the photoelectron yield. The most probable cause is thought to be the oxidation by the nitrate ion. On one side, this forced us to repeatedly check the attenuation length in the detector by using calibration sources all along the acquisition period. The procedure followed is described in Sect. 6.4. In parallel, we made a systematic laboratory study of the chemical and optical stability of liquid Gd-loaded scintillators, which is also of interest for future low-energy neutrino detectors. The main optical properties were determined with both spectrophotometric and fluorimetric measurements. A Varian Cary 2200, UV-vis, 10 cm cell double-beam spectrophotometer was used to measure the absorbance of scintillators as a function of the beam light wavelength in the 350 ÷ 600 nm range, the absorbance being defined as

$$A \equiv -\log_{10} \frac{I}{I_0} \tag{15}$$

where I_0, I are the intensity respectively of the incident and the emerging beams. Several paired cells, with Suprasil quartz windows were used for these measurements. The measurement of attenuation lengths of a few meters by means of 10 cm cells required great care in the stability control of the apparatus as well as an accurate cleaning of the cell optical surfaces. Corrections were applied to take into account the multiple reflections inside the cell due to the different refraction indices of air, quartz and scintillator; the overall systematic uncertainty on the absorbance (including the spectrometer stability and the planarity of the quartz windows) was proved to be 0.5%. Examples of these measurements obtained with a laboratory-blended scintillator sample (using the same composition as the Region I scintillator) are shown in Fig. 14 (left).

An overall attenuation for the scintillation light was obtained by folding the measured attenuation at different wavelengths with the fluorescence spectra of the phosphores and the PMT photocathode sensitivity. The light attenuation as a function of the path is shown in Fig. 14 (right). Apart from the first $\sim$ 20 cm, needed for the absorption by the second shifter (bis-MSB), attenuation is best described by an exponential decrease giving an "effective" length. Measurements performed on the laboratory samples at different aging stages reproduced the attenuation length values obtained for the target scintillator within 15%.

The time variation of the light attenuation length in the detector is best reproduced by the function

$$\lambda(t) = \frac{\lambda_0}{1 + vt} \tag{16}$$

which accounts for the observed exponential decrease of the number of photoelectrons with time. Here v is proportional to the velocity of the chemical reactions responsible for the scintillator deterioration. The reaction kinetics is known to depend on temperature according to an exponential law:

$$v(T) = v_0 f(T) = v_0 a^{[(T-T_0)/10\,^\circ\mathrm{C}]} \tag{17}$$

where the index 0 labels the values at room temperature. It is also known that reactions occurring at time scales $\sim$ 1 s are accelerated by a factor $\sim$ 2 if the temperature is raised by 10 °C from room temperature.

We attempted to accelerate the aging effects by heating different samples at 60, 70 and 80 °C. As shown in Fig. 15, we found that an increase of 10 degrees in the

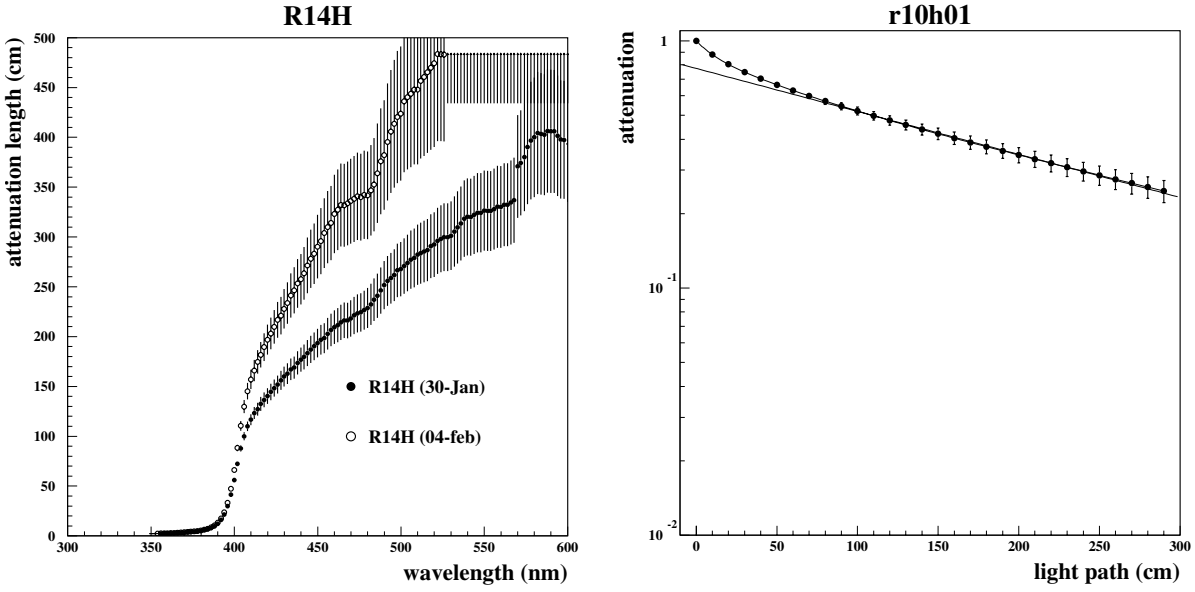

Fig. 14. Attenuation length vs. wavelength for the Gd-loaded scintillator (of the same type of that used at CHOOZ) at different aging stages (*left*) and scintillation light attenuation vs. path (*right*)

temperature corresponded to an acceleration factor $a \approx 3$ (instead of 2) in the aging rate. This discrepancy can be explained by simple thermodynamical arguments if (as in this case) such a reaction develops at room temperature on a time scale of a few months. The estimated value (at $T_0 = 20\,^{\circ}\mathrm{C}$) was $v_0 = (3.8 \pm 1.4) \cdot 10^{-3}\,\mathrm{d}^{-1}$, which was acceptable for a 1-year data-taking duration experiment like CHOOZ. This prediction turned out to be close to the value ($(4.2 \pm 0.4) \cdot 10^{-3}\,\mathrm{d}^{-1}$) obtained by direct measurements in the detector.

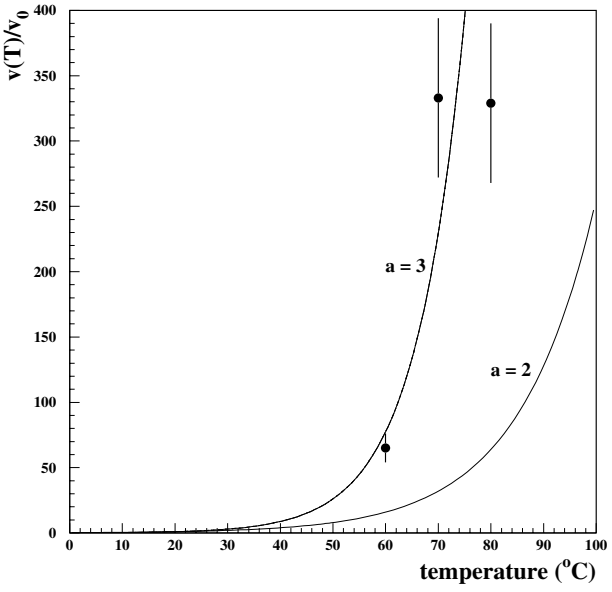

Fig. 15. Acceleration of the scintillator aging rate as a function of the temperature

3.4 The photomultiplier system

The PMTs provided both the charge and the time information needed to determine the event position and the energy deposit. The average photoelectron (pe) yield associated with a typical positron signal ($E \approx 3\,\mathrm{MeV}$) was ≈ 300, which corresponded to an average ≈ 1.5 pe at each PMT. The number of hit PMTs was $\approx 80\%$ of the total. As the PMTs had to work in a single pe regime, the most important feature for tube selection was the single pe resolution, i.e., the peak to valley ratio. Other important requirements were: low radioactivity and dark noise, high gain, large photocathode surface, low sensitivity to magnetic fields, good (but not ultra-fast) time properties. The EMI 9536KA B53 [46] turned out to be the best PMT for our needs. The high amplification ($\approx 10^7$, corresponding to $\approx 30\,\mathrm{mV}$ for a 1-pe pulse) matched the characteristics of the front-end electronics; the transit-time jitter ($\approx 8\,\mathrm{ns}$ FWHM at 1-pe level) was comparable with the scintillator decay time ($\approx 7\,\mathrm{ns}$). The PMT envelope was made of an ultra low-radioactivity glass (B53) at our request. PMTs were power supplied by the CAEN SY527 HV system (positive anode, grounded cathode), equipped with 16-channel cards A734P, providing a maximum of 3 kV; the HV channels were CAMAC controlled via the CAENET card C117B. The high voltage was distributed to the dynodes through a "tapered bleeder" progressive divider, with interdynode voltages progressively increasing in the last dynode stages. This divider was preferred to the linear one (with equal interdynode voltages), since it was proved to provide enhanced linearity at a still acceptable high voltage for the required gain. The divider consisted in a circular printed circuit board soldered to the PMT socket pins and glued to the back of the socket itself. The divider and the socket pins were enclosed in a

Plexiglass cylinder to prevent contact of liquid scintillator with all the components.

A PMT test facility [47] was designed to determine the relevant parameters of all the PMTs. The measurement program allowed the quantities listed below to be determined and thus to compare the results with the ones contained in the PMT test card given by the producer:

(i) the operating voltage corresponding to 30 mV pulse (on 50Ω) for a single pe;
(ii) the PMT noise level;
(iii) the relative light sensitivity (proportional to the photocathode quantum efficiency × pe collection efficiency);
(iv) the single pe pulse height spectrum and its peak to valley (P/V) ratio;
(v) the PMT time characteristics (time jitter and "walk" effects).

The results were used to define the optimal working conditions and decide a proper geometrical arrangement of all the PMT's in the detector. Since the light level of neutrino events in CHOOZ corresponded to a few photoelectrons at each PMT, it is at this regime that the listed parameters were determined. The best suited source was the Hamamatsu light pulser PLP-02 with a laser diode head SLD-041 emitting at 410 nm a wavelength close to the maximum photocathode sensitivity and to the maximum bis-MSB emission wavelength. Details of the features of this source, the coupling to the optical bench and to PMT housing structure can be found in [47]. The determination of the PMT relative sensitivity was cross-checked by using two additional "passive" light sources: a disk of NE110 scintillator activated by a low intensity ^{60}Co and a ^{241}Am α-source coupled to a NaI crystal. All our sensitivity measurements were found to be consistent with each other and with the quantum efficiency as measured by EMI.

3.5 Detector simulation

The Monte Carlo (MC) simulation of the detector is based on a Fortran code linked with the CERN GEANT 3.21 package [48]. The program allowed us to simulate the detector response for different particles, in particular for the positron and the neutron following an $\overline{\nu}_e$ interaction. The use of GEANT routines had a two-fold objective:

define the detector geometry and the physical parameters of the different materials (scintillators, acrylic, steel) in the detector and
track positrons, electrons and photons in the detector and evaluate the energy deposit in the scintillator.

A specially written routine was used to track secondary particles below 10 keV, the minimum cut-off energy allowed by GEANT, down to 1 keV, in order to better account for the scintillation saturation effects arising at low energies. The routine calculates the range corresponding to the particle energy and divides this range into 10 steps; the ionization loss is evaluated at each step, and the particle is tracked until its residual energy reaches 1 keV. Each energy deposit is then converted into the scintillation photon yield; ionization quenching effects are taken into account according to Birk's law, with $\beta = 1.3{\cdot}10^{-2}$ cm/ MeV derived from the measurements performed on the similar MACRO liquid scintillator [49].

Scintillation photons are isotropically generated and tracked up to the PMT surface. Effects due to light attenuation by the scintillators, due to reflection on the PMT glass, to the light refraction at the target boundary and to absorption on opaque surfaces (such as the Geode and the calibration pipes) are also simulated. The probability of detecting a photon hitting the PMT surface is weighted according to the quantum efficiency.

The MC code also includes the charge response of the digitizing electronics; the charge output for each event is formatted as for real data, which allowed us to reconstruct MC and real events by means of the same algorithm. The evaluation of the neutrino detection efficiencies strongly relies on MC evaluations; it was therefore crucial that the MC output was as close as possible to the data. The most important difference between the real and simulated geometry concerns the shape of the PMT's, assumed to be flat and lying on the geode surface (whereas the PMT glass is hemispherical and protrudes towards the centre by a few cm). As we will see, this approximation (needed to avoid a large waste of computing time) is also responsible for the fragility of the reconstruction algorithm in the case of events close to the PMTs.

User-defined routines [50] were introduced in the main MC code to follow the neutron moderation and capture processes. Tabulated cross section values were used for both elastic scattering and capture on Gd, H, C, O, Fe [51]. At each step (whose length depends on the total cross section at the neutron velocity) a decision is taken if either scattering or capture processes (or neither) arise. In the case of captures, γ-rays are emitted in cascade according to the de-excitation scheme of the nucleus involved; each photon is then tracked by GEANT routines. Captures on Hydrogen are followed by the emission of one 2.2 MeV γ-ray. The case of Gadolinium is harder to manage; the excited nucleus can decay to the ground state through a series of intermediate excited levels, both discrete and continuously distributed. Each capture event typically releases about three γ-rays with a total energy depending on which Gd isotope captures the neutron. The information used about the energy levels involved and the relative decay branches are taken from [52].

4 The trigger

The electronic system for the CHOOZ experiment collected and processed PMT output signals to select events due to neutrino interactions and to separate them from the background. The charge and time information provided by the PMT's were used to reconstruct the energy and position of each event.

The signature of a neutrino interaction relied on the delayed coincidence of two signals within a 100 μs time

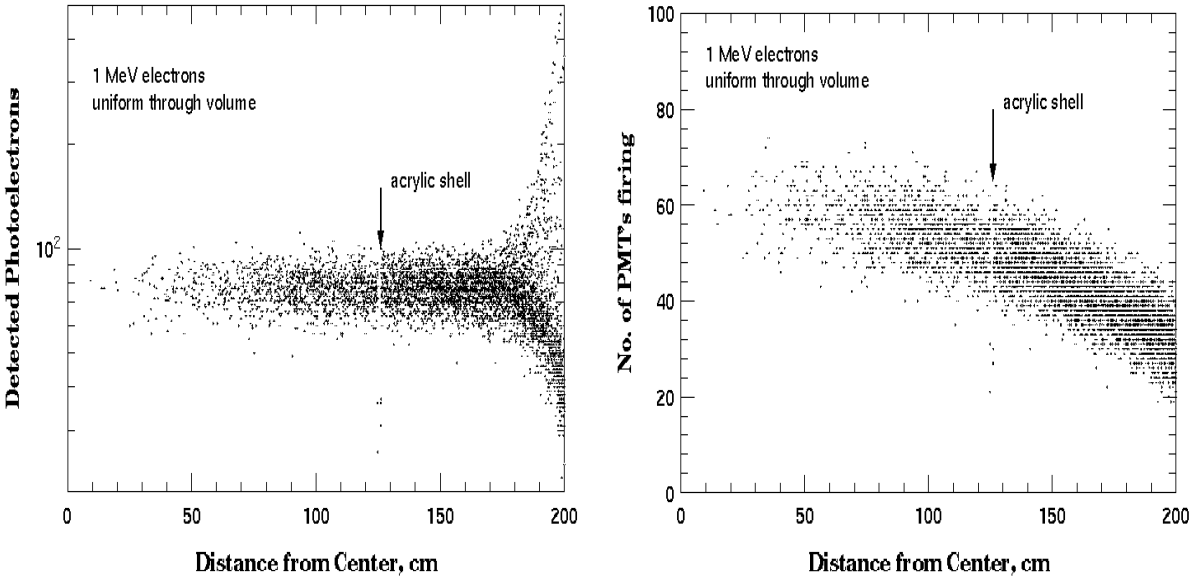

Fig. 16. Number of detected photoelectrons QSUM (*left*) and number of hit PMT's NSUM (*right*) for 1 MeV electron events, as a function of the distance from the detector centre

window: the former, due to the positron, has an average energy of about 3 MeV; the latter, due to the delayed neutron capture on Gadolinium, has a total γ-ray energy $\approx$ 8 MeV. The identification of this event combination was therefore based on a two-level trigger system; the first level selected events with an energy release $>$ 1.3 MeV (L1lo) or $>$ 3 MeV (L1hi); the occurrence of the sequence (L1lo,L1hi), within the 100 μs time window, generated the second level which triggered the data digitization and recording by the on-line system.

4.1 The first-level trigger

The electronic sum of the signals corresponding to photoelectrons detected by all PMT's gave a first rough measurement of the energy released by any event. A Monte Carlo simulation of electrons uniformly generated in the detector (whose results are summarized in Fig. 16) showed that the collected charge is linearly dependent on the energy deposit and almost independent of the position within Region I. In Region II this changes and the total number of photoelectrons for events within 30 cm from the PMT's can be as much as 10 times larger than for events at the centre. So, a trigger exclusively based on the charge information would not have rejected lower energy events generated close to the PMT surface.

A "topological" cut was then applied by also requiring a minimum number of hit PMT's. Figure 16 clearly shows that this extra condition preferentially rejected events close to the PMT's.

The first-level (L1) trigger was generated when both the charge and the PMT multiplicity fulfilled the above criteria. A simple schematic of the trigger circuit is presented in Fig. 17. The signals from each PMT were fed into the front-end electronics made of fan-in/out modules developed for the purpose. These modules provided a linear

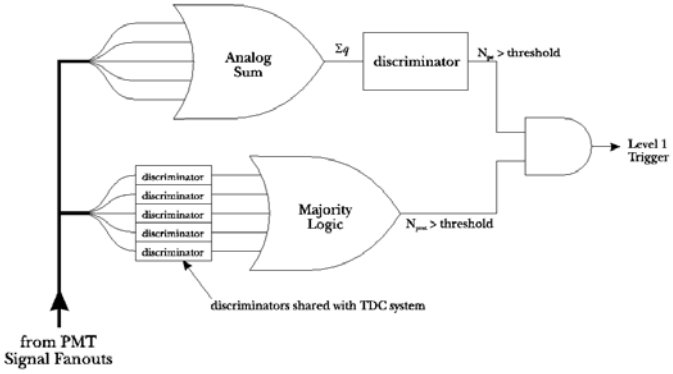

Fig. 17. First-level trigger scheme. Both the number of photoelectrons (QSUM) and the number of hit PMT's (NSUM) are required to fulfil a certain threshold condition

sum of the input signals (QSUM) whose amplitude was proportional to the total number of photoelectrons. The PMT multiplicity signal (NSUM) was obtained in a similar way. A copy of the PMT signals was fed into Lecroy LRS 4413 discriminators which had their threshold adjusted to 15 mV ($\approx$ one half of the single photoelectron amplitude). The linear sum of these discriminator outputs, whose amplitude was proportional to the number of channels over threshold on each discriminator board, formed the NSUM signal. The L1 trigger was finally asserted when both the resulting QSUM and NSUM signals exceeded the preset thresholds.

4.2 The second level trigger

The second-level (L2) condition (the one identifying the neutrino interactions) triggered on the occurrence of two events satisfying the L1 condition within a 100 μs wide

time window. This width represented a trade-off between a high neutrino detection efficiency and a high rejection of the accidental background. The positron–neutron delay followed an exponential distribution with an average $\tau \simeq 30\,\mu$s, therefore only 5% of the neutrino events were missed by the delayed coincidence window.

The L2 trigger logic is somewhat more complicated than the simple scheme just described. There were two different conditions for the fulfilment of the L1 trigger, corresponding to two different energy thresholds: the low condition (L1lo) roughly corresponded to 1.3 MeV and had a rate $\approx 130\,\mathrm{s}^{-1}$, the high condition (L1hi) corresponded to ≈ 3 MeV and had a rate $\approx 30\,\mathrm{s}^{-1}$. The higher threshold rejected the large background due to the natural γ-radioactivity (which practically ends with the 2.6 MeV ^{208}Tl line) and was sufficiently low to detect signals due to the neutron capture on Gd with almost full efficiency.

The L2 trigger was vetoed if some activity was present in Region III; this selection rejected events associated with cosmic rays. The VETO condition was satisfied whenever VSUM, the sum of the signals of the 48 PMT's located in Region III, was over a preset threshold. If no VETO condition occurred during a 1 ms time interval preceeding L2, the L2 triggered: the acquisition of further secondary particles went on for an extra-time of 100 μs and then stopped. The on-line processor took ≈ 80 ms to read all the electronics and to record the data on disk. During this time the computer *busy* condition was on and the acquisition of any further event was disabled.

Although a neutrino interaction corresponded to an L1lo-L1hi or L1hi-L1hi time sequence, the trigger logic enabled the acquisition of events with an L1hi-L1lo sequence as well, allowing a systematic study of the accidental background.

Finally, although the acquisition rate ($\approx 0.15\,\mathrm{s}^{-1}$) was rather low, it was large compared to the expected neutrino rate at full reactor power (≈ 30 events d^{-1}). The typical event size was roughly 30 Kbytes; the acquisition system could handle a daily amount of data in the order of 0.5 Gbytes. This capability was achieved through fast readout electronics and large storage devices.

4.3 Trigger for calibration runs

Acquisition schemes other than the normal neutrino trigger were required for calibrations or particular test runs. The trigger logic could be changed at the beginning of each run by loading an appropriate *trigger table*, a combination of the level trigger, veto and busy signals assembled by a dedicated logic unit Caen C542.

Neutron sources

Neutron sources were extensively used for detector calibration, both to define an absolute energy scale and to measure the neutron detection efficiency. A ^{252}Cf source was the most frequently used. This nucleus undergoes spontaneous fission, simultaneously emitting prompt neutrons and γ-rays below 10 MeV. The neutron multiplicity obeys Poissonian statistics with an average value 3.787 [53] and the kinetic energy is Maxwell-distributed, with an average energy equal to 1.3 MeV.

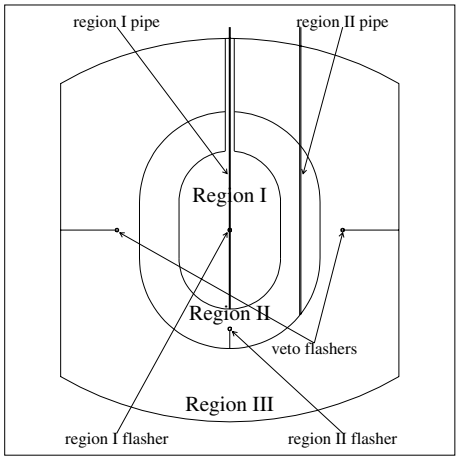

Fig. 18. Location of laser flashers and calibration pipes in the detector

We also used a Am/Be source. This emits neutrons, part of which follow the emission of a 4.4 MeV prompt γ-ray (see [54] and references therein for details).

With the source inserted in the centre of Region I, almost all the neutrons were contained and captured: some ($\approx 15\%$) were captured on Hydrogen, the majority on Gadolinium. The neutron binding energy was released in the form of γ-rays (one 2.2 MeV γ for H, an average of 3 γ's and $\sum_\gamma E_\gamma \approx 8$ MeV for Gd). In order to record events due to neutron capture on H as well, we defined a different trigger logic, by-passing the L1hi threshold condition; the L2 condition relied on the occurrence of two signals both satisfying the L1lo threshold. The "positron" role was, in this case, played by prompt γ's, while the second L1 trigger was provided by the first neutron capture (if within the 100 μs coincidence time-window).

The source could be inserted in the detector through two vertical calibration pipes: a central pipe, along the symmetry axis of the detector, and a parallel one, in Region II, just at half distance between the geode and the target boundary, as shown in Fig. 18. It was therefore possible to study the detector response anywhere along the z-axis in both regions. In particular, as we will see in the next section, calibration runs at different, known, positions allowed accurate tuning of the reconstruction algorithm and comparison with Monte Carlo forecasts.

γ sources

Daily calibration runs were performed by means of a ^{60}Co source, a well-known γ-emitter providing a low-energy calibration point at 2.5 MeV (the sum of 1.17 and 1.33 MeV simultaneous γ-lines). As we will see in the following sections, these runs were particularly useful to follow the detector evolution (a critical point because of the aging of

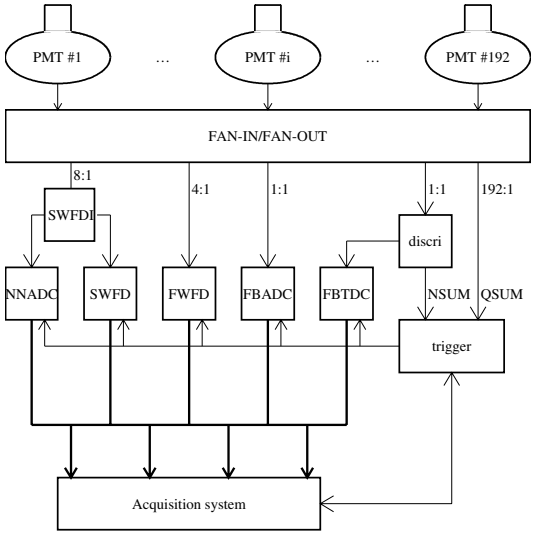

Fig. 19. Electronics layout for the CHOOZ experiment, including front-end, trigger and digitizing modules

the Gd-loaded scintillator), and to tune and check the trigger efficiency.

The neutrino trigger was not suited for acquiring these events, since the delayed neutron signal was missing. In this case, the L2 trigger was made to coincide with the L1lo trigger. With such a trigger we also recorded a great number of events due to γ-radioactivity natural background.

Laser

A laser based calibration system was also available. It consisted of a nitrogen UV Laser emitter ($\lambda = 337\,\mathrm{nm}$) with a repetition rate $\approx 10\,\mathrm{Hz}$ and a time jitter of less than 1 ns between the trigger and the light emission. The light intensity could be selected by using two variable neutral density filter wheels rotated by remote-controlled stepping motors. The attenuated light was fed to any one of six locations (remotely selectable), using UV quartz fibers (only two out of the four Veto flasher positions are shown in Fig. 18). At each position the bare fiber was terminated in a quartz vial filled with a dilute p-terphenyl solution, comprising the *flasher*. The fluorescence process shifted the laser wavelength to the same emission spectrum produced by scintillation, resulting in an isotropic point source having the same attenuation properties, time characteristics and PMT quantum efficiency as light generated by energetic particles. Time and pulse height calibrations of the detector could be carried out and monitored ona pulse-to-pulse basis. The monitors consisted of a photodiode, used to monitor laser intensity, and a separate fiber that directed light passing through the attenuator into a monitor PMT located next to the laser. Each of the monitors could be calibrated relative to an absolute standard.

In this case the L2 was given by the internal laser trigger after a delayed of $\approx 200\,\mathrm{ns}$ relative to the light emission.

4.4 The neural network trigger

This trigger [55] was intended to work as a fast acquisition filter for selecting events inside a fiducial volume, and secondly, it could be used for triggering upon coincidence of two L1lo triggers, therefore acquiring those neutrino events followed by neutron capture on Hydrogen (instead of Gadolinium).

This technique is not essential in the case of CHOOZ, since the amount of H-captures is $\approx 15\%$ of the total neutrino interactions in the target, but it could be important in on–going reactor experiments (namely KamLAND), where only a high-flash liquid scintillator (not Gd-loaded) is used.

The neural network algorithm was implemented on a VME parallel processor which reconstructed in $\approx 180\,\mu\mathrm{s}$ the energy and position of each event from the information provided by the NNADC digitizing system (see next section).

Due to the progressive deterioration of the Gd scintillator the potentialities of this trigger could not be fully exploited in this experiment.

5 Data acquisition

The data acquisition system consisted of various and distinct systems controlled by a VME-based processor:

NNADC $\rightarrow$ ADC units (VME),
SWFD $\rightarrow$ Slow (20 MHz) WFD units (VME),
FWFD $\rightarrow$ Fast (150 MHz) WFD units (FastBus),
FBADC $\rightarrow$ ADC units (FastBus),
FBTDC $\rightarrow$ TDC units (FastBus).

The PMT signals were fanned out and fed into each digitizing system, according to the diagram shown in Fig. 19. Since the PMT's were used in the grounded cathode configuration, their signals were fed to the circuits via AC couplings. For the first three systems, the signals from groups of PMTs were fanned in; for the NNADC's and SWFD's the PMT signals were linearly added by groups of 8, a PMT *patch*. This reduced the number of channels to 24. For the FWFD's the PMT groups varied from 4 to 8 during the experiment.

5.1 The on-line system

The acquisition system combined different bus standards (see Fig. 20); the digitizers listed above used both the VME and the FastBus standard, while the trigger electronics (including discriminators and logic units) was CAMAC based. The data were managed by a VME, OS-9 operating processor, whose central unit consisted of a Motorola 68040 microprocessor mounted in a CES FIC 8234 board. After completing the event readout, the data were sent through Ethernet to a dedicated SUN/Unix station and written on disk. A LabVIEW run controller was the interface between the user and the SUN; the controller also provided real-time information about the run and data quality.

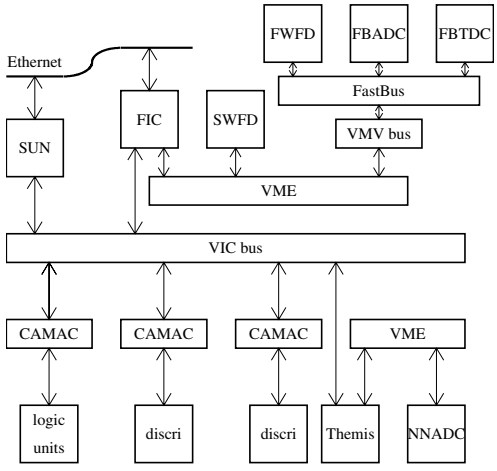

Fig. 20. On-line system architecture, with special reference to the different bus standards (VME, FastBus, CAMAC) and their interconnection (VIC,VMV)

5.2 The digitizing electronics

The NNADC's

The signals from the 24 PMT patches were sent to two VME 12-bit ADC banks, each composed of three 8-channel Caen V465 boards. Two banks were necessary to avoid any dead time between positron and neutron pulses, the time needed for the charge integration being $\approx 14\,\mu$s. The charge was integrated within a fast 200 ns gate. An external logic alternately switched the gate to the banks on the occurrence of an L1lo trigger. The digitized ADC values were arranged in a FIFO, thus allowing an internal multi-hit buffering in each bank. The ADC readout was performed by a Motorola 68030-based Themis TSVME133 VME processor board (referred to as "Themis" in Fig. 20). The TSVME133 was usually in a *wait* status until it received a VME interrupt generated when one of the two ADC banks was *not empty*.

The NNADC circuitry also included:

- 1 scaler Caen V560N:
- 1 flash-ADC Caen V534:
- 1 input/output register Caen V513:
- 1 Adaptive Solutions CNAPS parallel processor board.

The scaler and flash-ADC provided redundant information on the relative timing of events. The flash-ADC board was also used to sample the trigger signals (L1lo, L1hi, L2 and VETO). The other two boards were used to produce the Neural Network trigger.

The SWFD's

The Slow WaveForm Digitizer system used a set of 5 flash-ADC Caen V534 boards, with 20 MHz internal clock speed. These digitizers recorded the 30 Geode plus Veto patch signals from 100 μs before to 100 μs after the L2 trigger. All the input signals needed a proper stretching in order to fit to the inherent 50 ns resolution. Therefore these digitizers were essentially peak sensing devices and could not be used for pulse shape analysis. Extra channels recorded all the detector triggers.

The FWFD's

With their 155 MHz sample clock, these digitizers were the only equipment which could permit the study of pulse shapes. These units were equipped with an 8-page memory, the depth of one page being 206 ns, in order to record up to 8 events before the stop.

The FBADC's

The FastBus ADC system had four 96-channel Lecroy 1885F boards to separately measure the anode charge of each geode PMT. Even in this case, the boards were arranged in two alternating banks in order to record both events associated with the L2 trigger.

The FBTDC's

The FastBus TDC's recorded the time information of each geode PMT. Referring to Fig. 19, the input signals consisted of the logical (NIM) pulses generated by the trigger discriminators at minimum threshold. This system consisted of two 96-channel Lecroy 1877 multi-hit units able to record up to 16 hits in one single channel with 2 ns resolution.

6 Detector calibration

The reconstruction methods were based, for each event, on the VME ADC's digitization of the signals from the 24 patches which grouped the 192 PMTs looking at Region I. It was checked that this grouping does not significantly affect the quality of the reconstruction.

A good determination of the position and energy of each event and of the detection efficiency depends to a large extent on the knowledge of the main parameters of the detector (scintillator light yield and attenuation length, PMT and electronics gains).

6.1 PMT gain

The stability of the PMT gain was checked by periodic measurements of the single photoelectron pulse height spectrum of each PMT. Each spectrum was obtained by recording the PMT counting rate, out of a discriminator, as a function of its threshold. The data were taken by a LabVIEW code running in parallel with the main acquisition. No artificial light source was needed, since the single counting rate, at the one-pe level, due to the

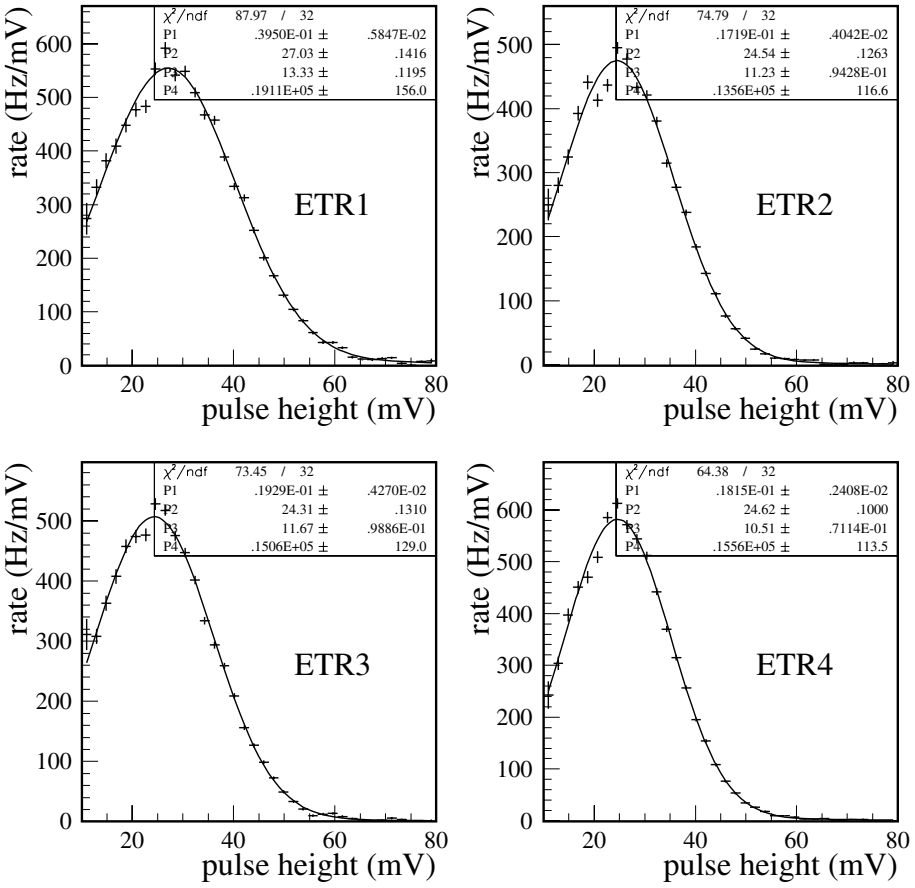

Fig. 21. Pulse height spectra for a sample of four PMTs

γ-radioactivity and to the dark noise, was $\approx 1\,\mathrm{kHz}$. Examples of these curves are shown in Fig. 21. The single pe spectra, obtained by differentiating the counting rate curves, were then fitted to get the PMT gains; values around 30 mV for the geode PMTs and 5 mV for the Veto ones were needed to match our front-end electronics. Figure 22 shows the distribution of the average single pe pulse height for the whole of the geode PMTs and its evolution since the beginning of the data taking. One concludes that the PMTs stabilized about one month after burn-in and that the asymptotic gain was $\approx 10\%$ lower than the starting value.

6.2 Determination of the photoelectron yield

A similar method was used to determine the photoelectron yield for events at the detector centre. We used the laser flasher at the detector centre as a calibrated light source. The laser provides its own trigger, so the counting rate is not affected by radioactivity.

An estimate of the number of photoelectrons N^i detected by each PMT comes from the probability of having zero photoelectrons when the average number is N^i. From Poisson statistics, we obtained for the i-th PMT

$$N^i = -\log\left(1 - \frac{N^i_{hit}}{\varepsilon^i N_{shot}}\right) \qquad (18)$$

where N^i_{hit}, N_{shot} are respectively the counts over threshold for that PMT and the number of laser shots. (18) includes also a detection efficiency ε^i, equal to the probability for a single pe pulse height to be over threshold, which can be evaluated for each PMT from the pulse height spectra shown in Fig. 21. The light intensity was kept at a level of about 0.5 pe/PMT so as to increase the sensitivity of the method. This number was divided by the energy deposit corresponding to the light intensity in order to determine the absolute light yield. As an energy reference we used the 2.5 MeV ^{60}Co "sum" line. By averaging the number of photoelectrons all over the PMTs, we obtained (0.65 ± 0.03) pe/MeV/PMT and a yield of (125 ± 5) pe/MeV.

6.3 ADC calibration in a single photoelectron regime

Calibration runs using the laser at a low intensity were periodically performed to test the single photoelectron gain and to calibrate the VME ADCs. The good ADC resolution and the high PMT gain allow us to distinguish the contributions to the ADC spectra due to different numbers of photoelectrons. A sketch of these spectra is presented in Fig. 23. The fit function results from the sum of a pedestal and a number of pe-distributions; each of these terms is represented by a Gaussian function (weighted according to Poisson statistics) whose peak position is linear with the number of photoelectrons.

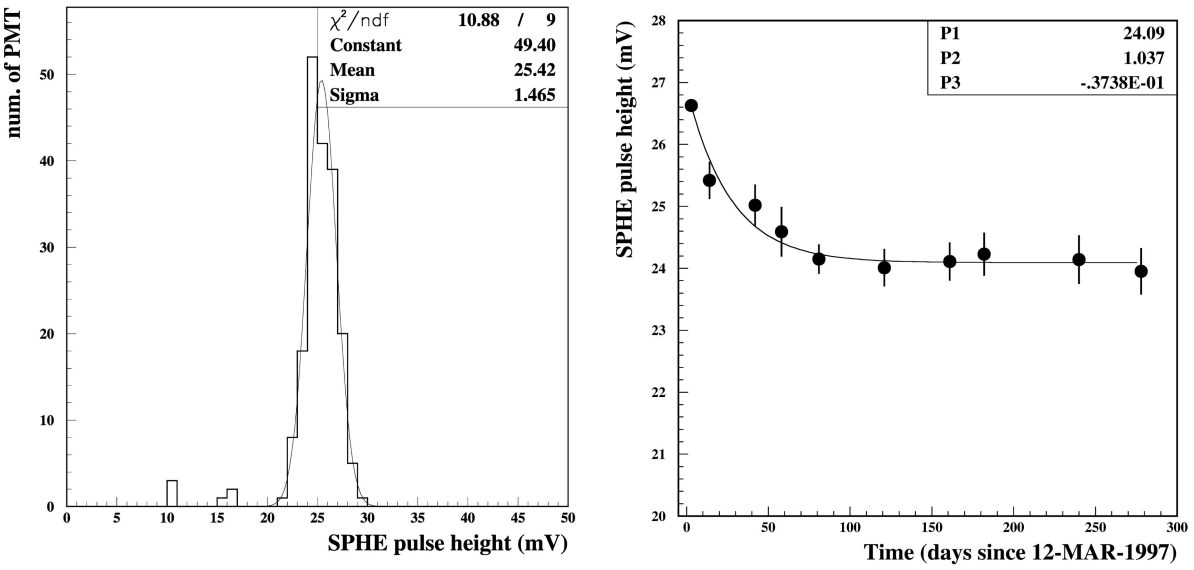

Fig. 22. Distribution of the single pe peak for all PMTs (*left*) and its time evolution since the start of data taking (*right*)

Apart from the ADC calibration, the fit also provides an independent determination of the number of photoelectrons collected by each PMT patch which is consistent with the measured photoelectron yield.

6.4 Light attenuation in the Gd-loaded scintillator

The degradation of light transparency in Region I (see Sect. 3.3) was regularly monitored in the apparatus by recording the number of photoelectrons associated with the ^{60}Co γ-line, as shown in Fig. 24.

The light absorption of Region I scintillator was periodically measured throughout the acquisition period. The method we used consisted in displacing a light source along the calibration pipe and in recording the charge detected by the top and bottom PMT patches. If we assume an exponential light attenuation (which is a good approximation for a light path longer than 10 cm, as already remarked), these charge values are related by the simple expression

$$\frac{Q_T}{Q_B} = \frac{\Omega_T}{\Omega_B} \exp\left(\frac{d_T - d_B}{\lambda_{Gd}}\right) \qquad (19)$$

$\Omega_{T,B}$ being the solid angle subtended by the top (bottom) patch PMTs and $d_{T,B}$ the average distance between these PMTs and the source position.

For this measurement we used a radioactive source, namely ^{252}Cf. This source was preferred to a γ source (such as ^{60}Co) since the double signature, provided by the prompt γ's and the neutron captures, makes the identification of source events much easier. The ^{252}Cf neutron emission and capture, the involved light paths and solid angles were simulated by the MC method.

The results obtained from different measurements are displayed in Fig. 25, superimposed on the exponential best-fit curves according to (19). The charge values in use are those corresponding to the 2.2 MeV γ-line due to the neutron capture on Hydrogen. We did not use the 8 MeV line in order to reduce systematics due to ADC saturation effects which might have arisen when the source approached the edges of Region I. The fitted λ_{Gd} values are plotted versus time in Fig. 26. The time evolution of the absorption length was fitted by the empirical function (16) (already used in the laboratory test). By taking the λ_{Gd} values, at the beginning and at the end of the experiment, one can estimate a 35% reduction in the photoelectron yield, in agreement with the measurement of the QSUM for events at the detector centre (Fig. 24).

6.5 Electronics amplification balancing

The electronic gain may differ from patch to patch and slightly vary with time because of the behaviour of the active electronic components in the circuits treating the signals from the PMTs. Amplification balancing factors were obtained three times a week using the ADC charge values corresponding to the 8 MeV line peak generated with the ^{252}Cf source at the detector centre.

7 Event reconstruction techniques

7.1 The standard minimization algorithm

The standard algorithm uses a maximum likelihood method to reconstruct the energy E and the vertex $\vec{x}$ of an event. The likelihood is defined as the joint Poissonian probability of observing a measured distribution of photoelectrons over the 24 patches for given $(E, \vec{x})$ coordinates in the detector. So, for an event occurring at time t after the start of data taking, we can build a likelihood function as follows:

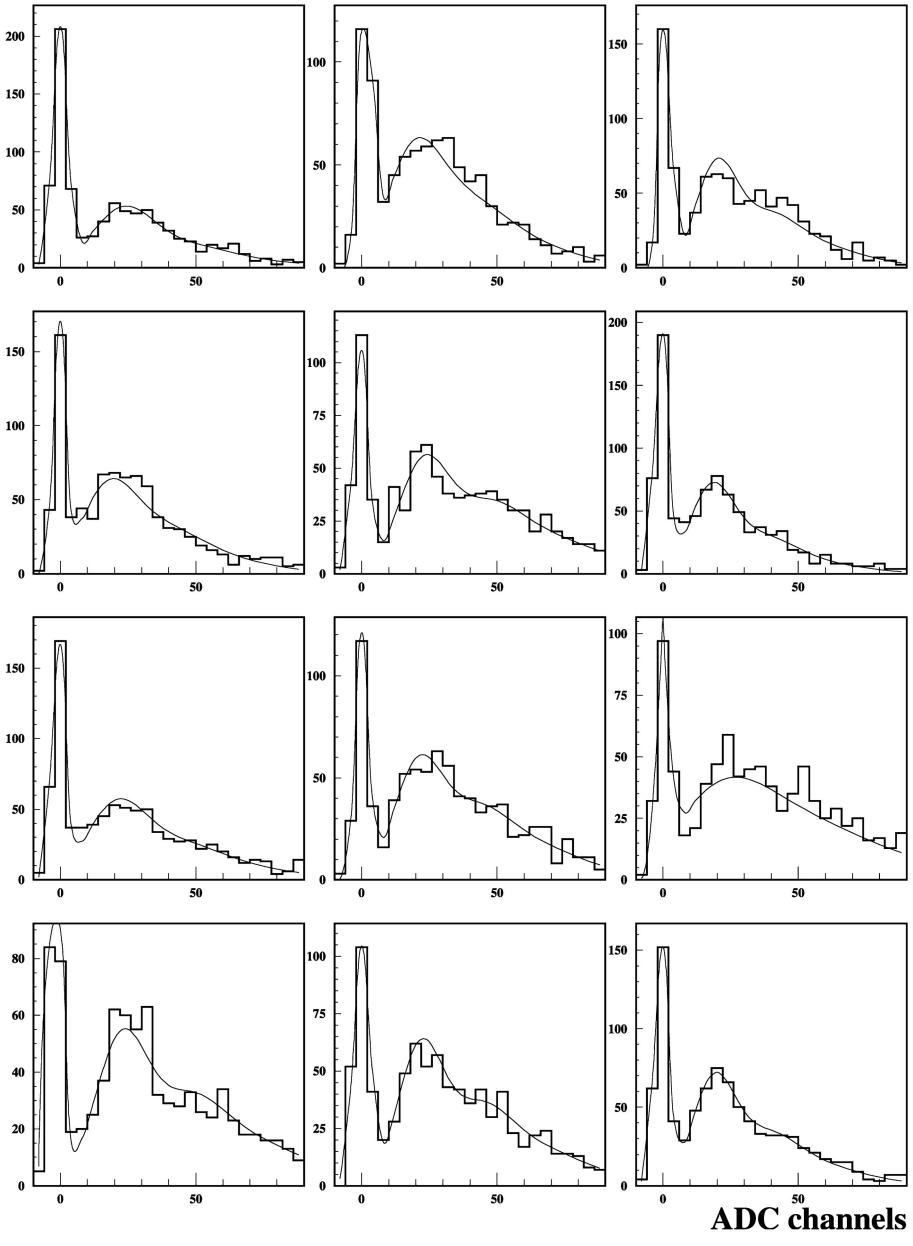

Fig. 23. ADC spectra obtained with a laser calibration, where the single pe peak is clearly visible. The fitting function results from the sum of the pedestal and the first three photoelectrons

$$\mathcal{L}(N;\overline{N}) = \prod_{j=1}^{24} P(N_j;\overline{N}_j(E,\overrightarrow{\mathrm{x}},t)) = \prod_{j=1}^{24} \frac{\overline{N}_j^{N_j}}{N_j!} e^{-\overline{N}_j} \tag{20}$$

where N_j is the observed number of photoelectrons and $\overline{N}_j$ the expected one for the j-th patch, given an event $(E,\overrightarrow{\mathrm{x}},t)$. The reason for using a Poissonian instead of Gaussian statistics is due to the frequent occurrence of low energy events, with low number of photoelectrons detected by some PMT patches.

The values N_j are obtained from the data recorded by the VME ADC's by applying the reference ADC gain g_0 and the balancing factors f_j: so

$$N_j = \frac{Q_j}{g_0 f_j(t)} \tag{21}$$

The predicted number of photoelectrons for patch j is computed by considering a local deposit of energy, resulting in a number of visible photons which are tracked to each PMT through the different attenuating Region 1 and 2 scintillators. Therefore

$$\overline{N}_j = \alpha E \eta \sum_{k=1}^{8} \frac{\Omega_{jk}(\overrightarrow{\mathrm{x}})}{4\pi} \exp\left(-\frac{d_{1jk}(\overrightarrow{\mathrm{x}})}{\lambda_{Gd}(t)} - \frac{d_{2jk}(\overrightarrow{\mathrm{x}})}{\lambda_{Hi}}\right) \tag{22}$$

where

E	is the energy deposited in the scintillators,
α	is the light yield of the scintillator,
η	is the average PMT quantum efficiency,
Ω_{jk}	is the solid angle subtended by the k-th PMT from the position,

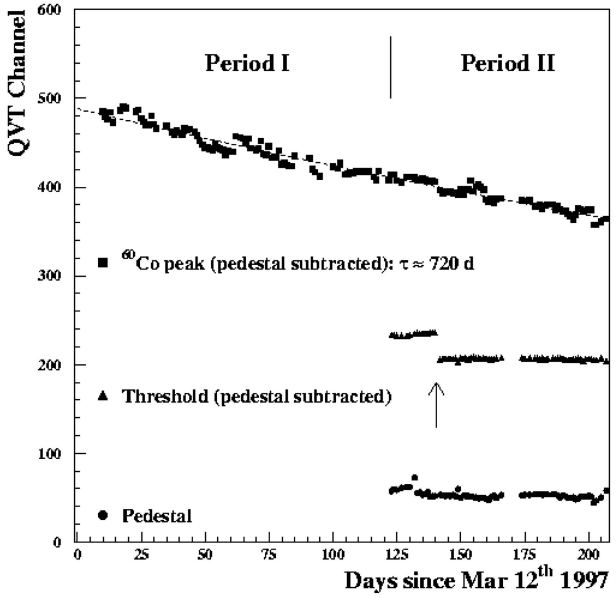

Fig. 24. Peak associated with the ^{60}Co 2.5 MeV line, as a function of time, as measured by means of a Lecroy QVT. The detected charge follows an exponential decrease, with decay time ≈ 720 d

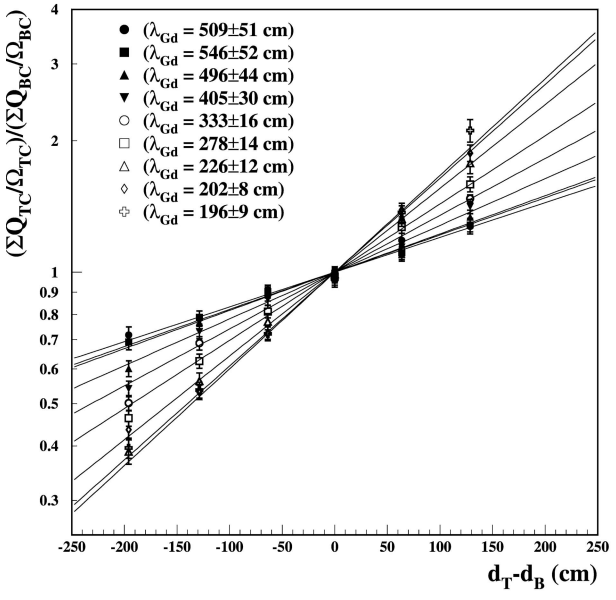

Fig. 25. Attenuation length measurements at different stages of the data taking period

d_{1jk} is the path length in Region I,
d_{2jk} is the path length in Region II,
λ_{Gd} is the attenuation length in Region I scintillator,
λ_{Hi} is the attenuation length in Region II scintillator.

To reduce computing time PMTs are considered to be flat and the solid angle is approximated by the following expression

$$\Omega_{jk} = 2\pi \left(1 - \frac{d_{jk}}{\sqrt{d_{jk}^2 + r_{PMT}^2 \cos\theta}} \right) \qquad (23)$$

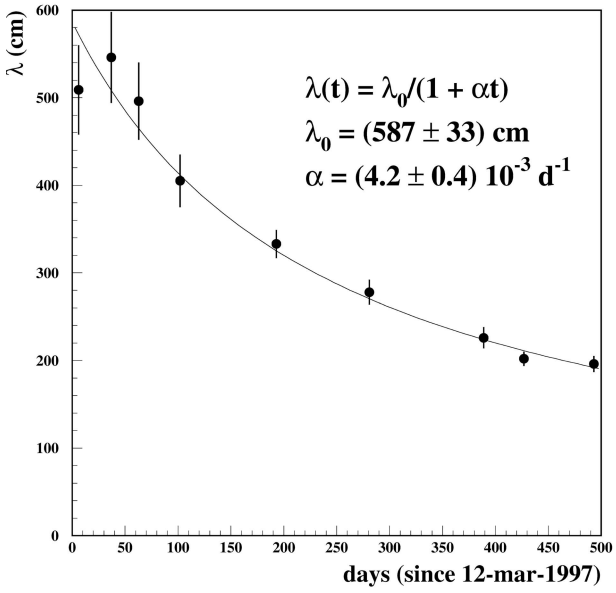

Fig. 26. λ_{Gd} versus time with best-fit function superimposed

r_{PMT} being the PMT photocathode radius, θ the angle between the event-PMT direction and the inward unit vector normal to the PMT surface and $d_{jk} = d_{1jk} + d_{2jk}$.

Instead of directly using (20) it is more convenient to exploit the "likelihood ratio test" theorem to convert the likelihood function into a form which obeys the χ^2 distribution [56]. We let N_j be the best estimate of the true (unknown) photoelectron distribution and form the likelihood ratio λ defined by

$$\lambda = \frac{\mathcal{L}(N; \overline{N})}{\mathcal{L}(N; N)} \qquad (24)$$

The "likelihood ratio test" theorem states that the "Poissonian" χ^2, defined by

$$\chi^2 = -2 \log \lambda = 2 \sum_{j=1}^{24} \left[\overline{N}_j - N_j + N_j \log \left(\frac{N_j}{\overline{N}_j} \right) \right], \qquad (25)$$

asymptotically obeys a chi-square distribution [57]. It is easy to prove that the minimization of χ^2 is equivalent to maximization of the likelihood function, so that the χ^2 statistic may be useful both for estimating the event characteristics and for goodness-of-fit testing.

We used the MIGRAD minimizer provided by the CERN MINUIT package [58] to minimize (25). The search for the minimum χ^2 proceeds through the computation of the first derivatives of (25). This routine proved very powerful, provided the starting values for the fit parameter are accurate. We studied the χ^2 profile by reconstructing Monte Carlo generated events. Several relative minima were found, most of them differing by more than 1σ from the generated $(E, \overrightarrow{x})$ coordinates. This is the reason why a suitable choice of these starting values is crucial in event reconstruction. In our case, an indication of the event position comes from the asymmetry of the charge distribution: no significant asymmetry will be visible for

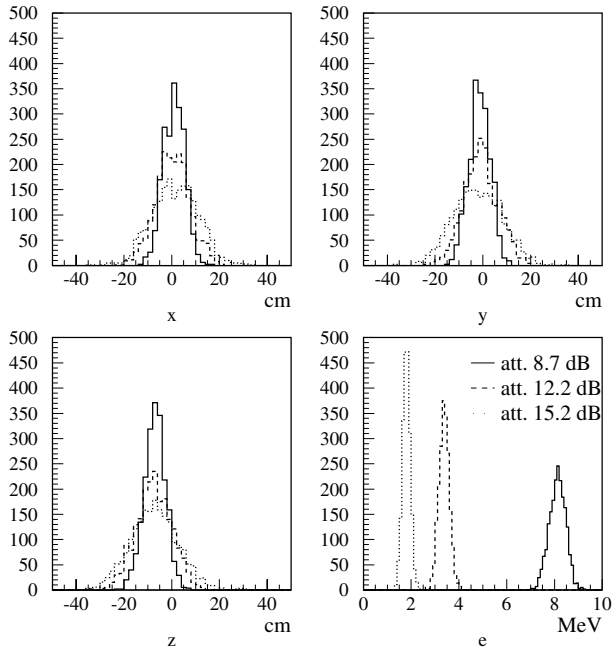

Fig. 27. Comparison of position and energy distributions for runs with the laser flasher at the detector centre, corresponding to three different light intensities

events at the centre while the charge distribution will be more and more asymmetric for events approaching the detector boundary. We subdivided the PMT patches into 6 "superpatches", two patches for each coordinate, and built the starting point for the i-th coordinate according to the following equation:

$$x_{i0} = \frac{\sqrt{Q^i_+} - \sqrt{Q^i_-}}{\sqrt{Q^i_+} + \sqrt{Q^i_-}} D^i, \; i = 1, 2, 3, \qquad (26)$$

where the indices $+-$ refer to the opposite superpatches of the i-th axis and D^i is the half size of the detector along that axis. Once the x_{i0} corresponding to the starting position is known, the starting energy value is obtained from (22) after replacing $\overrightarrow{x}$ with $\overrightarrow{x}_0$ and $\overline{N}_j$ with N_j. The event reconstruction was tested by analysing events generated with calibration sources in various positions inside the detector. Let us review the results. Distributions of reconstructed events generated by the laser flasher at the detector centre are presented in Fig. 27. The standard deviation of the distributions shown gives an indication of the resolution, both in energy and position. The fit yields $\sigma_x \approx 4\,\mathrm{cm}$ for each coordinate and an energy resolution $\sigma_E \simeq 0.33\,\mathrm{MeV}$ at an equivalent energy of 8.1 MeV in which the statistical fluctuations in the number of photoelectrons prevail. Photoelectron statistics also affect the position resolution. The effect is clearly visible in the data taken with the same laser flasher for three different light intensities (in Fig. 27 a larger filter attenuation corresponds to a lower intensity). As can be seen in Fig. 27, the average z coordinate is displaced by 7 cm from the nominal position; this is due to the effect of the

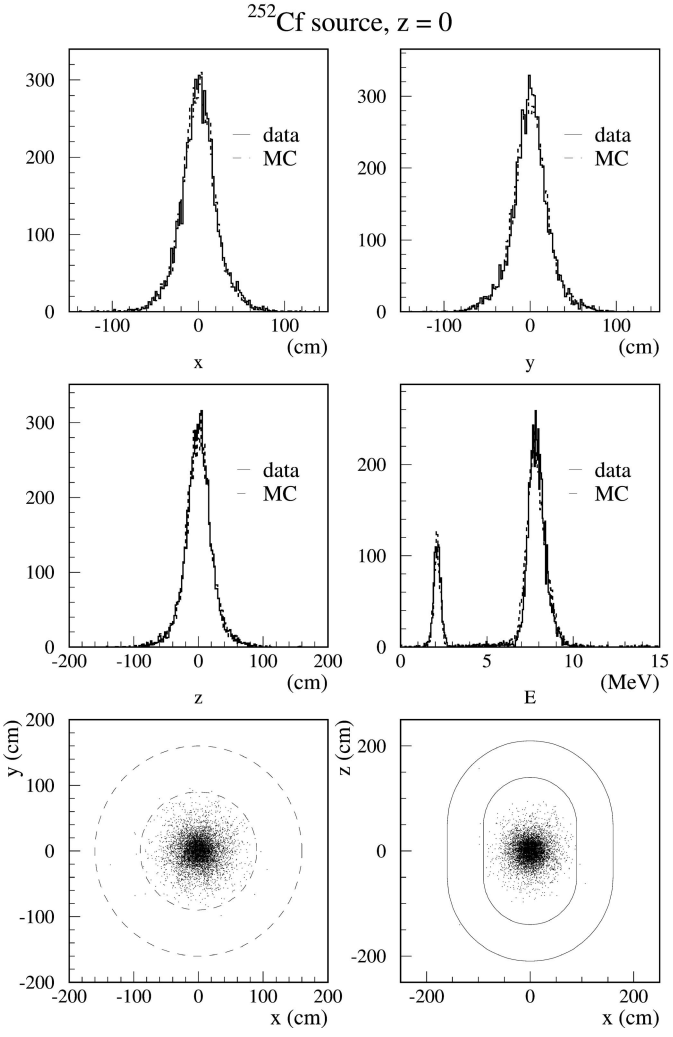

Fig. 28. Data and Monte Carlo distributions of neutron events with the ^{252}Cf source at the detector centre. Dashed and solid lines in the bottom figures represent respectively the top and the side view of the edge of the target and the geode

shadow of the flasher already mentioned; in this case, the flasher points downward, thus producing a shadow in the upward direction and displacing the event below the true source position. In Figs. 28, 29 we report the results of the calibration runs with the ^{252}Cf source at two different positions ($z = 0, -80\,\mathrm{cm}$) along the calibration pipe. The position distribution is Gaussian for all the coordinates, with $\sigma_x \approx 19\,\mathrm{cm}$. An equivalent number of neutrons was generated, at each position, by our Monte Carlo code and similarly analysed. The figures also display the Monte Carlo data to emphasize the agreement between data and expectations.

The energy spectra show the energy lines due to neutron capture on Gd and H. The shape of the Gd-capture energy spectrum, as pointed out in Fig. 30, results from the superimposition of γ lines due to neutron capture on ^{157}Gd and ^{155}Gd (see Table 4 for a reference). Due to the scintillator saturation (see Sect. 3.5) the fitted peak values are $\approx 2.5\%$ lower than the nominal ones.

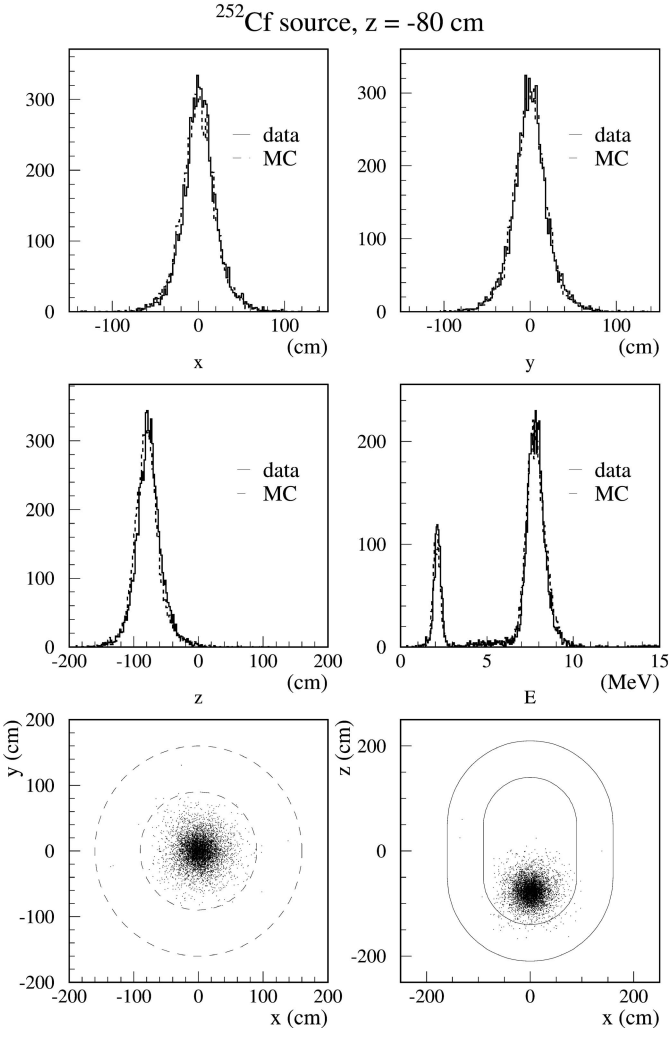

Fig. 29. Same as before, with the source at $z = -80\,\mathrm{cm}$

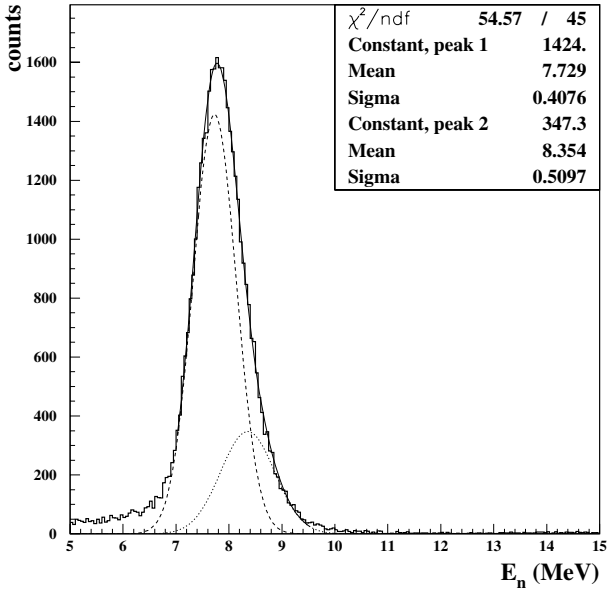

Fig. 30. Reconstructed energy spectrum for events associated with neutron capture on Gd. Contributions from γ-lines at 7.94 MeV (capture on ^{157}Gd) and 8.54 MeV (capture on ^{155}Gd) are singled out. The double-Gaussian fit parameters are also shown

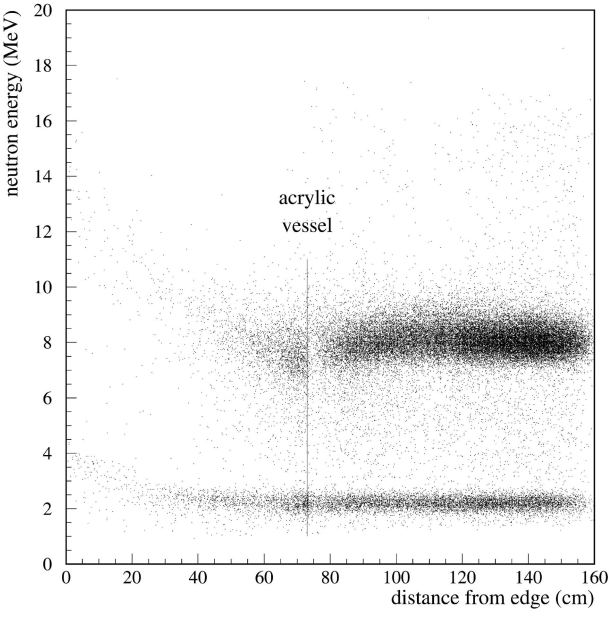

Fig. 31. Energy versus distance from edge for neutron events generated by the ^{252}Cf source along the calibration pipe. The energy is flat whenever the reconstructed position is more than 30 cm from PMTs

7.2 Reconstruction problems

We have just seen that event reconstruction gives good results, for calibration runs, as long as the source position is inside Region I. Unfortunately this is not always true and more and more problems arise for events closer and closer to the geode surface.

The main problem concerns the $1/r^2$ divergence of the light collected by one PMT; the exponential light attenuation, entering formulae (19,22), becomes inaccurate in the vicinity of the PMTs. In such a case, the approximation of a flat PMT surface is also no longer adequate to evaluate the solid angle by means of (23). These effects are shown in Fig. 31. The neutron capture energy (both for Gadolinium and Hydrogen) is overestimated at reconstructed distances smaller than $\sim 30\,\mathrm{cm}$ from the geode surface.

Figure 31 also shows one further weakness inherent in the minimization procedure. As remarked above, the MIGRAD minimizer heavily depends on the knowledge of the first derivatives of (25) with respect to the fit parameters and fails if this computation is not accurate enough. This situation arises for events near the acrylic vessel, where the first derivatives of (25) exhibit a discontinuity due to the different light attenuation of the Region I and Region II scintillators; as a result, a discontinuity in the energy vs. distance profile is found around the vessel surface position. A slight improvement was obtained by calling the CERN SIMPLEX routine when MIGRAD failed. This minimizer, although much slower and in general less reliable than MI-

GRAD, is more suitable in this case since it does not use first derivatives and it is not so sensitive to large fluctuations in the function value.

Figure 32 shows the distribution of ^{252}Cf neutron events generated at $z = -120$ cm. The discontinuity in the z distribution is also present for Monte Carlo generated events, thus proving that this is an inherent feature of the minimization procedure, and was properly taken into account in evaluating the neutrino detection efficiency.

8 Neutrino event selection and background rejection

Neutrino events must be identified in a diverse and much more numerous background. Off-line selections, based on the reconstructed event variables, were chosen to enhance the signal/background ratio; at full reactor power this ratio is > 20. We performed a careful evaluation of the efficiencies associated with the selection criteria. The analysis procedure is reviewed and the characteristics of the neutrino event sample are presented.

8.1 The data sample

The data acquisition period extended over 450 days, from 12 March 1997 till 20 July 1998; about 2000 runs were taken, including standard neutrino runs (about 1/4 of the total) and daily calibrations. The experiment stopped taking data five months after the last reactor shut-down (8 February 1998) when it became clear that, due to problems related with the cooling system, neither reactor would resume its normal operating conditions for at least one year.

Data taking is summarized in Table 1; the total thermal energy released (which can be intended as a neutrino integrated luminosity) is also listed. The total live time amounts to ≈ 340 d, 40% of which was with both reactors off. The power evolution of the CHOOZ reactors is illustrated in Fig. 33. The set of power values for both reactors almost continuously covers the entire range up to full power. It is worth noting that this is a very unique feature of the CHOOZ experiment.

Only one of the two CHOOZ reactors was on for at least 80% of the total live time of the experiment. This allowed us to extract the separate contribution of each reactor to the neutrino signal and to perform, thanks to their different distances from the detector, a two-distance oscillation test.

8.2 Candidate event selection

Radioactivity background events are greatly reduced by applying loose energy cuts to the neutron–like signals; events are selected if $\mathrm{QSUM_n} > 13000$ ADC counts, which roughly corresponds to a 4 MeV energy deposit at the detector centre. The residual events ($\approx 7.2 \cdot 10^5$ over a total

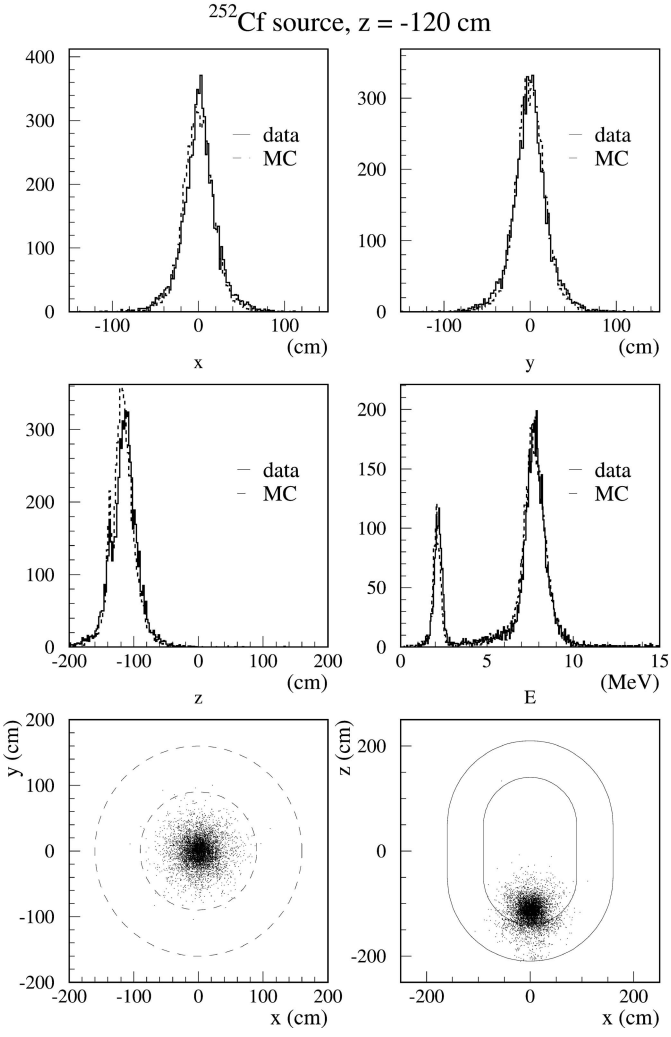

Fig. 32. Distributions of neutron events with the ^{252}Cf source at z = -120 cm. The discontinuity in the z distribution at the vessel surface is visible also in Monte Carlo generated events

number of $\approx 1.2 \cdot 10^7$ L2 triggers) are then reconstructed by the standard minimization procedure described above.

An analysis of this preliminary sample gives a first illustration of the properties of the neutrino signal (reactor–on data) and the associated background (reactor–off data). Figures 34, 35 show the correlation of neutron–like vs. positron–like energy for this sample. Neutrino events, as indicated in Fig. 34, populate a region in the (E_{e^+}, E_n) plot delimited by $E_{e^+} < 8$ MeV and $6 < E_n < 12$ MeV. Background events, depending on their position in these scatter plots, are classified in the following categories:

A) events with $E_{e^+} < 8$ MeV and $E_n > 12$ MeV:
B) events with $E_{e^+} > 8$ MeV and $E_n > 12$ MeV:
C) events with $E_{e^+} > 8$ MeV and $6 < E_n < 12$ MeV:
D) events with $E_{e^+} < 8$ MeV and $E_n < 6$ MeV:

The neutron energy distribution of C) events presents a clear 8 MeV peak, typical of the neutron capture on Gadolinium, still persisting in the reactor-off data. These events can then be interpreted as a correlated background

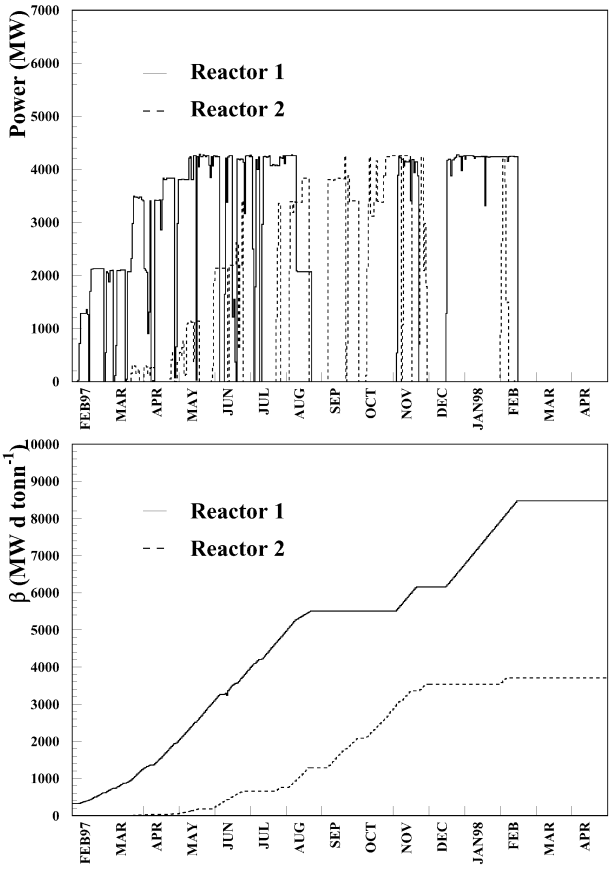

Fig. 33. Power (*top*) and burn-up (*bottom*) evolution for CHOOZ reactors. Both have been off since February 1998

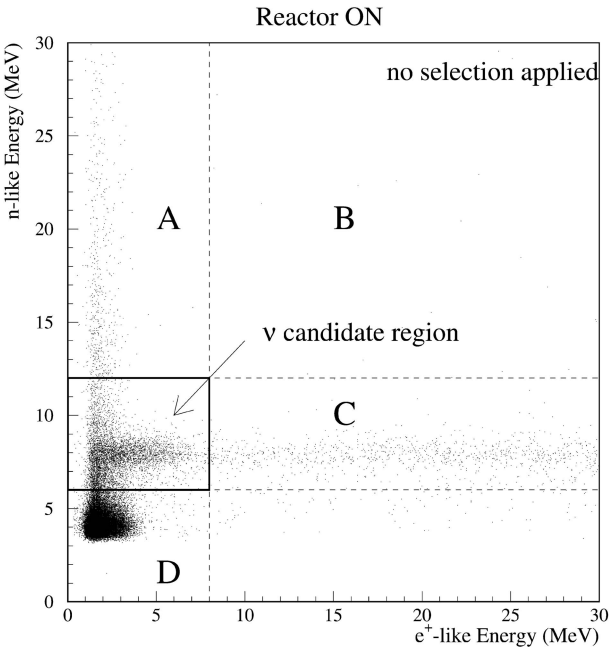

Fig. 34. Neutron versus positron energy for neutrino-like events collected during the reactor-on period. A preliminary cut to the neutron QSUM is applied to reject most of the radioactivity background

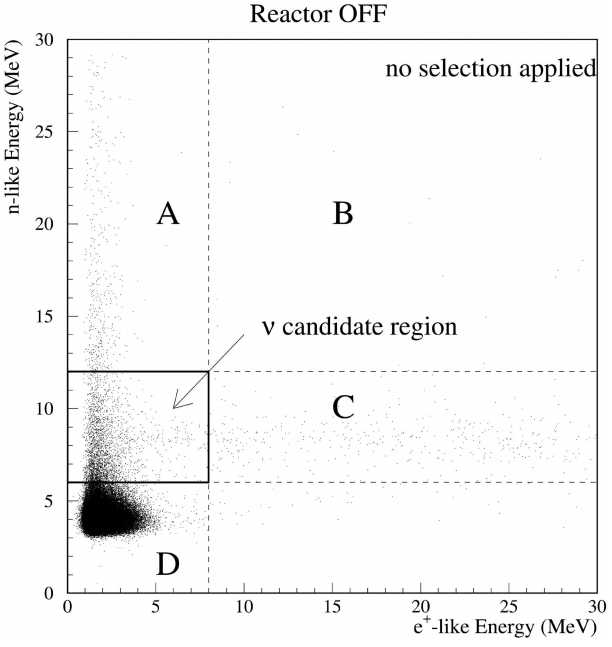

Fig. 35. Same as before, with neutrino-like events collected during the shut-down of both reactors

associated with high energy spallation neutrons from cosmic ray interactions in the rock surrounding the detector; the neutrons entering the detector are slowed down to thermal velocities via elastic scattering on protons and then captured; the proton recoil signal, whose energy spectrum is basically flat and extends to high energies, mimics the positron signal. This interpretation is confirmed by the neutron delay distribution. An example is shown in Fig. 36, where events in sample C) follow an exponential decay distribution whose life time $\tau = (30.5 \pm 1.0)\,\mu$s is correct for neutron capture in the Gd-doped scintillator.

Events in categories A) and D) show a flat delay distribution, therefore implying an accidental coincidence of uncorrelated signals. In both cases, the positron signal is faked by a low energy ($E_\gamma \leq 3\,$MeV) radioactivity event. The neutron signal may be associated with either another radioactivity event, as in category D), or a high activity signal (most likely due to a proton recoil) as in category A).

Finally, the delay of B) events is exponentially distributed with a lifetime $\tau = (2.8 \pm 0.4)\,\mu$s which is compatible with that of a muon decay at rest. These events can be associated with residual cosmic muons stopping in the detector and then decaying. Both the muon energy loss and the Michel electron energy are much higher than the typical energy of a reactor neutrino interaction; these events can be rejected by applying an energy selection both to the positron–like and the neutron–like signals.

The accidental background can be significantly reduced by applying fiducial volume cuts. Less than 10% of the events in regions A) and D), as shown in Fig. 37, survive the selection cuts (distances from the geode $d > 30\,$cm for both positron and neutron and relative distance $<$

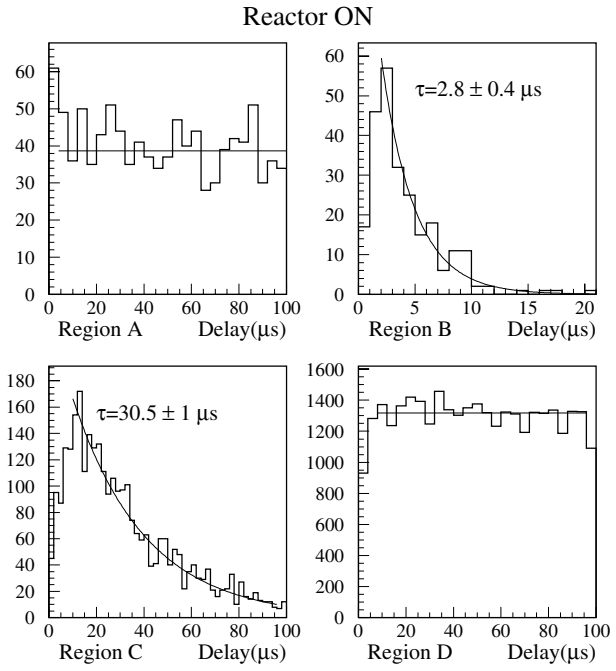

Fig. 36. Distribution of positron–neutron delay for the different event categories. The best fit curves are also drawn and the relative parameters indicated

100 cm). Conversely the correlated background is more difficult to eliminate since these events exhibit the same features as neutrino interactions. This is the reason why the final background rate is dominated by the correlated component, in spite of the shielding provided by the rock overburden. However, the neutron signals associated with this background component are an important tool to follow the energy calibration stability throughout the experiment. The results are shown in Fig. 38, where the average neutron energy, obtained by a Gaussian fit of the Gadolinium capture peak, is plotted vs. the run number. The relative stability throughout the data taking period (drift at a 0.8% level) is an independent verification of the reliability of the adopted reconstruction technique.

8.3 Final selection

Both the energy and the topological cuts were studied and optimized by relying on the Monte Carlo simulation of neutrino events. These predictions were cross-checked with the calibration data to gain confidence in the final efficiencies. We adopted the following criteria for selecting neutrino events:

1) Positron energy: $E_{e^+} < 8\,\mathrm{MeV}$:
2) Neutron energy: $6 < E_n < 12\,\mathrm{MeV}$:
3) Distance from geode boundary:
   $d_{e^+} > 30\,\mathrm{cm}$, $d_n > 30\,\mathrm{cm}$:
4) Relative positron–neutron distance: $d_{e^+n} < 100\,\mathrm{cm}$:
5) Neutron delay: $2 < \Delta t_{e^+n} < 100\,\mu\mathrm{s}$:
6) Neutron multiplicity: $N_n = 1$.

The cut on the positron–like energy is chosen to accept all possible positron triggers. The L1lo trigger threshold limits the lower end while the upper limit was set to 8 MeV since the probability of having a larger positron energy is negligible ($< 0.05\%$).

Cut 2) selects the neutrino events associated with the neutron captures on Gadolinium, which are more than 80% of the total. The lower cut introduces an additional inefficiency due to γ rays escaping the containment region. As illustrated in Fig. 37, 6 MeV is a suitable choice to separate neutrino events from the residual low energy uncorrelated background, thus optimizing the signal to noise ratio.

The cut on the neutron delay covers about three capture times for neutrons in Region I. The 2 μs lower cut was introduced to reduce the effects of the signal overshoot inherent the AC coupling of PMT bases and front-end electronics. These effects are particularly troublesome in the case of NNADC's, which integrate current signals of both polarities.

The correlated background can be reduced by applying a cut on the secondary particle multiplicity[2]. Muon spallation processes usually generate several neutrons, therefore more than one particle is likely to enter the detector and give a detectable signal.

Events satisfying the selection criteria will be referred to as *neutrino event candidates* from now on. The next section reviews the efficiency for selecting neutrino interactions and the background rejection resulting from individual cuts.

8.4 Positron efficiency

Energy cut

The expected positron energy spectrum is obtained by folding the kinetic energy spectrum coming from (9) with the detector response function. Two problems then arise in evaluating the positron efficiency. Firstly, the neutrino spectral shape slightly varies along a reactor cycle as a consequence of the fuel burn-up; however, the information daily provided by E.D.F. allows us to accurately follow this variation. Secondly, the energy cut operated by the L1lo trigger increases with time because of the aging of Region I scintillator. A daily check of the equivalent energy threshold is required to account for this effect. The procedure we followed is shown in Fig. 39. A Lecroy qVt recorded the energy spectra due to a ^{60}Co source placed at the detector centre. Two spectra were taken, the first one with an external trigger provided by the L1lo signal and the second with an internal trigger set at a lower threshold. In addition to the 2.5 MeV "sum" line, each spectrum exhibits a low energy tail due to the energy loss in the calibration pipe. The ratio of the two spectra (after background subtraction) yields the L1lo trigger efficiency curve. The equivalent energy threshold results from fitting this curve by an integral Gaussian function.

[2] The positron (or primary) signal is associated with the L1 trigger preceding the L2. Every signal associated with or occurring after the L2 is referred to as a secondary event

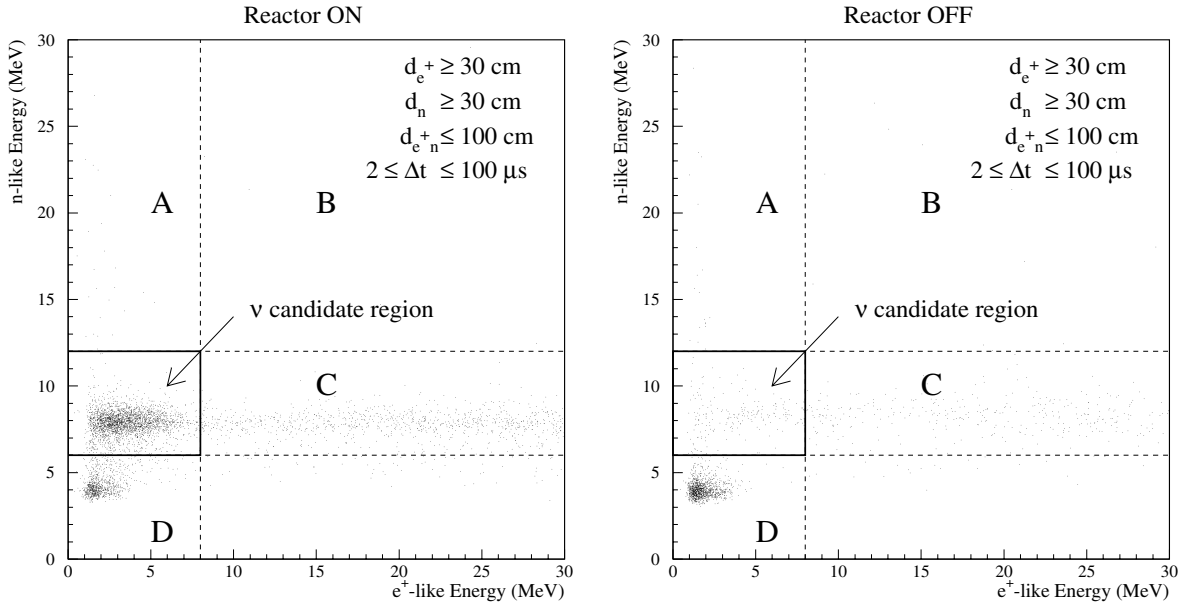

Fig. 37. Neutron versus positron energy for neutrino-like events selected from the preliminary sample by applying the "topological" cuts here indicated

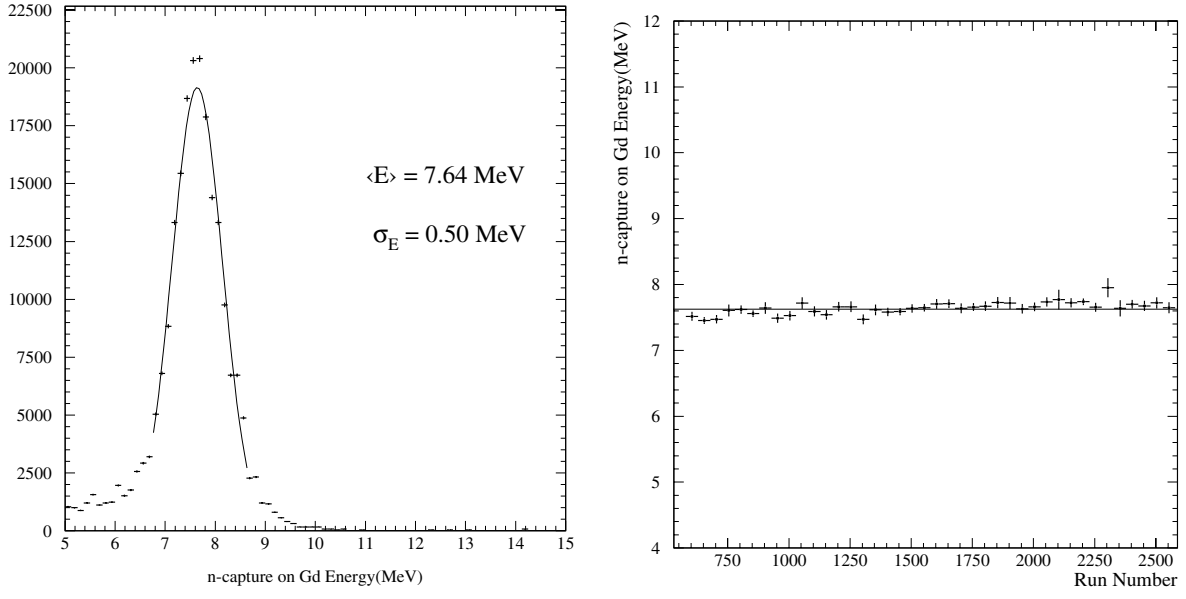

Fig. 38. Neutron energy distribution for correlated background events (*left*) and average $E_{\rm n}$ vs. run number (*right*)

The energy threshold varies with time as illustrated in Fig. 40. Its behaviour can be described by a linear function. Discontinuities arise in coincidence with the threshold resettings, which were needed to bring the L1lo threshold back to the optimal value.

More extensive ^{60}Co calibrations were periodically performed at different positions of the source along the central pipe, in order to measure the z dependence of the energy threshold. The results are shown in Fig. 41 at four different stages of data acquisition. The overall dependence on the position of the energy threshold can also be predicted by a Monte Carlo simulation of the QSUM and NSUM behaviour. The attenuation length values are the same as those used in the event reconstruction. The threshold measurement always fits well with expectations, as evident from the same figure. We can therefore rely on Monte Carlo predictions to determine the energy threshold at each position in the detector, where the source cannot be placed. An expression for the positron threshold as a function of time and position can be derived by combining the daily threshold measurements at the detector centre with Monte Carlo evaluations. An explicit form of this threshold is given in cylindrical coordinates (ρ, z, ϕ) by the following equation:

$$E_{thr}(t, \overrightarrow{\mathrm{x}}) = E_{thr}(t, \overrightarrow{\mathrm{x}} = 0) \times (1 - \alpha(t)\rho^2) \times (1 - \beta(t)z^2) \quad (27)$$

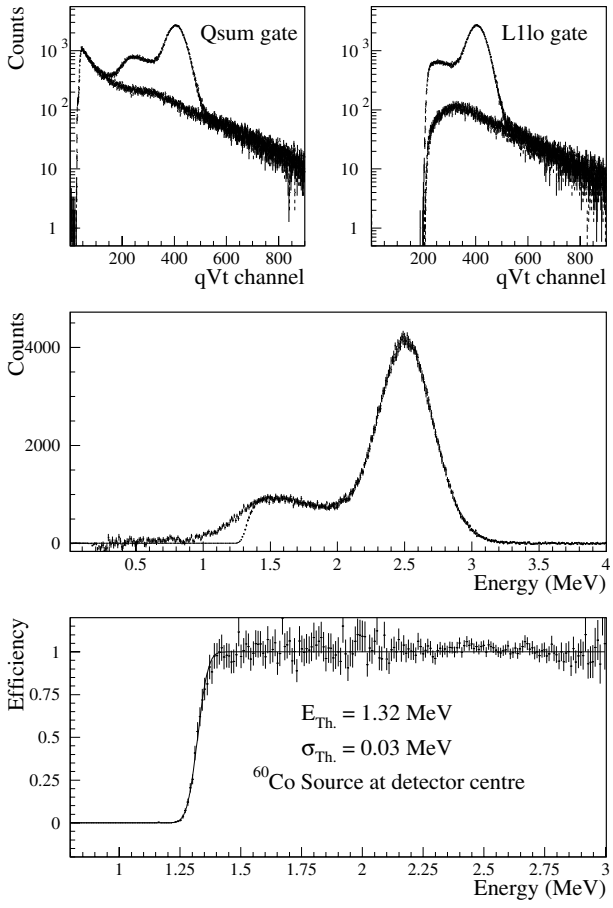

Fig. 39. Determination of the L1lo equivalent energy threshold. The top figures show the QSUM spectra measured with a ^{60}Co at the detector centre by means of an internal and external triggered qVt (the corresponding background is superimposed). The central plot shows the background subtracted spectra. The bottom histogram, displaying the efficiency curve, follows an integral Gaussian function whose parameters are indicated

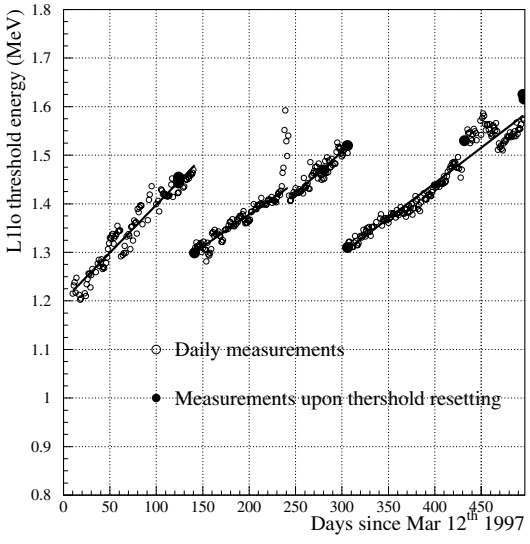

Fig. 40. Equivalent energy threshold at detector centre as a function of time. The jumps visible here are due to the threshold setting

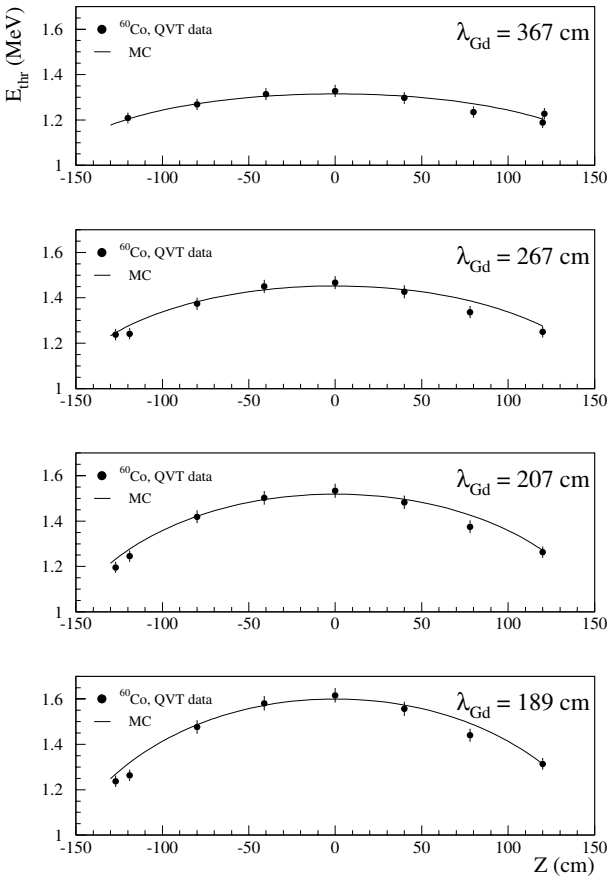

Fig. 41. Energy threshold as a function of z for different values of the attenuation length for the Gd-doped scintillator. The measurements obtained with the ^{60}Co source follow the expected behaviour

where the energy threshold at centre $E_{thr}(t, \overrightarrow{\mathrm{x}} = 0)$ is extracted by interpolating the daily measurements shown in Fig. 40 and $\alpha(t), \beta(t)$ are linear functions obtained by Monte Carlo.

Distance from the geode cut

The positron loss due to the selection 3) (distance from the geode boundary) was evaluated by a Monte Carlo simulation of neutrino interactions. 10000 events were uniformly generated in a volume including a 10 cm wide shell surrounding the target, so as to take into account spill-in/spill-out effects. The estimated efficiency proves to be almost independent of the scintillator degradation; we can then consider it as a constant and get the average value

$$\varepsilon_{d_{e^+}} = (99.86 \pm 0.1)\% \qquad (28)$$

8.5 Neutron efficiency

Neutron capture cut

The neutron capture efficiency is defined as the ratio of neutrons captured by Gadolinium nuclei to the total num-

ber of captures. This ratio enters the global neutron efficiency since the neutron energy selection excludes events associated with neutron captures on Hydrogen. This capture efficiency was studied by means of a normal and a special tagged ^{252}Cf source, providing a fission tagging signal. The calibration pipe was removed for these particular studies in order to avoid effects due to the iron content in the pipe. The source was at the end of a plumb-line long enough to reach the bottom of the target vessel. Fission neutrons have a longer mean pathlength than neutrons from neutrino interactions (≈ 20 cm in scintillator instead of ≈ 6 cm), so calibration data must be coupled with Monte Carlo predictions to correctly take into account the effects associated with the neutron spill-out (which are relevant for events approaching the boundary of Region I).

Neutron events are associated with Gd captures if $4 < E_{\rm n} < 12$ MeV. The ratio obtained includes a 1% correction due to Gd-capture events with visible energy below 4 MeV. The combination of data and MC studies results in an average efficiency over the entire detector of

$$\varepsilon_{Gd} = (84.6 \pm 0.85)\% \tag{29}$$

Energy containment cut

The 6 MeV lower energy cut introduces an inefficiency in neutron detection due to the γ rays from Gd-capture (by definition inside Region I) escaping the visible volume. Since this efficiency is almost independent of the neutron pathlength we can rely on the calibration data to evaluate this number; Monte Carlo predictions are used to cross-check the data. Since this effect is expected to be more relevant for events near the edge of Region I, a fine source scanning was made in this region. A special set of runs, was made with 2 cm steps, between 1.5 cm and 11.5 cm, from the bottom edge of the acrylic vessel.

The escape fraction was defined as the ratio of the number of events with $4 < E_{\rm n} < 6$ MeV over those with $4 < E_{\rm n} < 12$ MeV. The values turn out to range from 2.9% at the centre to up to 6.6% at the bottom edge. By averaging over the target volume we get

$$\varepsilon_{E_{\rm n}} = (94.6 \pm 0.4)\% \tag{30}$$

Distance from the geode cut

We followed the same procedure used to evaluate the corresponding positron efficiency. We obtain

$$\varepsilon_{d_{\rm n}} = (99.5 \pm 0.1)\% \tag{31}$$

This value is not significantly affected by the scintillator degradation.

Delay cut

The neutron delay cut was studied by using both the ^{252}Cf and an Am/Be source; the latter emits single neutrons only, preventing biases due to the ADC integration dead time arising at high neutron multiplicities. Figure 42 shows the delay distributions obtained with the Am/Be source placed at the centre and at the bottom edge of the target. The neutron capture time at the centre can be used to determine the Gd content in the Region I scintillator (to be used in the Monte Carlo code). The fitted decay time $\tau = (30.7 \pm 0.5)\,\mu$s corresponds to a mass fraction of $(0.0940 \pm 0.0015)\%$. With reference to Fig. 42(right), at the bottom of the detector the neutron capture on Hydrogen becomes more important and the fitted decay time increases accordingly. Both spectra show a low first bin content. This is due to neutron moderation time which corresponds to the relatively fast neutrons emitted by the Am/Be source.

Given the chemical composition of the scintillator, it is possible to rely on the Monte Carlo simulation to predict the efficiency related to the neutron delay cut in the case of neutrino induced events. The estimated loss due to the $2\,\mu$s analysis cut amounts to $1.6 \pm 0.2\%$; the fraction of neutrons with $\Delta t > 100\,\mu$s is $4.7 \pm 0.3\%$. We therefore end up with:

$$\varepsilon_{\Delta t} = (93.7 \pm 0.4)\% \tag{32}$$

8.6 Relative distance cut efficiency

Again we used the reconstruction of 10000 Monte Carlo generated events to predict the efficiency due to the positron–neutron distance cut. We obtained

$$\varepsilon_{d_{\rm e^+n}} = (98.4 \pm 0.3)\% \tag{33}$$

Again this efficiency is nearly independent of the time evolution of the Gd-doped scintillator.

8.7 Neutron multiplicity

The neutron multiplicity cut rejects neutrino events if a "spurious" L1lo trigger occurs along with the positron–neutron pair. L1lo triggers are mainly associated with γ-background events, $\approx 97\%$ of which have energies lower than the high threshold; so, the background above the L1hi threshold can be neglected in what follows. The error associated with this approximation is negligible.

Let us consider all possible sequences:

1) $\mathrm{e}^+ - \mathrm{n} - \gamma$ with $t_\gamma - t_{\rm n} < 100\,\mu$s:
2) $\mathrm{e}^+ - \gamma - \mathrm{n}$:
3) $\gamma - \mathrm{e}^+ - \mathrm{n}$ with $t_{\rm e^+} - t_\gamma < 100\,\mu$s:

Case 1

The L2 triggers on the $(\mathrm{e}^+, \mathrm{n})$ pair and the γ signal is mistaken for a second neutron; the neutrino event is then rejected because of cut 6). Given the γ rate R_γ, the probability of such a sequence is

$$1 - \varepsilon_1 = R_\gamma \Delta t_\nu \tag{34}$$

(where Δt_ν is the $98\,\mu$s acceptance window) from which ε_1 is extracted. The average efficiency is $(98.6 \pm 0.3)\%$.

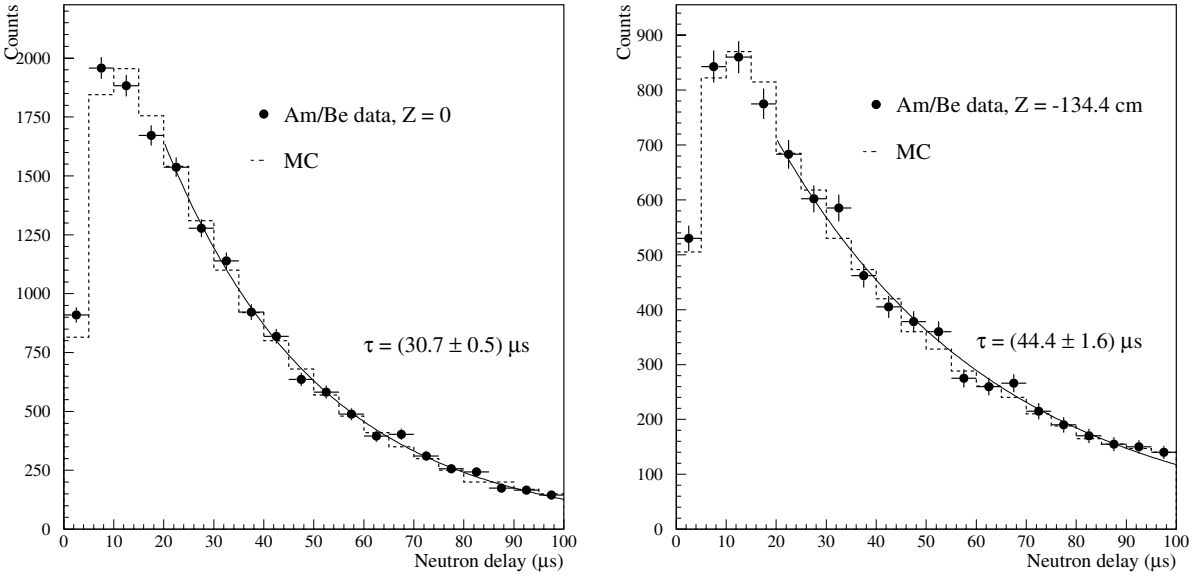

Fig. 42. Neutron delay distribution measured with the Am/Be source at the detector centre (*left*) and at the bottom edge of the acrylic vessel (*right*). The time origin is defined by the 4.4 MeV γ-ray. No time analysis cut is applied yet

Case 2

If the positron energy exceeds the high threshold, the L2 triggers on the (e^+, γ) pair; then two neutron–like signals are detected (the "true" neutron plus the γ) and the neutrino event is rejected by cut 6). If the positron energy is lower then the L1hi threshold, the L2 triggers on the (γ, n) and the γ is mistaken for a positron–like event. Since the γ signal is not correlated with the neutron, the probability of surviving the topological cuts 3) and 4) is quite low ($< 2\%$) and can be neglected. As a conclusion, neutrino events occurring in such a sequence are always rejected, whatever the positron energy is.

Let $P_n(t_c)$ be the neutron delay distribution shown in Fig. 42 and t the time between the positron and the γ signals. The neutrino efficiency can be written as follows:

$$\varepsilon_2 = 1 - \int_0^{100} P_n(t_c)\,dt_c \int_0^{t_c} R_\gamma\,dt = 1 - R_\gamma \overline{t_c} \qquad (35)$$

where $\overline{t_c} = (30.5 \pm 0.5)\,\mu$s is the average neutron delay.

Case 3

Like the above case, if the positron signal met the high trigger condition, L2 would trigger on the (γ, e^+) pair and the selection criterium 6) would reject the event; otherwise the L2 would trigger on the (e^+, n) pair and the neutrino events would be accepted. So

$$\varepsilon_3 = 1 - R_\gamma f_H \Delta t_\nu \qquad (36)$$

$f_H = (0.45 \pm 0.05)$ being the positron fraction above the high energy threshold.

Combined efficiency

The neutron multiplicity cut efficiency is obtained by multiplying the three above efficiencies. We evaluated it on a run by run basis since R_γ depends on the L1lo threshold. The average value is $\varepsilon_{2n} = (97.4 \pm 0.5)\%$.

A summary of all the efficiencies is presented in Table 6.

Table 6. Summary of the neutrino detection efficiencies

selection	ϵ(%)	rel. error (%)
positron energy*	97.8	0.8
positron-geode distance	99.9	0.1
neutron capture	84.6	1.0
capture energy containment	94.6	0.4
neutron-geode distance	99.5	0.1
neutron delay	93.7	0.4
positron-neutron distance	98.4	0.3
neutron multiplicity*	97.4	0.5
combined*	69.8	1.5

*average values

9 The neutrino signal

Figures 43 through 45 present the final neutrino candidate sample, with all the selection cuts applied. A total number of 2991 neutrino candidates was collected, 287 of which occurred during the reactor-off periods. To properly compare these with expectations, the entire acquisition cycle was divided according to the dates of the threshold resetting, when variations in the background rate were expected. For each resulting period, the reactor-off background was normalized to the same livetime as the reactor-on spectra.

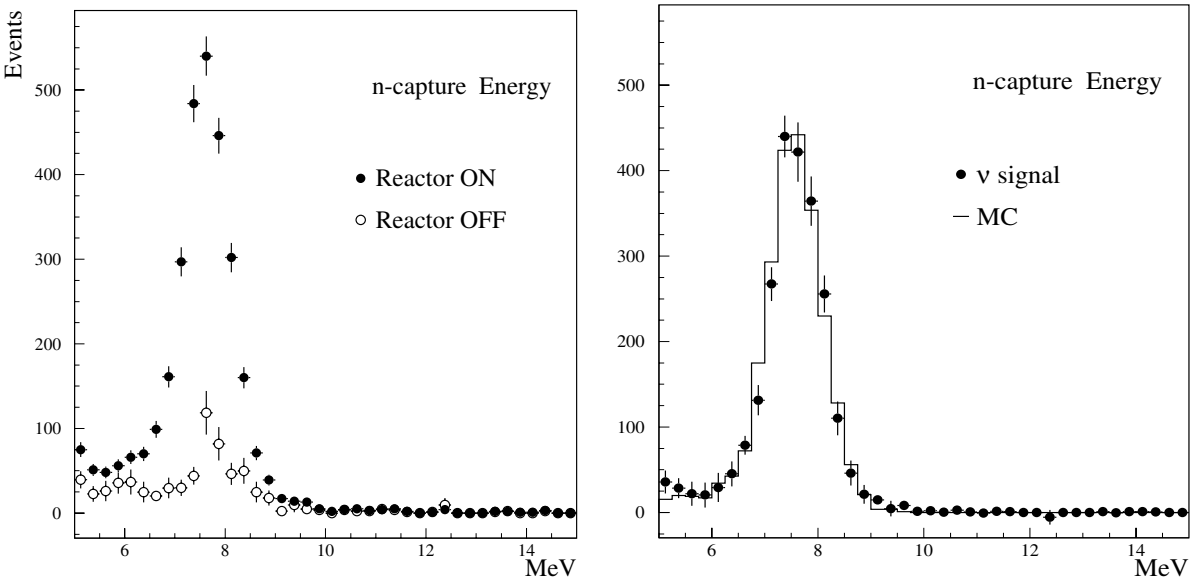

Fig. 43. Neutron energy spectra for reactor-on and reactor-off periods (*left*) and background subtracted spectrum compared to Monte Carlo expectations (*right*)

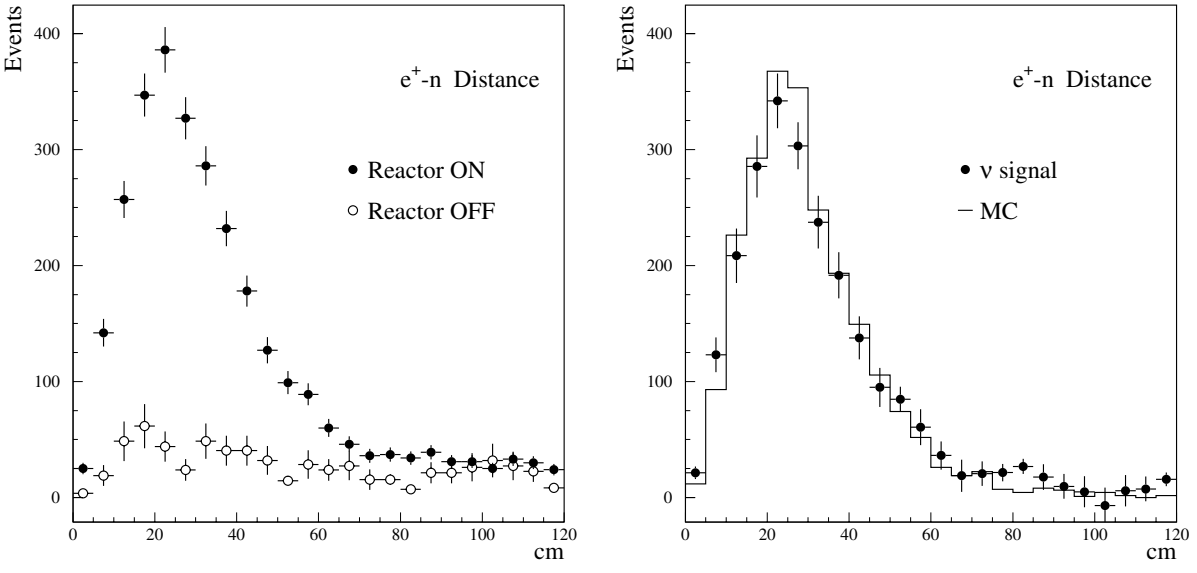

Fig. 44. Same as before, for the positron–neutron distance

9.1 Measured positron spectrum

Fig. 46 shows the complete measured spectra (reactor-on, reactor-off), obtained by summing the spectra collected during runs relative to different off-line periods; the resulting positron spectrum (reactor-on minus reactor-off) is presented in Fig. 47. The chosen bin width (0.4 MeV) is roughly adapted both to the statistics and to the energy resolution.

9.2 Predicted positron spectrum

The expected visible energy positron spectrum at the detector position, for a mean reactor-detector distance L_k, is given by:

$$S_k(E, L_k, \theta, \delta m^2) = \frac{1}{4\pi L_k^2} N_p \int h(L, L_k)\, \mathrm{d}L \times \int \sigma(E_{\mathrm{e}^+}) S_\nu(E_\nu) P(E_\nu, L, \theta, \delta m^2) \times r(E_{\mathrm{e}^+}, E) \varepsilon(E_{\mathrm{e}^+})\, \mathrm{d}E_{\mathrm{e}^+}, \quad (37)$$

where

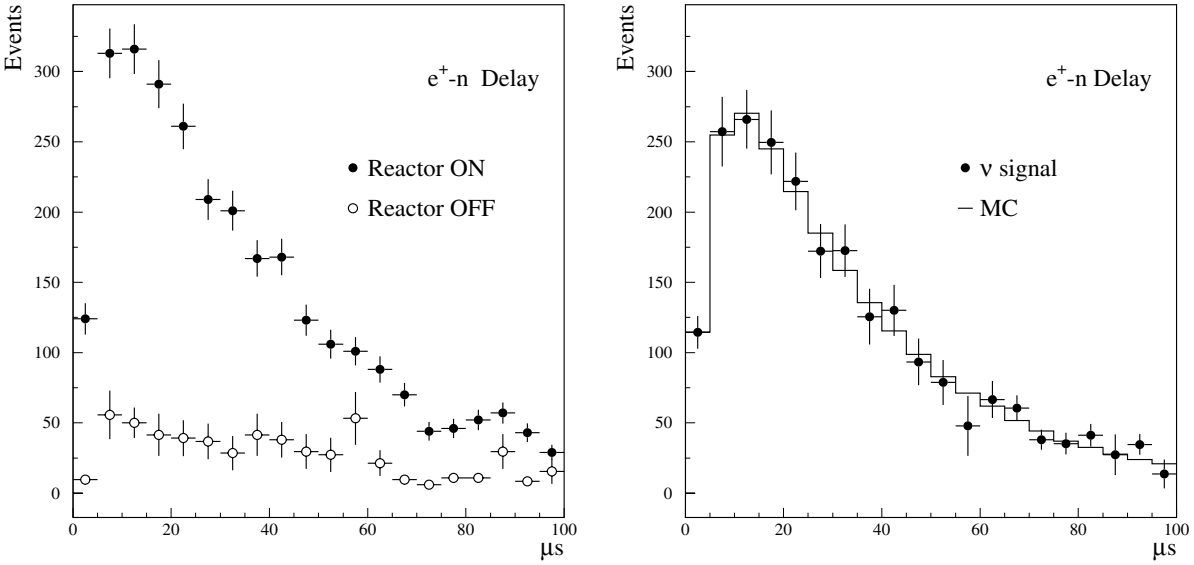

Fig. 45. Neutron delay distributions for reactor-on and reactor-off periods (*left*) and background subtracted spectrum compared to MC predictions (*right*)

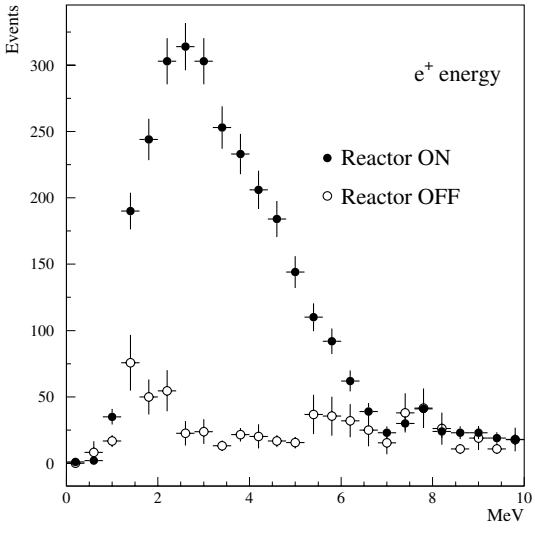

Fig. 46. Experimental positron spectra for reactor-on and reactor- periods after application of all selection criteria. The errors shown are statistical

E_ν, E_{e^+}	are related by (9),
N_p	is the total number of target protons in the Region I scintillator,
$\sigma(E_{e^+})$	is the detection cross section (10),
$S_\nu(E_\nu)$	is the $\overline{\nu}_e$ spectrum,
$h(L, L_k)$	is the spatial distribution function for the finite core and detector sizes,
$r(E_{e^+}, E)$	is the detector response function providing the visible e^+ energy,
$P(E_\nu, L, \theta, \delta m^2)$	is the two-flavour survival probability,
$\varepsilon(E_{e^+})$	is the combined detection efficiency.

We first computed the positron spectrum in the absence of neutrino oscillations, by using the Monte Carlo code to simulate both reactors and the detector. The composite antineutrino spectrum was generated for each of the 205 fuel elements of each reactor core; each antineutrino was assigned a weight according to the prescriptions given in Sect. 2.9. The interaction points were randomly chosen in the target; the positron and resulting annihilation photons were tracked in the detector, and scintillator saturation effects were included to correctly evaluate the positron visible energy. The resulting spectrum, summed over the two reactors, is superimposed on the one measured in Fig. 47 to emphasize the fact that the data fit with the no-oscillation hypothesis; the Kolmogorov-Smirnov test for compatibility of the two distributions gives a 82% probability. The measured vs. expected ratio, averaged over the energy spectrum (also presented in Fig. 47) is

$$R = 1.01 \pm 2.8\%(\text{stat}) \pm 2.7\%(\text{syst}) \qquad (38)$$

In the next section we will discuss how this ratio constrains the oscillation hypothesis.

9.3 Background

One of the main features of the experiment, the low background, represents a difficulty in that it is hard to measure. Apart from the low statistics, another difficulty is that the background rate depends on the trigger conditions which, as discussed above, changed with time due to scintillator aging and the positron threshold adjustments. Separate estimates of the background are then needed for each data taking period. Only 34 events were collected during the 1997 runs (periods 1 & 2, until 12 January 1998, date of the last threshold resetting: see Table 7 below) with reactors off, the total live time being 577 h; this implies a background rate of 1.41 ± 0.24 events per day. Most of the

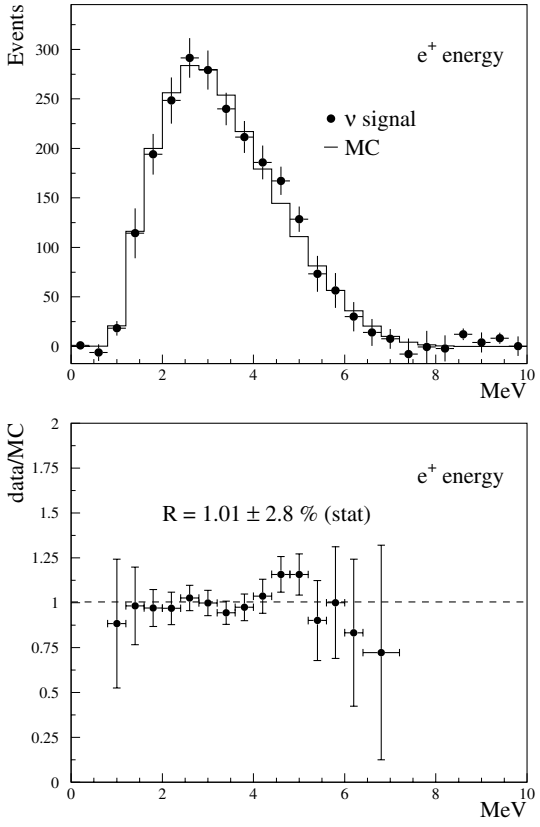

Fig. 47. (*above*) Expected positron spectrum for the case of no oscillations, superimposed on the measured positron obtained from the subtraction of reactor-on and reactor-off spectra; (*below*) measured over expected ratio. The errors shown are statistical

reactor-off statistics, amounting to 253 events, was collected during the 1998 run when the cumulative reactor power was very low; the reactor-off live time is 2737 h. The resulting background rate is 2.22 ± 0.14, about twice as large as in the 1997 run.

The explanation for this variation relies on the lowering of the NSUM threshold associated with the L1lo trigger. A lower number of hit PMTs implies a larger fiducial volume extended towards the PMT boundary, where the event rate is dominated by the natural radioactivity. Moreover, we saw that the reconstruction algorithm overestimates the energy of events near the PMTs (see Fig. 31). Therefore a larger fraction of radioactivity events is shifted into the neutrino candidate event window shown in Figs. 34, 35, 37. As a result, the accidental component of the background is greatly enhanced. On the other hand, the correlated background is virtually unaffected by the low trigger conditions, since the neutron signal is much higher than the threshold. We verified that the correlated background did not significantly change throughout the experiment.

As a further cross-check of the reactor-off estimates, we measured the background by extrapolating to zero the candidate yield versus reactor power. This will be the subject of Sect. 9.6.

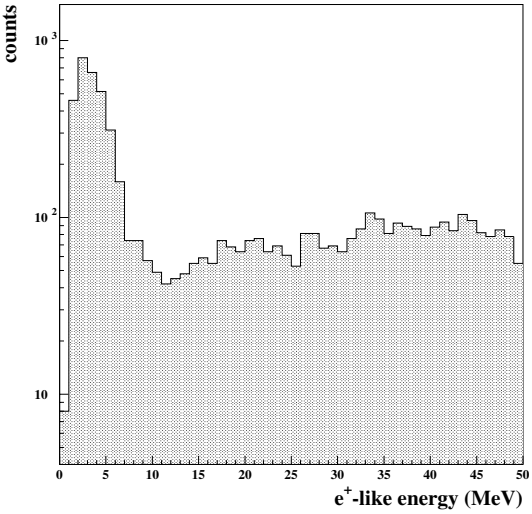

Fig. 48. Energy distribution of e^+-like signals associated with the correlated background

9.4 Correlated background

Figure 48 shows the energy distribution of e^+-like signals associated with the correlated background; these events are selected by applying all the criteria for neutrino candidate selection, except e^+-like energy. Apart from a low-energy peak (due to the neutrino events and to the accidental background), the spectrum has a roughly flat distribution extending beyond 30 MeV, with a slight increase at higher energies caused by the NNADC saturation. A Monte Carlo simulation of this spectrum is very difficult, since no reliable transport code is available for spallation neutrons in the $10 \div 100$ MeV kinetic energy range. Moreover, the observed spectrum is affected by the scintillator saturation (which is relevant at low recoil proton energies).

To verify the stability of the correlated background rate, we divided the complete run into three different periods (see Table 7 below) corresponding to the dates of the threshold resetting. The spectra for each period were fitted in the $10 < E < 30$ MeV range. We divided them by the live times (also listed in Table 7) of the three periods, and finally found:

$$B_{corr} = \begin{cases} (0.156 \pm 0.01)\,\mathrm{MeV}^{-1}\,\mathrm{d}^{-1} & \text{for the 1st period,} \\ (0.158 \pm 0.01)\,\mathrm{MeV}^{-1}\,\mathrm{d}^{-1} & \text{for the 2nd period,} \\ (0.151 \pm 0.01)\,\mathrm{MeV}^{-1}\,\mathrm{d}^{-1} & \text{for the 3rd period,} \end{cases} \quad (39)$$

confirming the stability of the correlated background rate throughout the experiment.

A rough evaluation of the correlated background can be obtained by extrapolating the rate in the positron window ($E_{thr} < E < 8$ MeV). Taking the average value from (39) and assuming $E_{thr} = 1.5$ MeV, we obtained a rate of $(1.01 \pm 0.04(stat) \pm 0.1(syst))$events d^{-1}.

9.5 Accidental background

The accidental background rate was determined by separate estimates of the singles rate for both e^+-like and n-like signals. To minimize possible biases due to the trigger, both estimates were performed by looking at "isolated old" events, i.e. at the hits recorded in the NNADC event buffer (storing up to 9 events) for which the previous and following events were more than 1 ms distant (isolated) and which occurred at least 2 ms before the L2 trigger (old). The event selection was operated by applying the same cuts (energy and distance from edge) used for the candidate selection; in the 1997 run we found $R_{e^+} = (64.8 \pm 0.1)\,s^{-1}$ for the e^+-like event rate and $R_n = (45 \pm 2)\,h^{-1}$ for the n-like one. The rate of accidental coincidences $e^+ - n$ in the $2 \div 100\,\mu s$ time window therefore turns out to be $(3.4 \pm 0.15)\,d^{-1}$. An additional reduction factor $f_d = (0.12 \pm 0.01)$ was applied to account for the selection operated by the $e^+ - n$ distance cut. The resulting background rate is $(0.42 \pm 0.05)\,d^{-1}$, which fits with the previous determinations of the total and the correlated background for the 1997 run.

We checked that the measured single event rates R_{e^+} and R_n are in agreement with estimates based on the radioactive contaminants present in the detector and its surroundings [59,60].

9.6 Neutrino yield versus power

The CHOOZ experiment gave us the unique opportunity of measuring the neutrino flux before either reactor started working and also after the reactors were shut down. We were therefore able to collect enough reactor–off data to determine the background rate and could further measure the neutrino flux while the reactors were ramping up to full power. By fitting the slope of the measured rate versus reactor power it is possible to determine the neutrino rate at full power, which can then be compared with the predicted neutrino production rate at full power. This procedure provides not only a very powerful tool to determine the neutrino deficit and test the oscillation hypothesis, but also gives an independent estimate of the background rate to be compared with the values quoted above.

The fitting procedure is as follows. For each run i the predicted number of neutrino candidates $\overline{N}_i$ is derived from the sum of a signal term, linearly dependent on reactor power W_{1i} and W_{2i}, with the background B, assumed to be constant and independent of power:

$$\overline{N}_i = (B + W_{1i}Y_{1i} + W_{2i}Y_{2i})\Delta t_i, \tag{40}$$

where Δt_i is live time of run i and (Y_{1i}, Y_{2i}) are the positron yields induced by each reactor. These yields still depend on the reactor index (even in the absence of neutrino oscillations), because of the different distances, and on run number, as a consequence of their different fissile isotope composition. It is thus convenient to factor Y_{ki} into a function X_k (common to both reactors in the no-oscillation case) and distance dependent terms, as follows:

$$Y_{ki} = (1 + \eta_{ki})\frac{L_1^2}{L_k^2}X_k, \tag{41}$$

where $k = 1, 2$ labels the reactors and the η_{ki} corrections contain the dependence of the neutrino counting rate on the fissile isotope composition of the reactor core. We are thus led to define a cumulative "effective" power according to the expression[3]

$$W_i^* \equiv \sum_{k=1}^{2} W_{ki}(1 + \eta_{ki})\frac{L_1^2}{L_k^2}; \tag{42}$$

(40) then becomes

$$\overline{N}_i = (B + W_i^* X)\Delta t_i, \tag{43}$$

X being the positron yield per unit power averaged over the two reactors.

The burn–up corrections η_{ki} must be evaluated on a run by run basis. Since the GEANT routines would have been very time-consuming for such a task, we preferred to follow a simpler approach than the procedure explained at Sect. 9.1. 10000 $\overline{\nu}_e$'s per run were generated at each reactor according to the respective fuel composition; the kinetic positron energy was obtained by the simple relation $E_\nu = T_{e^+} + 1.804\,\text{MeV}$ (which comes from (9) in the limit of infinite nucleon mass). The cross section (10) was thus multiplied by a function $\delta(E_\nu)$ to correct for the shift in the positron energy scale due to the finite neutron recoil effect [40]; this correction can be parametrized as

$$\delta(E_\nu) = 1 - 0.155 \times \exp\left(\frac{E_\nu/\,\text{MeV} - 8}{1.4}\right) \tag{44}$$

We then applied the detector response function (evaluated by Monte Carlo simulations at several positron energies ranging from 0.5 MeV up to 10 MeV) to the positron kinetic energy and weighted each event according to the positron threshold efficiency.

We built the likelihood function $\mathcal{L}$ for a set of n runs as the joint Poissonian probability of detecting N_i neutrino candidates in the i-th run when $\overline{N}_i$ are expected:

$$-\ln \mathcal{L} = -\sum_{i=1}^{n} \ln P(N_i; \overline{N}_i) \tag{45}$$

Searching for the maximum likelihood to determine the parameters X and B is then equivalent to minimizing (45). The minimization procedure is similar to that used in the event reconstruction (see Sect. 7).

Both the average positron yield X and the background rate B are assumed to be constant. This is true, by definition, for the positron yield, since the effect of the threshold

[3] The "effective" power is the thermal power necessary to make the same number of events with a single reactor located at the reactor 1 site. It must provide 9.55 GW at full operating conditions at the start of reactor operation

Table 7. Summary of the likelihood fit parameters for the three data taking periods

period	1	2	3
starting date	97/4/7	97/7/30	98/1/12
runs	579→1074	1082→1775	1778→2567
live time (h)	1831.3	2938.8	3268.4
reactor-off time (h)	38.9	539.5	2737.2
$\int W\,\mathrm{d}t$ (GWh)	7798	10636	2838
B (d^{-1})	1.25 ± 0.6	1.22 ± 0.21	2.2 ± 0.14
X ($\mathrm{d}^{-1}\,\mathrm{GW}^{-1}$)	2.60 ± 0.17	2.60 ± 0.09	2.51 ± 0.17
χ^2/dof	136/117	135/154	168/184
n_ν (d^{-1}) (at full power)	24.8 ± 1.6	24.8 ± 0.9	24.0 ± 1.6

resetting on the positron efficiency is already included in the η_{ki} correction factors. On the other hand, we find that the background rate changes significantly when the trigger threshold are reset. The complete run sample therefore needs to be divided into three periods, according to the dates of the threshold resetting, and the fit parameters for each period drawn separately. The results are listed in Table 7.

By averaging the signal X over the three periods, we obtain

$$\langle X \rangle = (2.58 \pm 0.07)\ \text{counts}\,\mathrm{d}^{-1}\,\mathrm{GW}^{-1}, \qquad (46)$$

corresponding to (24.7 ± 0.7) daily neutrino interactions at full power.

The background rate was stable throughout the 1997 run, then it suddenly increased by close to a factor of 2 in coincidence with the last threshold resetting (see period 3 column). This can be explained in terms of a larger accidental background rate, as a result of threshold lowering.

Figure 49 shows the daily number of neutrino candidates as a function of reactor power for all the data sets together. The superimposed line corresponds to the average fitted signal and background values.

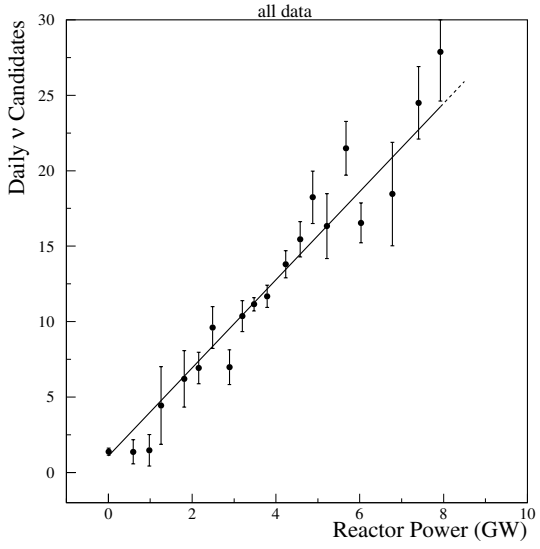

Fig. 49. Daily number of $\overline{\nu}_\mathrm{e}$ candidates, as a function of the reactor power

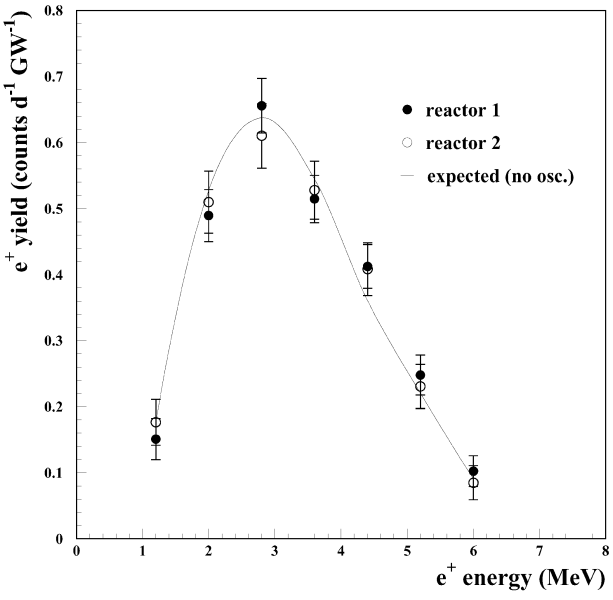

Fig. 50. Positron yields for the two reactors, as compared with expected yield for no oscillations

9.7 Neutrino yield for individual reactors

The same fitting procedure can be used to determine the contribution to the neutrino yield from each reactor and for each energy bin of the positron spectra. After splitting the signal term into separate yields and introducing a dependence on the positron energy, (43) can be rewritten as

$$\overline{N}_i(E_j) = (B(E_j) + W^*_{1i}(E_j)X_1(E_j) + W^*_{2i}(E_j)X_2(E_j))\Delta t_i \qquad (47)$$

The spectrum shape is expected to vary, due to fuel aging, throughout the reactor cycle. Burn-up correction factors η_{ki} then need to be calculated for each bin of the positron spectrum. The fitted yields, averaged over the three periods, are listed in Table 8 and plotted in Fig. 50 against the expected yield in absence of neutrino oscillations.

The yield parameters X_1, X_2 are slightly correlated, as shown in Table 8; this correlation (which does not exceed 20%) is always negative, since, at given candidate and background rates, an increase in reactor 1 yield corresponds to a decrease in reactor 2 yield (and *vice versa*). X_1 and X_2 are expected to be the same in the case of no-oscillation.

9.8 Neutrino yield versus fuel burn-up

As previously remarked, the contributions of the main fissile isotopes to the thermal power change in the course of an operating period; this should produce a corresponding decrease in the total neutrino counting rate as well as a

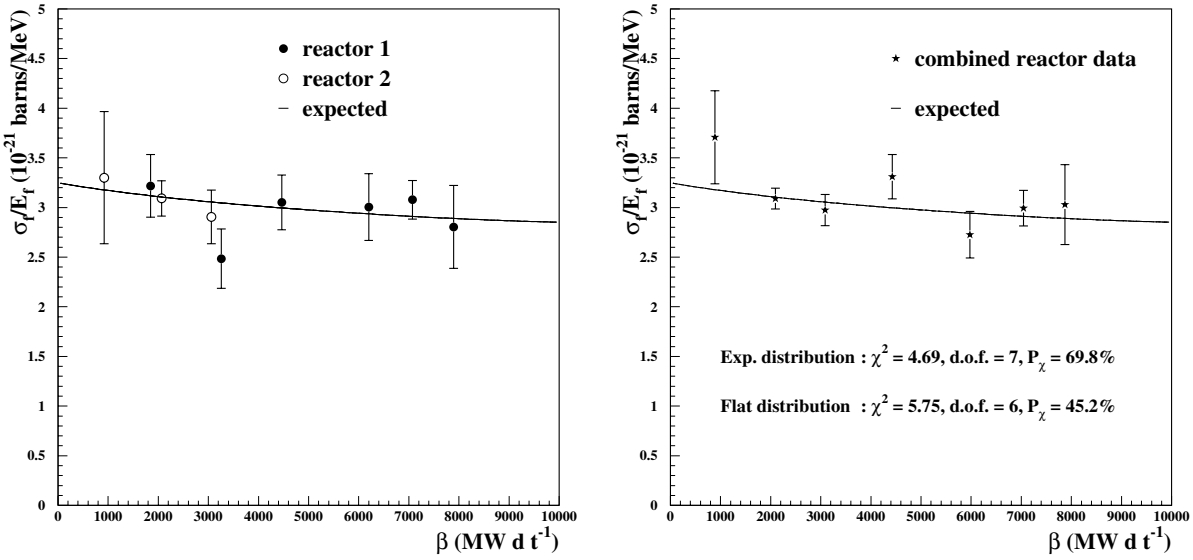

Fig. 51. Variation of the measured neutrino counting rate, as a function of the fuel burn-up for separate (*left*) and combined (*right*) reactor data and comparison with predictions. Error bars include only statistical uncertainties

Table 8. Experimental positron yields for both reactors (X_1 and X_2)and expected spectrum ($\tilde{X}$) for no oscillation. The errors (68% C.L.) and the covariance matrix off-diagonal elements are also listed

E_{e+} MeV	$X_1 \pm \sigma_1$	$X_2 \pm \sigma_2$ (counts $d^{-1}\,GW^{-1}$)	$\tilde{X}$	σ_{12}
1.2	0.151 ± 0.031	0.176 ± 0.035	0.172	$-2.2\ 10^{-4}$
2.0	0.490 ± 0.039	0.510 ± 0.047	0.532	$-1.5\ 10^{-4}$
2.8	0.656 ± 0.041	0.610 ± 0.049	0.632	$-3.5\ 10^{-4}$
3.6	0.515 ± 0.036	0.528 ± 0.044	0.530	$-3.3\ 10^{-4}$
4.4	0.412 ± 0.033	0.408 ± 0.040	0.379	$-2.0\ 10^{-4}$
5.2	0.248 ± 0.030	0.231 ± 0.034	0.208	$-0.7\ 10^{-4}$
6.0	0.102 ± 0.023	0.085 ± 0.026	0.101	$-1.3\ 10^{-4}$

modification in the spectral shape. The magnitude of this variation amounts to $\approx 10\%$ throughout the first cycle of the CHOOZ reactors, as we have already shown (see Sect. 2.6), which by far exceeds the statistical and systematic accuracy of the neutrino flux. We were then forced to follow the dynamics of the fuel burn-up and to apply daily corrections to the thermal power in order to restore the linearity with the positron yield (see (41),(42)).

We set out to establish whether the neutrino counting rate varies with the reactor burn-up according to predictions, with the purpose of improving the reliability and internal consistency of our results. The number N_ν of neutrino events, recorded in a time interval Δt, by a detector at a distance L from the core of a reactor working at a power W can be derived from (7); by inverting we find

$$\frac{\sigma_f}{E_f} = 4\pi \frac{L^2}{W \Delta t} \frac{N_\nu}{N_p \varepsilon} \tag{48}$$

σ_f and E_f being respectively the reaction cross section (10) and the average energy absorbed in the core in a single fission. The ratio σ_f/E_f, which contains the dependence on the fuel composition, can be evaluated for either reactor by considering the runs where reactors were alternatively *on*; runs are selected if the thermal energy is $\int W\,dt > 850\,GW\,d$ (which is the energy released in one day by a reactor at 20% of full power). The number of neutrino events is obtained by subtracting the number of background events (as determined in the previous Section) from the number of candidate events collected in a run. The resulting σ_f/E_f values are finally grouped in 1000 MW d burn-up intervals and plotted vs. reactor burn-up in Fig. 51(left).

A more significant test is performed by using combined reactor information. Each run is assigned an average burn-up defined as

$$\overline{\beta} \equiv \frac{\beta_1 W_1/L_1^2 + \beta_2 W_2/L_2^2}{W_1/L_1^2 + W_2/L_2^2}; \tag{49}$$

where β_1 and β_2 are the burn–up values for the two reactors.

Similarly, σ_f/E_f is obtained by

$$\frac{\sigma_f}{E_f} = 4\pi \left(\frac{L_1^2}{W_1 \Delta t} + \frac{L_2^2}{W_2 \Delta t} \right) \frac{N_\nu}{N_p \varepsilon} \tag{50}$$

The resulting values are plotted in Fig. 51(right) and compared with expectations; the compatibility is excellent, since $\chi^2 = 4.69$ with 7 d.o.f., corresponding to 69.8% χ^2-probability. The data compatibility with a flat distribution is also good ($\chi^2 = 5.75$ with 6 d.o.f., $P_{\chi^2} = 45.2\%$), but lower than in the previous comparison.

9.9 Neutrino direction

The use of reaction (2) to detect low energy antineutrinos in large volume scintillator detectors is an ideal tool for

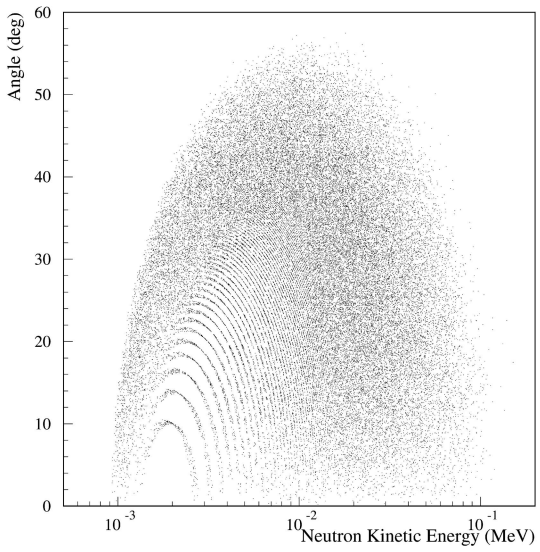

Fig. 52. Neutron emission angle (with respect to the incident $\overline{\nu}_e$ direction) vs. its kinetic energy; the discrete structure of lower-left part of the picture is an effect of the logarithmic scale for the abscissa combined with the $\overline{\nu}_e$ energy binning

measuring the antineutrino energy spectrum. Moreover, it provides a good determination of the antineutrino incoming direction [61,62]. This determination is based on the neutron boost in the forward direction, as a result of the kinematics of the reaction; the neutron then retains a memory of the source direction, which survives even after collisions with the protons in the moderating medium.

In CHOOZ we exploited this neutron recoil technique to locate the reactor direction [63], with the twofold objective of testing our event reconstruction method and tuning our Monte Carlo simulations of the slowing down and capture of neutrons in the scintillator. We then studied a possible extension of this technique to much larger scintillation detectors, such as Kamland, and their capabilities in locating astrophysical neutrino sources, such as Supernovæ. The neutron emission angle with respect to the incident neutrino direction is limited to values below $\sim 55°$; this results from Fig. 52, where the neutron angle θ_n is plotted vs. the neutron kinetic energy T_n (which extends up to $\sim 100\,\mathrm{keV}$). Moreover, the neutron moderation maintains some memory of the initial neutron direction [64]: in each elastic scattering the average cosine of the outgoing neutron is $\langle \cos\theta_n \rangle = 2/3A$, A being the mass number of the scattering nucleus. The direction is thus best preserved by collisions on protons, which is also the most effective target nucleus at energies below 1 MeV. The neutron mean free path rapidly reduces during moderation, since the scattering cross section rapidly increases at increasingly lower neutron energies; so the bulk of the neutron displacement is due to the first two or three collisions. The isotropic diffusion of thermalized neutrons does not affect the average neutron displacement along the neutrino direction.

The average neutron displacement in CHOOZ has been calculated to be 1.7 cm. Since the experimental position resolution is $\sigma_x \approx 19\,\mathrm{cm}$ for the neutron and the collected neutrino statistic is ≈ 2500, the precision of the method is $\approx 0.4\,\mathrm{cm}$; so neutron displacement can be observed at $\sim 4\sigma$ level. The average direction (in spherical coordinates) of the two reactors in the CHOOZ detector frame was measured by standard surveying techniques to be $\phi = (-50.3 \pm 0.5)°$ and $\theta = (91.5 \pm 0.5)°$.

Table 9. Measurement of neutrino direction: data and Monte Carlo. The angle δ is the $1\sigma-$uncertainty on $\overline{\nu}_e$ direction

	ϕ	θ	δ
Data	$-70°$	$103°$	$18°$
MC	$-56°$	$100°$	$19°$

The neutrino direction resulting from the data and the associated uncertainty, is presented in Table 9; the Monte Carlo predictions, for a sample with the same statistics, is also listed for comparison. The measured direction has a 16% probability of being compatible with the expected value, while the probability of a fluctuation of an isotropic distribution is negligible. The average neutron displacement was found to be $(1.9 \pm 0.4)\,\mathrm{cm}$, in agreement with what expected.

10 Neutrino oscillation tests

Three different approaches were adopted to analyse the results of the experiment. The first one ("analysis A" in what follows) uses the predicted positron spectrum in addition to the measured spectra for each reactor. This approach uses the absolute normalization and is therefore sensitive to the mixing angle even for large δm^2 values, where the oscillation structure could no longer be resolved in the energy spectrum and the oscillation limits exclusively depend on the uncertainty in the absolute normalization.

The second approach ("analysis B") uniquely relies on a comparison of measurements taken at different reactor core–detector distances. We are led to limits on the oscillation parameters which are practically independent of the uncertainties in the reactor antineutrino flux and spectrum; other major sources of systematic uncertainties, such as detection efficiencies and the reaction cross section, also cancel out. The result of this analysis can thus be regarded as free from all these systematic uncertainties.

The third approach ("analysis C") is somewhat intermediate between the first two analyses. It uses the shape of the predicted positron spectrum, while leaving the absolute normalization free. The only contribution to the systematic shape uncertainty comes from the precision of the neutrino spectrum extraction method [26].

10.1 Global test (Analysis A)

In a simple two-neutrino oscillation model, the expected positron yield for the k-th reactor and the j-th energy

spectrum bin, can be parametrized as follows:

$$\overline{X}(E_j, L_k, \theta, \delta m^2) = \tilde{X}(E_j)\overline{P}(E_j, L_k, \theta, \delta m^2), \quad (j = 1, \ldots, 7 \quad k = 1, 2) \quad (51)$$

where $\tilde{X}(E_j)$ is the distance-independent positron yield in the absence of neutrino oscillations defined in the previous section, L_k is the reactor-detector distance and the last factor represents the survival probability averaged over the energy bin and the finite detector and reactor core sizes. The procedure to compute such a probability at varying oscillation parameters is similar to the method used to calculate the burn-up corrections to the positron yields (see Sect. 9.6); the positron spectrum is obtained by (37) after adding the detector response function and the size function; the same procedure was applied to obtain the spectrum for no oscillations; the probability $\overline{P}(E_j, L_k, \theta, \delta m^2)$ results then from the ratio of the j-th bin contents of the two spectra.

In order to test the compatibility of a certain oscillation hypothesis $(\theta, \delta m^2)$ with the measurements, we built a χ^2 statistic containing the experimental yields for the 7 energy bins at the two positions L_k listed in Table 8. We grouped these values into a 14-element array X arranged as follows:

$$\mathbf{X} = (X_1(E_1), \ldots, X_1(E_7), X_2(E_1), \ldots, X_2(E_7)), \quad (52)$$

and similarly for the associated variances. These components are not independent, as already noted in Sect. 9.7. By combining the statistical variances with the systematic uncertainties related to the neutrino spectrum, the 14×14 covariance matrix can be written in a compact form as follows:

$$V_{ij} = \delta_{i,j}(\sigma_i^2 + \tilde{\sigma}_i^2) + (\delta_{i,j-7} + \delta_{i,j+7})\sigma_{12}^{(i)} \quad (i, j = 1, \ldots, 14), \quad (53)$$

where σ_i are the statistical errors associated with the yield array (52), $\tilde{\sigma}_i$ are the systematic uncertainties and $\sigma_{12}^{(i)}$ are the covariance of reactor 1 and 2 yield contributions to the i-th energy bin (see Table 8). These systematic errors, including the statistical error on the measured β-spectra measured at ILL [26] as well as the bin-to-bin systematic error inherent in the conversion procedure, range from 1.4% at 2 MeV (positron energy) to 7.3% at 6 MeV and are assumed to be uncorrelated[4].

We still have to take into account the systematic error related to the absolute normalization; combining all the contributions listed in Table 10, we obtain an overall normalization uncertainty of $\sigma_\alpha = 2.7\%$. We may define the following χ^2 function

[4] The extraction of the neutrino spectra from the β measurement at ILL should introduce a slight correlation of the bin-to-bin error systematic error. Nevertheless, the overall uncertainties on the positron yields are dominated by statistical errors, so that neglecting the off-diagonal systematic error matrix does not affect the oscillation test significantly. Also previous reactor experiments, even with much lower statistical errors, did not take this correlation into account

Table 10. Contributions to the overall systematic uncertainty on the absolute normalization factor

parameter	relative error (%)
reaction cross section	1.9%
number of protons	0.8%
detection efficiency	1.5%
reactor power	0.7%
energy released per fission	0.6%
combined	2.7%

$$\chi^2(\theta, \delta m^2, \alpha, g) = \sum_{i=1}^{14}\sum_{j=1}^{14}\Big(X_i - \alpha\overline{X}\big(gE_i, L_i, \theta, \delta m^2\big)\Big) \times V_{ij}^{-1}\Big(X_j - \alpha\overline{X}\big(gE_j, L_j, \theta, \delta m^2\big)\Big) + \left(\frac{\alpha - 1}{\sigma_\alpha}\right)^2 + \left(\frac{g - 1}{\sigma_g}\right)^2, \quad (54)$$

where α is the absolute normalization constant, g is the energy-scale calibration factor, $L_{i,j} = L_1$ for $i, j \leq 7$ and $L_{i,j} = L_2$ for $i, j > 7$. The uncertainty on g is $\sigma_g = 1.1\%$, resulting from the accuracy on the energy scale calibration (16 keV at the 2.11 MeV visible energy line associated with the n-capture on Hydrogen) and the 0.8% drift in the Gd-capture line, as measured throughout the acquisition period with high-energy spallation neutrons (see Fig. 38). The χ^2 in (54) thus contains 14 experimental errors with 2 additional parameters, yielding altogether 16 variances. The χ^2 value for a certain parameter set $(\theta, \delta m^2)$ is determined by minimizing (54) with respect to the gain factor g and to the normalization α; the minimization then leads to 12 degrees of freedom. The minimum value $\chi^2_{min} = 5.0$, corresponding to a χ^2 probability $P_\chi = 96\%$, is found for the parameters $\sin^2(2\theta) = 0.23$, $\delta m^2 = 8.1 \cdot 10^{-4}\,\mathrm{eV}^2$, $\alpha = 1.012$, $g = 1.006$; the resulting positron yields are shown by solid lines in Fig. 53 and superimposed on the data. Also the no-oscillation hypothesis, with $\chi^2(0, 0) = 5.5$, $\alpha = 1.008$ and $g = 1.011$, is found to perfectly fit with the data ($P_\chi = 93\%$).

To test a particular oscillation hypothesis $(\theta,\ \delta m^2)$ against the parameters of the best fit and to determine the 90% confidence belt, we adopted the Feldman & Cousins prescription [65]. The "ordering" principle is based on the logarithm of the ratio of the likelihood functions for the two cases:

$$\lambda(\theta, \delta m^2) = \chi^2(\theta, \delta m^2) - \chi^2_{min} \quad (55)$$

where the mimimum χ^2 value must be searched for within the physical domain $(0 < \sin^2(2\theta) < 1,\ \delta m^2 > 0)$. Smaller λ values imply better compatibility of the hypothesis with the data. The λ distribution for the given parameter set was evaluated by performing a Monte Carlo simulation of a large number (5000) of experimental positron spectra whose values are scattered around the predicted positron yields $\overline{X}(E_i, L_i, \theta, \delta m^2)$ with Gaussian-assumed variances σ_i and correlation coefficients given by (53). For each set we extracted the quantity $\lambda_c(\theta, \delta m^2)$ such that 90% of the

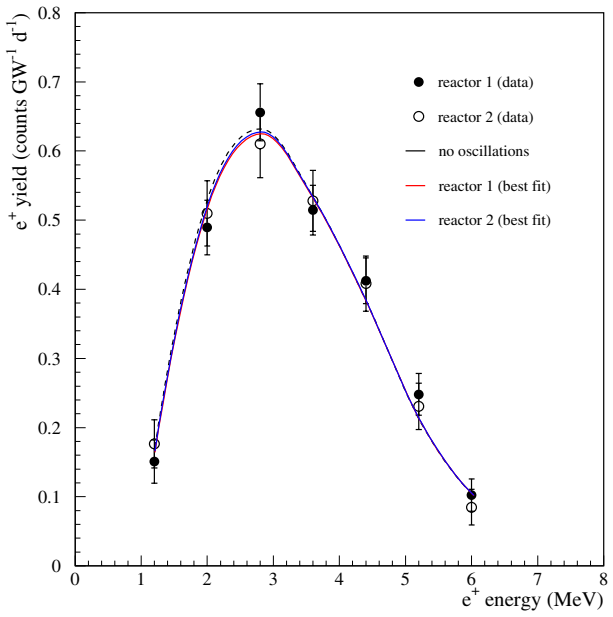

Fig. 53. Positron yields for reactor 1 and 2; the solid curves represent the predicted positron yields corresponding to the best-fit parameters, the dashed one to the predicted yield for the case of no oscillations

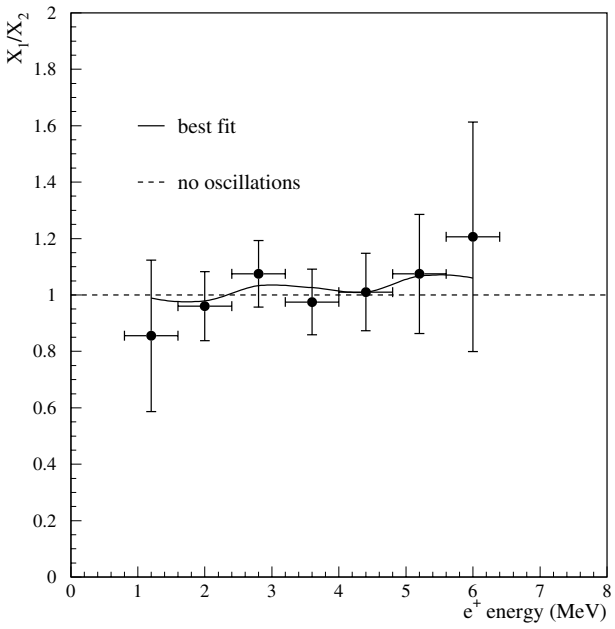

Fig. 54. Measured ratio of experimental positron yield, compared with the predicted ratio in the best oscillation hypothesis (solid line) and in the case of no oscillations (dashed line)

simulated experiments have $\lambda < \lambda_c$. The 90% confidence domain then includes all points in the $(\sin^2(2\theta), \delta m^2)$ plane such that

$$\lambda_{exp}(\theta, \delta m^2) < \lambda_c(\theta, \delta m^2), \tag{56}$$

where λ_{exp} is evaluated for the experimental data for each point in the physical domain.

The acceptance domain at the 90% C.L. (solid line) is shown in Fig. 55; all the parameters lying to the right of the curves are excluded by CHOOZ with the indicated confidence level, while the parameter regions on the left are still compatible with our data. The region allowed by Kamiokande for the $\nu_\mu \to \nu_e$ oscillations is also shown for comparison; this hypothesis, a possible explanation for the ν_μ deficit in the atmospheric neutrino flux, is excluded. The δm^2 limit at full mixing is $7 \cdot 10^{-4}\,\mathrm{eV}^2$; the limit for the mixing angle in the asymptotic range of large mass differences is $\sin^2(2\theta) = 0.10$.

10.2 Two-distance test (Analysis B)

The predicted ratio of the two–reactor positron yields equals the ratio of the corresponding survival probabilities. At full mixing ($\sin^2(2\theta) = 1$) and at low mass differences ($\delta m^2 \approx 10^{-3}\,\mathrm{eV}^2$), this ratio can be approximated by

$$\begin{aligned}\overline{R} &\approx \left[1 - \left(\frac{1.27\delta m^2 L_1}{E_\nu}\right)^2\right]\left[1 + \left(\frac{1.27\delta m^2 L_2}{E_\nu}\right)^2\right] \\ &\approx 1 - 2\left(\frac{1.27\delta m^2}{E_\nu}\right)^2 L\delta L,\end{aligned} \tag{57}$$

where L is the average reactor-detector distance and δL is the difference of the two distances. Therefore an experiment which measures this ratio with an uncertainty σ is sensitive to oscillations down to mass-difference values as low as

$$\delta m^2 \approx \frac{E_\nu}{1.27}\sqrt{\frac{k\sigma}{2L\delta L}}, \tag{58}$$

k being the number of standard deviations corresponding to the chosen confidence level. This value can be compared to the sensitivity limit δm_0^2 inherent in analysis A by noting that

$$\delta m^2 \approx \sqrt{\frac{L}{2\delta L}}\delta m_0^2 \approx 2\delta m_0^2 \approx 1.5 \cdot 10^{-3}\,\mathrm{eV}^2 \tag{59}$$

Although twice as large, this limit is lower than the lowest δm^2 value allowed by Kamiokande (see Fig. 55). The ratio $R(E_i) \equiv X_1(E_i)/X_2(E_i)$ of the measured positron yields must be compared with the expected values; since the expected yields are the same for both reactors in the case of no-oscillations, the expected ratio for the i-th energy bin reduces to the ratio of the average survival probability in that bin. We can then build the following χ^2 statistic:

$$\chi^2 = \sum_{i=1}^{7}\left(\frac{R(E_i) - \overline{R}(E_i, \theta, \delta m^2)}{\delta R(E_i)}\right)^2 \tag{60}$$

where $\delta R(E_i)$ is the statistical uncertainty on the measured ratio. The minimum χ^2 value ($\chi^2_{min} = 0.78$ over 5 d.o.f.) occurs at $\sin^2(2\theta) = 1$ and $\delta m^2 = 0.6\,\mathrm{eV}^2$; the compatibility of the no-oscillation hypothesis is still excellent (see Fig. 54), as $\chi^2(0,0) = 1.29$.

We adopted the same procedure described in the previous section to determine the confidence domain in the

$(\sin^2(2\theta), \delta m^2)$ plane and for each point in this plane we simulated the results of 5000 experiments. If the positron yields of both reactors are Gaussian distributed around the predicted values $\overline{X}_{1,2}$, and if $\overline{X}_2/\sigma_2$ is sufficiently large so that the X_2 generated have only positive values, then the variable

$$Z = \frac{\dfrac{\overline{X}_1}{\overline{X}_1} - \dfrac{\overline{X}_2}{\overline{X}_2}}{\sqrt{\dfrac{\sigma_1^2}{\overline{X}_1^2} + \dfrac{\sigma_2^2}{\overline{X}_2^2} - 2\dfrac{\sigma_{12}}{\overline{X}_1\overline{X}_2}}} = \frac{\overline{X}_1 - \overline{X}_2 R}{\sqrt{\sigma_1^2 + \sigma_2^2 R^2 - 2\sigma_{12} R}} \tag{61}$$

is normally distributed with zero mean and unit variance [56]. We could then use a normal random generator to extract Z and invert (61) to determine the ratio $R(E_i)$.

The exclusion plot obtained at 90% C.L. is also shown in Fig. 55. Although less powerful than the previous analysis, the region excluded by this oscillation test almost completely covers the one allowed by Kamiokande.

10.3 Shape test (Analysis C)

This test is similar to analysis A, the only difference being related to the hypothesis on the absolute normalization. In analysis A we fixed the integral counting rate to be distributed around the predicted value ($\alpha = 1$), with $\sigma_\alpha = 2.7\%$ systematic uncertainty; in the shape test, on the contrary, we gave up any constraint on the normalization parameter (which is equivalent to having $\sigma_\alpha = \infty$). The χ^2 statistic for this test is the same expression as (54) without the term depending on the normalization, so we can write

$$\begin{aligned}\chi^2(\theta, \delta m^2, \alpha, g) = &\sum_{i=1}^{14}\sum_{j=1}^{14}\Big(X_i - \alpha\overline{X}\big(gE_i, L_i, \theta, \delta m^2\big)\Big) \\ &\times V_{ij}^{-1}\Big(X_j - \alpha\overline{X}\big(gE_j, L_j, \theta, \delta m^2\big)\Big) \\ &+ \left(\frac{g-1}{\sigma_g}\right)^2,\end{aligned} \tag{62}$$

This χ^2 has a minimum value $\chi^2_{min} = 2.64$ (over 11 degrees of freedom) at $\sin^2(2\theta) = 0.23$, $\delta m^2 = 2.4 \cdot 10^{-2}\,\mathrm{eV}^2$ and $g = 1.008$; the null hypothesis gives instead $\chi^2(0,0) = 5.5$ with $g = 1.006$. The exclusion plot, obtained according to the Feldman–Cousins prescriptions, is shown in Fig. 55 and compared to the results of the other tests. As in the case of the two-distance test it is not sensitive to oscillations at large squared mass-difference values ($\delta m^2 \gtrsim 0.1\,\mathrm{eV}^2$), where the oscillation length

$$L_{osc}(\,\mathrm{m}) = \frac{2.48 E_\nu(\,\mathrm{MeV})}{\delta m^2(\,\mathrm{eV}^2)} \lesssim 100\,\mathrm{m} \tag{63}$$

becomes much lower than the average reactor–detector distance. The $\sin^2(2\theta)$ limit at the maximum oscillation probability is similar to that obtained with analysis A.

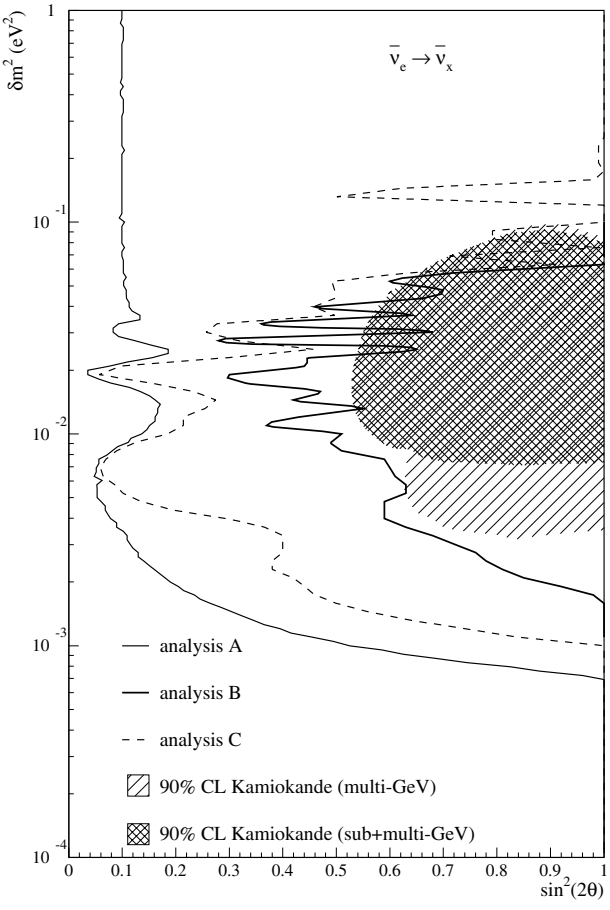

Fig. 55. Exclusion plot contours at 90% C.L. obtained by the three analyses presented. Analysis A uses both shape and normalization of the background-subtracted positron spectrum; analysis B uses the baseline difference between the two reactors; analysis C uses the spectrum shape. The Kamiokande $\nu_\mu \leftrightarrow \nu_e$ allowed region to atmospheric neutrino oscillations is also shown for comparison

10.4 Implications of the CHOOZ results

The importance of the CHOOZ results on neutrino oscillations has been pointed out by many authors [1,19,66–70]. In a three-flavour neutrino mixing frame, the see-saw mechanism indicates a mass hierarchy ($m_1 \ll m_2 \ll m_3$) from which

$$\delta m^2_{12} \ll \delta m^2_{23}. \tag{64}$$

The only available possibile explanation for solar and atmospheric neutrino anomalies through neutrino oscillations is that δm_{12} is relevant for the transitions of solar neutrinos and δm_{13} is the one probed by atmospheric and L-B accelerator neutrino experiments. By approximation (64) it is possible to show that the CP-violating phase in the 3×3 mixing matrix does not give rise to observable effects, and that the mixing angle θ_{12} (associated with the lower mass states) can be rotated away in the atmospheric neutrino analysis. Therefore, condition (64) implies that the transition probability in atmospheric and L-B experiments depends only on the largest mass squared difference

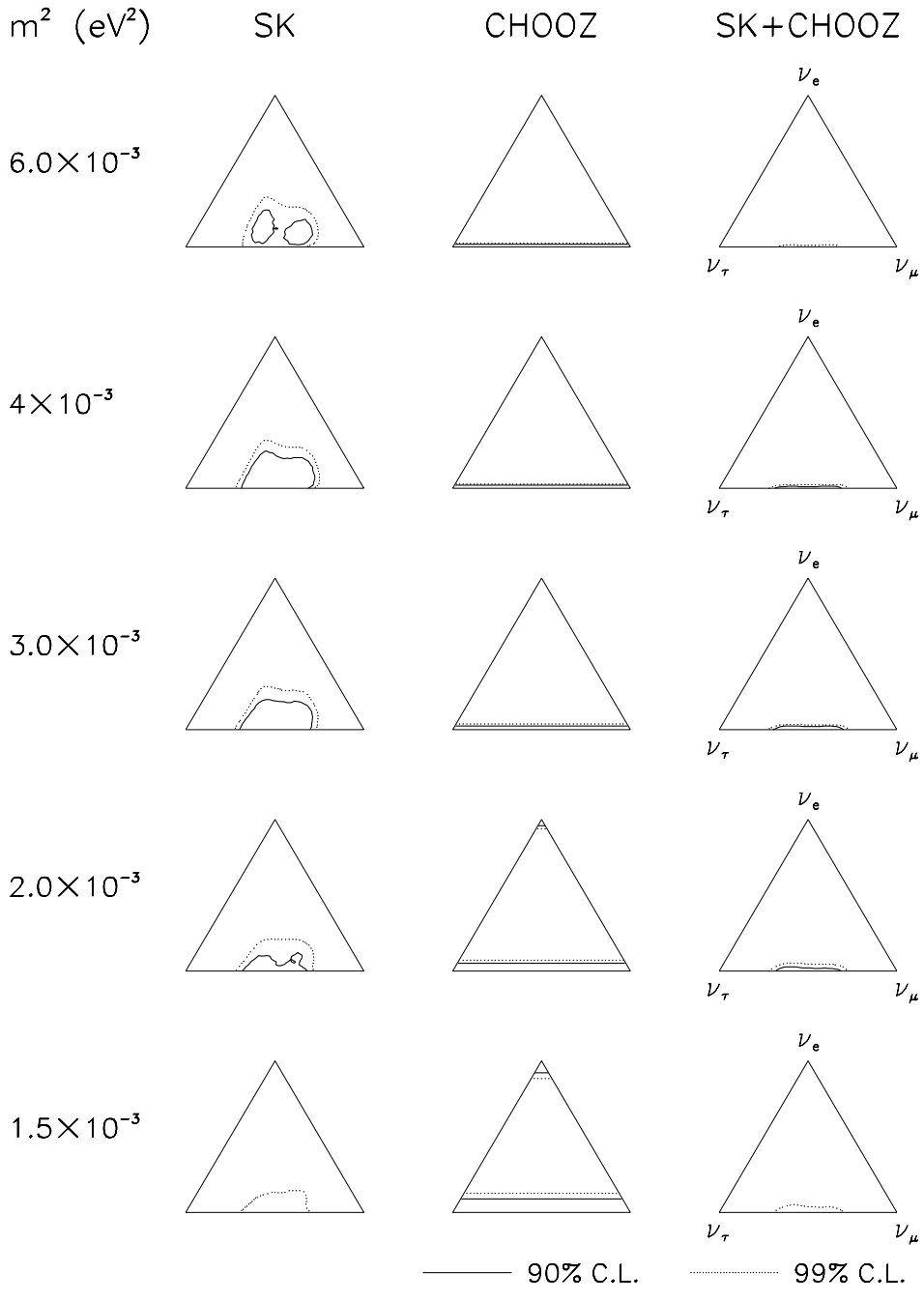

Fig. 56. Results of a three flavour mixing analysis of separate and combined Super-Kamiokande and CHOOZ data, for five representative values of $m^2 \equiv \delta m^2{}_{23}$. The analysis concerns the 79.5 kTy data sample for Super-Kamiokande and the first CHOOZ result [19]

δm^2_{23} and the elements $U_{\alpha 3}$ connecting flavour neutrinos with ν_3; it assumes then the simple form

$$P_{\nu_\alpha \to \nu_\beta} = \begin{cases} 1 - 4U^2_{\alpha 3}(1 - U^2_{\alpha 3}) \sin^2 \left(\dfrac{1.27 \delta m^2 (\mathrm{eV}^2) L(\mathrm{m})}{E(\mathrm{MeV})} \right) \\ \text{if } \alpha = \beta, \\ 4U^2_{\alpha 3} U^2_{\beta 3} \sin^2 \left(\dfrac{1.27 \delta m^2 (\mathrm{eV}^2) L(\mathrm{m})}{E(\mathrm{MeV})} \right) \\ \text{if } \alpha \neq \beta. \end{cases} \tag{65}$$

In particular, the survival probability reduces to the usual two-flavour formula (1) with $\sin^2 2\theta = 4U^2_{\alpha 3}(1 - U^2_{\alpha 3})$. Therefore, information on the parameter U_{e3} can be obtained from the CHOOZ exclusion plot. The upper limit for $\sin^2 2\theta$ implied by the exclusion plot in Fig. 55 is $\sin^2 2\theta \lesssim 0.1$ for $\delta m_{13} \gtrsim 2 \cdot 10^{-3}$; it follows that

$$U^2_{e3} < 0.03 \qquad or \qquad U^2_{e3} > 0.97 \tag{66}$$

Large values of values of U_{e3}, those allowed by the second inequality in (66), are excluded by the solar neutrino data [1]; the solar ν_e survival probability would be larger than 0.95, which is incompatible with the deficit observed in all solar neutrino experiments. The CHOOZ result then constrains the mixing of electron neutrinos with all other flavours, in the atmospheric and L-B range, to small values.

It has been remarked [19] that even the most recent Super-Kamiokande data alone do not completely exclude sizable ν_e mixing. This can be seen in Fig. 56, where the confidence regions for separate and combined Super–Kamiokande and CHOOZ data are shown for different values of $m^2 \equiv \delta m^2{}_{23}$ (the mass difference relevant for atmospheric neutrinos). Each set of mixing parameters (U_{e3}, $U_{\mu 3}, U_{\tau 3}$) is associated with a point embedded in a triangle graph (equilateral due to the unitarity condition), whose corners represent the flavour eigenstates; by convention ν_e is assigned the upper corner. The distance from the three sides are equal to U^2_{e3}, $U^2_{\mu 3}$, $U^2_{\tau 3}$; in a two-flavour scheme ($U_{\alpha 3} = 0$), the point is bound on the side connecting the two mixed flavour states (and the mean point of that side is associated with the maximum mixing hypothesis).

The CHOOZ result excludes large horizontal stripes in the triangle plot, according to (65); the stripe becomes increasingly narrower at lower $\delta m^2{}_{23}$ values, as a consequence of the reduced sensitivity to $\sin^2 2\theta$. The Super-Kamiokande allowed region lies on the triangle base and protrudes towards the centre, which implies a non-negligible $\nu_\mu \to \nu_e$ oscillation probablility. Yet in the combined analysis graph the allowed region is significantly flattened on the base, thus indicating a dominance of the $\nu_\mu \to \nu_\tau$ maximum mixing hypothesis.

The impact of CHOOZ in constraining the ν_e mixing is more evident in the bilogarthmic plot of Fig. 57 where the allowed regions (90 and 99% C.L.) in the m^2 ($\equiv \delta m^2{}_{23}$), $tan^2\phi$ ($\phi \equiv \theta_{13}$) parameter space are shown for the Super–Kamiokande data only (less restrictive limits) and for the combined Super–Kamiokande and CHOOZ data. The improvement obtained by using the CHOOZ data is of about one order of magnitude.

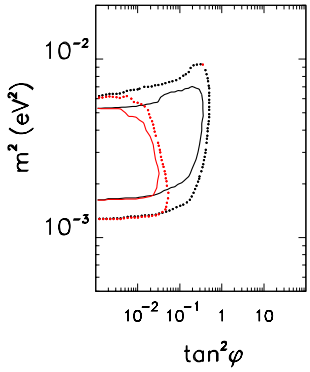

Fig. 57. 90% (*solid line*) and 99% C.L. (*dotted line*) limits in the m^2 ($\equiv \delta m^2{}_{23}$), $tan^2\phi$ ($\phi \equiv \theta_{13}$) parameter space obtained with the use of Super–Kamiokande alone (less restrictive limits) and CHOOZ +Super–Kamiokande [19]

11 A novel method for the derivation of confidence regions

The derivation of confidence regions for parameters, in neutrino oscillation experiments, has been the focus of attention and debate in recent years. There has been a general consensus in applying the Feldman and Cousins method (FC), which, apart from its intrinsic merit, allows a simpler comparison between experiments. Discussions about the statistical analysis are far from conclusive. We therefore tested an interesting new scheme which may represent a further step towards an objection-free procedure. It tends to produce confidence regions which are somewhat larger in size and, similarly, its application would more or less affect the results of all experiments. The new prescription [71] in confidence interval estimate is based on the concept of *strong Confidence Level* (*sCL*), to make an inference on neutrino oscillation parameters. This new method is purely frequentist, just like the FC "unified approach", yet it seems to be free from any pathologies inherent in every frequentist procedure proposed to date. Moreover, the definition of strong limits can be generalized in a natural way to include exact frequentist treatment of systematics [72]. Previous limits (Fig. 55) were computed by replacing the likelihood function with the one obtained by maximizing with respect to the systematic parameters ("profile" likelihood). This is an approximation [73] often used to overcome computational difficulties. It has been shown [72] that this approximation no longer holds in cases where the systematic error is of the same order of magnitude of the statistical one.

11.1 Application of the method

In this method we need to construct the probability density function (*pdf*) of our experiment in terms of the data (energy spectra) and the parameters (oscillation + normalization). For practical reasons, we decided to condense all the information (shape + normalization) contained in a spectrum $\boldsymbol{X}$ into the three parameters ($\hat{\sin^2(2\theta)}$, $\hat{\delta m^2}$), $\hat{\alpha}$) for which the likelihood is maximum; any parameter set uniquely identifies a particular energy spectrum. The set of maximum likelihood estimators (MLE) is our observable.

In order to obtain strong confidence limits, we computed the probability density function numerically. The domain of oscillation parameters ($0 < \sin^2(2\theta) < 1$, $10^{-4} < \delta m^2 < 1\,\mathrm{eV}^2$) was sampled by a 100× 100 grid (with a constant binning in $\log \delta m^2$); the range $0.95 < \alpha < 1.05$ was divided into 10 cells[5]. For each set of ($\sin^2(2\theta)$, δm^2, α) we generated $5 \cdot 10^4$ spectra scattered around $\alpha\overline{\boldsymbol{X}}(\sin^2(2\theta), \delta m^2)$ with uncertainties given by the covariance matrix. MLE for each experiment are searched for in the same space spanned by the parameters but with a coarser grid ($20 \times 20 \times 10$).

The results of our computation are shown in Fig. 58. The confidence bounds obtained are significantly higher than those obtained by the procedure explained in the previous section. In fact, oscillations $\overline{\nu}_e \to \overline{\nu}_x$ are excluded for $\delta m^2 \geq 8 \cdot 10^{-4}\,\mathrm{eV}^2$ at maximum mixing and

[5] We verified that values of α outside the considered range give no further contribution to the projection of the band on $(\sin^2(2\theta), \delta m^2)$-space

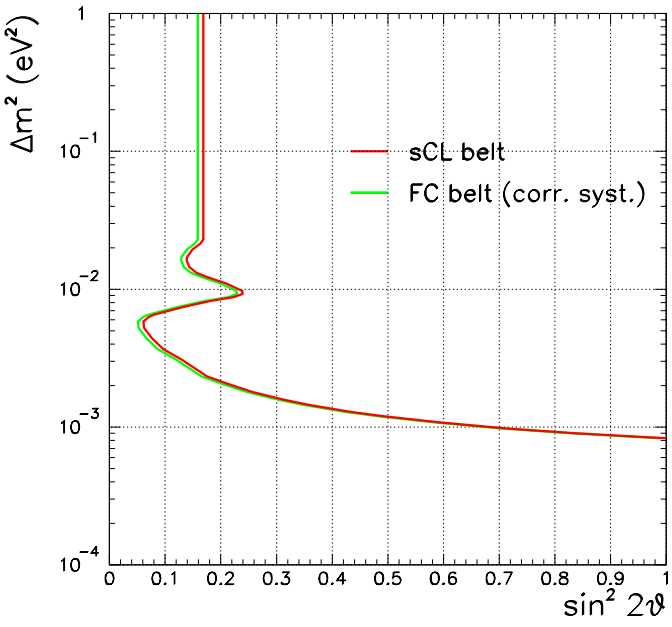

Fig. 58. Exclusion plot at 90% sCL for the oscillation parameters based on the differential energy spectrum; the FC contour, obtained with "correct systematics" treatment, is also shown

$\sin^2(2\theta) \geq 0.17$ at large δm^2 values. It should be noted that the limits quoted are only slightly looser than those obtained by using the FC prescription with the correct inclusion of systematics, as shown in Fig. 58.

12 Conclusions

The CHOOZ experiment stopped taking data in July 1998, about 5 years after the submission of the proposal for approval. With more than 1-year data taking, the statistical error (2.8%) on the neutrino flux matched the goal (3%) of the proposal. Accurate estimates of the detection efficiencies as well as precise measurements of the detector parameters also allowed us to keep the systematic uncertainty (2.7%) below expectations (3.2%).

We found (at 90% confidence level) no evidence for neutrino oscillations in the $\overline{\nu}_e$ disappearance mode, for the parameter region given by approximately $\delta m^2 > 7 \cdot 10^{-4}\,\mathrm{eV}^2$ for maximum mixing, and $\sin^2 2\theta = 0.10$ for large δm^2. Less sensitive results, based only on the comparison of the positron spectra from the two different-distance nuclear reactors (and therefore independent of the absolute normalization of the $\overline{\nu}_e$ flux, the number of protons and the detector efficiencies) were also presented.

Our result does not allow the atmospheric neutrino anomaly to be explained in terms of $\nu_\mu \to \nu_e$ oscillations, thus leaving, in a three-flavour mixing scheme, the $\nu_\mu \to \nu_\tau$ possibility.

Many cross-checks were performed on the data to test the internal consistence and improve the reliability of our results. As a by-product, we have shown that the use of reaction (2) allowed us to locate the $\overline{\nu}_e$ source within a cone of half-aperture $\simeq 18°$ at 68% confidence level.

Acknowledgements. Construction of the laboratory was funded by Électricité de France (E.D.F.). Other work was supported in part by IN2P3–CNRS (France), INFN (Italy), the United States Department of Energy, and by RFBR (Russia). We are very grateful to the Conseil Général des Ardennes for providing us with the facilities for the experiment. At various stages during the organization and management of the experiment, we were assisted by the efficient staff at SENA (Société Electronucléaire des Ardennes) and by the E.D.F. CHOOZ B nuclear plant. Special thanks to the technical staff of our laboratories for their excellent work in designing and building the detector. We would like to thank Prof. Erno Pretsch and his group at ETH Zurich, for some precise measurements of the target scintillator Hydrogen content.

References

1. S.M. Bilenky, C. Giunti, W. Grimus, Prog. Part. Nucl. Phys. **43**, 1 (1999)
2. B. Pontecorvo, Sov. Phys. JETP **6**, 429 (1958)
3. B. Pontecorvo, Sov. Phys. JETP **26**, 984 (1968)
4. Z. Maki, M. Nakagawa, S. Sakata, Prog. Theor. Phys. **28**, 870 (1962)
5. T.A. Kirsten, Rev. Mod. Phys. **71**, 1213 (1999)
6. S. Fukuda et al., Phys. Rev. Lett. **86**, 5651 (2001); ibidem **86**, 5656
7. Q.R. Ahmad et al., Phys. Rev. Lett. **87**, 071301 (2001)
8. Q.R. Ahmad et al., Phys. Rev. Lett. **89**, 011301 (2002)
9. Y. Fukuda et al., Phys. Lett. B **335**, 237 (1994)
10. K.S. Hirata et al., Phys. Lett. B **280**, 146 (1992)
11. Y. Fukuda et al., Phys. Rev. Lett. **81**, 1562 (1998)
12. Y. Fukuda et al., Phys. Rev. Lett. **82**, 2430 (1999)
13. S. Fukuda et al., Phys. Rev. Lett. **85**, 3999 (2000)
14. T. Kajita, Y. Totsuka, Rev. Mod. Phys. **73**, 85 (2001)
15. C. Bemporad, G. Gratta, P. Vogel, Rev. Mod. Phys. **74**, 297 (2002)
16. M. Apollonio et al., Phys. Lett. B **420**, 397 (1998)
17. M. Apollonio et al., Phys. Lett. B **466**, 415 (1999)
18. F. Boehm et al., Phys. Rev. D **64**, 112001 (2001)
19. G.L. Fogli, E. Lisi, A. Marrone, G. Scioscia, Phys. Rev. D **59**, 033001 (1999); G.L. Fogli, E. Lisi, A. Marrone, D. Montanino, A. Palazzo, preprint hep-ex/0105023, Contribution to 36th Rencontres de Moriond, 2001; G.L. Fogli, E. Lisi, A.Marrone, Phys. Rev. D **64**, 093005 (2001)
20. K. Schreckenbach, ILL technical report 84SC26T
21. Dossier de presse E.D.F., Mise en service de CHOOZ B1 (1996)
22. M.F. James, J. Nucl. Energy **23**, 517 (1969)
23. R.E. Carter et al., Phys. Rev. **113**, 280 (1959)
24. B.R. Davis et al., Phys. Rev. C **19**, 2259 (1979)
25. A.A. Borovoi et al., Sov. J. Nucl. Phys. **37**, 801 (1983)
26. F. von Feilitzsch et al., Phys. Lett. B **118**, 162 (1982)
27. K. Schreckenbach et al., Phys. Lett. B **160**, 325 (1985)
28. A.A. Hahn et al., Phys. Lett. B **218**, 365 (1989)
29. P. Vogel et al., Phys. Rev. C **24**, 1543 (1981)
30. G. Zacek et al., Phys. Rev. D **34**, 2621 (1986)
31. B. Achkar et al., Nucl. Phys. B **434**, 503 (1995)
32. B. Achkar et al., Phys. Lett. B **374**, 243 (1996)
33. H.V. Klapdor, J. Metzinger, Phys. Rev. Lett. **48**, 127 (1982)
34. O. Tengblad et al., Nucl. Phys. A **503**, 136 (1989)

35. A.A. Kuvshinnikov et al., Sov. J. Nucl. Phys. **52**, 300 (1990)
36. Y. Declais et al., Phys. Lett. B **338**, 383 (1994)
37. V.I. Kopeikin et al., Kurchatov Internal Report IAE-6026/2 (1997)
38. D.H. Wilkinson, Nucl. Phys. A **377**, 474 (1982)
39. Particle Data Group, Europ. Phys. J. C **15**, 692 (2000)
40. P. Vogel, Phys. Rev. D **29**, 1918 (1984)
41. S.A. Fayans, Sov. J. Nucl. Phys. **42**, 540 (1985)
42. Y. Declais, E. Duverney, A. Oriboni, CHOOZ Design Technical Report (1995)
43. P. Guillouet, LPC internal report 94-19
44. Laboratory of Organic Chemistry, ETH Zürich (kindness of prof. A. Pretsch)
45. Service central d' analyse, laboratoire du CNRS, Vernaison (France)
46. The Thorn EMI Inc. photomultipliers and accessories catalogue
47. A. Baldini et al., Nucl. Instr. Meth. A **372**, 207 (1996)
48. GEANT Reference Manual vers. 3.21 (1993)
49. R. Liu, MACRO internal memo 11/93 (1993)
50. H. de Kerret, B. Lefièvre, LPC internal report 88-01
51. S.F. Mughabghab, Neutron cross sections, ed. Academic Press
52. L.V. Groshev et al., Nucl. Data Table A **5**, 1 (1968)
53. R.R. Spencer, R. Gwin, R. Ingle, Nucl. Sci. and Eng. **80**, 603 (1982)
54. A. Baldini et al., Nucl. Instr. Meth. A **305**, 475 (1991)
55. A. Baldini et al., Nucl. Instr. Meth. A **389**, 141 (1997)
56. W.T. Eadie et al., Statistical methods of experimental physics, North-Holland, Amsterdam (1971)
57. S. Baker, R. Cousins, Nucl. Instr. Meth. **221**, 437 (1984)
58. F. James, MINUIT Reference Manual, vers. 94.1 (1994)
59. The CHOOZ experiment proposal (1993), available at the WWW site http://duphy4.physics.drexel.edu/chooz_pub/
60. E.D. Earle, P.Y. Wong, internal report AECL 9393/SNO-87-1 (addendum) (1987)
61. C. Bemporad, Proceedings of the 3rd International Workshop on Neutrino Telescopes, Venice (1991)
62. P. Vogel, J.F. Beacom, Phys. Rev. D **60**) (1999), 053003
63. M. Apollonio et al., Phys. Rev. D **61**, 012001 (1999)
64. E. Amaldi, The production and slowing down of neutrons, S. Flügge, Encyclopedia of Physics (Springer–Verlag ed.), vol. **38.2** (1959)
65. G.J. Feldman, R.D. Cousins, Phys. Rev. D **57**, 3873 (1998)
66. P.F. Harrison, D.H. Perkins, W.G. Scott, Phys. Lett. B **349**, 357 (1995)
67. R. Barbieri et al., JHEP **9812**, 017 (1998)
68. M.C. Gonzalez-Garcia, M. Maltoni, C. Pena-Garay, J.W.F. Valle, Phys. Rev. D **63**, 033005 (2001)
69. S.M. Bilenky, D. Nicolò, S.T. Petcov, Phys. Lett. B **538**, 77 (2002)
70. P.I. Krastev, A.Yu. Smirnov, Phys. Rev. D **65**, 073022 (2002)
71. G. Punzi, Stronger classical confidence limit, Contribution to the "Workshop on Confidence Limits", CERN Yellow Report 2000-005 (2000); G. Punzi, A stronger classical definition of confidence limit, INFN Pisa preprint INFN PI/AE 99/08 (also available on the INFN Pisa web site http://www.pi.infn.it/library/preprints)
72. D. Nicolò, G. Signorelli, Proceedings of the Conference on "Advanced Statistical Techniques in Particle Physics", Durham, 18-22 March 2002 (presented by G. Signorelli), available at http://www.ippp.dur.ac.uk/statistics/papers
73. A. Stuart, J.K. Ord, Kendall's Advanced Theory of Statistics, Vol. 2, 5th ed. (Oxford University Press, New York, 1991)